Multiscale Investigation of the Nonlinear Rheology of Wormlike Micelles

by

Abdulrazaq Abiodun Adams

A dissertation submitted in partial fulfillment
of the requirements for the degree of
Doctor of Philosophy
(Chemical Engineering)
in The University of Michigan
2018

Doctoral Committee:

Professor Ronald G. Larson, Co-Chair
Professor Michael J. Solomon, Co-Chair
Professor Sharon C. Glotzer
Professor Alan S. Wineman

Abdulrazaq A. Adams

adamsaa@umich.edu

ORCID iD: 0000-0003-0527-9939

To my parents, siblings, Nike and Rahma

ACKNOWLEDGEMENTS

My gratitude is to Allah for His mercy, guidance and protection.

I would like to especially appreciate my parents for their love, and sacrifice. I thank them for all their efforts towards making me who I am today. I am forever indebted to you. I thank my siblings for their support, care and love. To my lovely wife, thank you for your love, support and patience throughout the course of this program. I am grateful. And to my sweet daughter, I love you!

To my advisors, Professors Larson and Solomon, I have been very fortunate to learn from you. I am very grateful for the opportunity. I thank you immensely for your help and care. I've had a lot to learn from watching you and being mentored by you. You made me a better person. Thank you. I also appreciate your support. Thank you for offering me financial aid when things got tough. I am very grateful.

I would also like to thank my dissertation committee, Professors Glotzer and Wineman. I appreciate your comments and feedback throughout the course of this dissertation. Thank you.

I would also like to thank current and past members of the Larson and Solomon groups. It was fun meeting you all and interacting with you. I particularly would like to acknowledge Weizhong Zou, Priyanka Desai, and Youngri Kim for several insightful conversations . I learnt a lot from you. I thank you for teaching me on skills that I would go on to use in the course of my dissertation. And Weizhong thanks for your patience and clarity in answering my numerous questions. I also appreciate Xiaolin Xia for working with me tirelessly on the strain hardening project. I would also like

to thank Indranil Saha and Soroush Moghadam for sharing some of their codes with me.

I would like to thank the administrative staff at Chemical Engineering Department especially Susan Hamlin for being very helpful and welcoming. Ms Hamlin was my first point-of-contact in Michigan and she has been great all the way. I appreciate your And since then she has been very helpful. Thank you very much.

My appreciation goes to Bode Fujah, Amr Ibrahim, Mohammed Alzuabi for their friendship . I enjoyed every bit of your companionship. I also benefited from intellectual discussions. I would like to thank Amr for getting me up to speed with Matlab, it proved useful to me throughout this dissertation. And to Khalid Ahmed for introducing me to a lot of useful computational tools and other useful resources. Lest I forget, thanks Ahmad Jiman for your hospitality and friendship.

I would like to express my gratitude to the Good People of Nigeria and the Federal Government of Nigeria for funding my doctoral studies at The Univeristy of Michigan through the Presidential Special Scholarship for Innovation and Development (PRESSID) program. I would also like to thank The University of Michigan for funding me during the course of my studies. I acknowledge the support of the National Science Foundation (NSF) and Procter & Gamble. I thank Rackham Graduate School for sponsoring my trips to several conferences during the course of my studies.

I like to thank Will Hartt, Mike Weaver and Lori Bacca of P&G. Special thanks to Lori for making us some anionic surfactant samples. Many thanks to the members of Ann Arbor Muslim community and the friendly people of Michigan.

And to you, the reader, I hope you benefit from this work. Thank you.

TABLE OF CONTENTS

LIST OF FIGURES

Figure

LIST OF APPENDICES

Appendix

LIST OF ABBREVIATIONS

BD Brownian dynamics

CCR Convective constraint release

CTAB Cetyl trimethyl ammonium bromide

CTApTS Cetyltrimethylammonium p-toluene sulfonate

cmc critical micelle concentration

cwmc critical wormlike micelle concentration

CPyCl Cetyl pyridinium chloride

KBr Potassium bromide

NaCl Sodium chloride

NapTS Sodium p-toluene sulfonate

NaSal Sodium salicylate

Rheo-SALS Rheometry on Small Angle Light Scattering

Rheo-SANS Rheometry on Small Angle Neutron Scattering

Rolie-Poly Rouse Linear Entangled Polymers

SHNC Sodium 3-hydroxy-2-naphthoate

SLE1S Sodium lauryl ether (1) sulfate

SLE3S Sodium lauryl ether (3) sulfate

SLS Sodium lauryl sulfate

VCM Vasquez-Cook-McKinley

WLM Wormlike micelle

ABSTRACT

Wormlike micelles (WLMs) are formed by reversible self-assembly of amphiphilic (e.g. surfactant) molecules usually with the aid of salt which acts to screen the electrostatic repulsion between the micelles to achieve giant structures. Their unique dynamics such as reversible scission give them interesting rheological properties which are sought in several industrial applications. It is therefore imperative to understand and predict these phenomena in WLMs using constitutive equations that incorporate reversible scission into the deformation dynamics of WLMs.

We compare the predictions of the Vasquez-Cook-McKinley (VCM) (2007) model which treats WLMs as Hookean dumbbells that break at half-length to form two shorter dumbbells, to an analogous Brownian dynamics (BD) simulation of the same physical model. We find a discrepancy between their predictions and trace it to the absence in the VCM model of the internal position of the nascent breakage point in the long micelle, which is needed to satisfy microscopic reversibility of breakage and fusion. We correct this deficiency in the VCM model by extending an ensemble-averaged bead-spring phase space model of Wiest et al. (1989) to include reversible scission of two-spring chains. The revision tracks the conformations of the two halves of the long micelle and transmits this information to the short micelles upon breakage and thereby recovers complete agreement with the BD results.

We extend the reversible scission kinetics to the slip-link tube model of Likhtman (2005) originally formulated for single polymer chains with entanglements. This facilitates the simulation of entangled WLMs and enables us to study the effects of entanglements on WLM rheology. We observe increased stresses for start-up shear flows

in the entangled WLMs when breakage time was equal to reptation time. We propose that reversible scission acts as a means of constraint release which re-orientates chain segments in the velocity gradient direction and prevent retraction in the tube thereby causing increased stress. However, stress overshoot caused by the relaxation of the peak stress to a lower steady stress was observed in the fast-breaking regime. This suggests that reversible scission functions as both stress relaxation and constraint release mechanisms.

We then investigate strain hardening, a nonlinear rheological property. We explore different kinds of WLMs for strain hardening and systematically study their strain hardening dependence on salt concentration and temperature. By measuring stress relaxation following a step strain, we observe that strain hardening is prevalent over a temperature range of 15 - 25 C for a solution of cetyl trimethyl ammonium bromide (CTAB) with the added hydrotrope, sodium salicylate at hydrotrope-to-surfactant concentration ratios between 0.5 - 3.0. The extent of strain hardening upon nonlinear step-strain deformation varies non-monotonically as a function of salt-to-surfactant ratio for different temperatures. A transition from strain hardening to softening or linear response is observed at strains that are dependent on temperature and concentration. Strain hardening was also observed in solutions of CTAB and hydrotrope, sodium 3-hydroxy-2-naphthoate. However, solutions of anionic sodium lauryl sulfate surfactants without hydrotrope but simple salt, sodium chloride strain softened, indicating that the hydrotrope is crucial to obtaining strain hardening in step strains. The results indicate a stress relaxation mechanism that is more complex than that of simple disentanglement and reversible scission, possibly involving strain-induced associations between micelles facilitated by hydrotropes that may act as physical crosslinkers.

CHAPTER I

Introduction

1.1 Background

Wormlike micelles (WLMs) are a class of complex fluids that have generated significant scientific interest in recent decades and have been used in various industrial applications. Unlike ordinary polymers, wormlike micelles have a dynamic structure that forms a viscoelastic network from the reversible self-assembly of constituent molecules without the need of chemical cross-linking. The wormlike micelle structure can be influenced by the local fluid environment thereby making their structure and hence, rheology tunable to desired applications [1]. For instance, some wormlike micelle fluids exhibit changes in their microstructure and rheology with salinity, light, heat, pH, electricity among other stimuli [2]. The tunability of the rheology of wormlike micelles and the reversibility of their structure have made them attractive and suitable for many applications.

Wormlike micelles (WLMs) have been employed in drilling and pumping operations because of their ability to regain viscosity after exposure to high shear-rates. Thus, they can be re-used several times unlike polymer-based fluids that reduce in performance once their irreversible cross-links are broken. WLMs are better drag reducers than polymers in heat-exchangers and pipe flows because of the aforementioned reason coupled to their shear- and thermo- thickening properties [2, 3, 4]. In

biomedical applications, WLMs have been used for encapsulation and targeted release of drugs to pathological sites due to their responsiveness to stimuli such as pH, temperature, and redox potential [2]; and also their biodegradability, surface tension reduction and solubility [5]. In the cosmetic industry, they are used as major constituents of shampoos for their detergency, viscosity and foaming ability [4]. They are also used in many consumer products like coatings, lubricants, adhesives, and thin films. In electronic industry, they are used in making masks and photoresists and serve as tools for extreme high-resolution lithography [4, p. 176] in the production of integrated circuits.

Although, WLMs have been used in many industrial products and processes, industrialists still face many challenges in using them in some applications because some micellar properties could be disadvantageous to production process and even products themselves. For instance, strain hardening WLM fluids tend to clog filling nozzles over time. They resist flow and increase their stiffness when moderate force is applied to clear the clog. The clogging of lines can lead to downtime in production thus resulting in financial losses [6]. Knowledge of the nonlinear rheological behavior of WLMs is also needed to overcome the challenge of excessive thinning in enhanced oil recovery. The entangled WLMs are disintegrated into spherical micelles as they pass through the pore throat of the oil reservoir. The spherical micelles may not reform into entangled wormlike micelles by the time they pass through the next layer of pores, thereby causing reduced recovery [2]. Hence, it is essential to understand the the microstructural changes that cause these rheological properties in wormlike micelles.

Detailed understanding of the rheology of WLMs could be used to better design products by fine-tuning their rheology to suit the desired applications. This knowledge would ultimately lead to higher quality products and reduced costs of production. It is therefore of economic necessity to understand the relationship between the mi-

crostructure and rheology and be able to predict the stress response of micelles to deformation and flow for their intended applications. For this, constitutive equations are formulated from well-founded theories. However, many of the existing theories and constitutive equations have been developed for polymers and do not include the unique reversibility of structure and rheology observed in wormlike micelles. There is therefore the need to formulate models that include reversibility of structure to allow for accurate prediction of wormlike micelle dynamics.

1.2 Micelles

1.2.1 Molecular Structure and Formation

Micelles are molecular aggregates formed by the reversible assembly of amphiphilic molecules in solution [7]. Amphiphilic molecules (or amphiphiles) typically have a hydrophilic (water-loving) head and a hydrophobic (water-hating) tail [7, 4]. Amphiphiles could be surfactants, block co-polymers, colloids or polyelectrolytes and serve as building blocks for their aggregation into macromolecular structures. The amphiphilic molecules assemble to form micelles at concentrations slightly above the critical micelle concentration (cmc). The structure of the micelles formed depend on the packing parameter of the amphiphilic molecules which is defined as $p = v/al$, where v is volume of the hydrophobic tail with length, l and a is the area occupied by the hydrophilic head-group at the micelle surface. Figure 1.1 shows the expected micelle aggregate structure by packing parameter. When $p < 1/3$, the amphiphiles assemble into spherical aggregates and when $1/3 < p < 1/2$, they form wormlike structures. They assembly into vesicles between 1/2 and 1 and bilayers at about 1.

The structure of the aggregates also depend upon factors such as surfactant concentration, ionic strength, type of solvent, temperature and presence of counterion and/or co-surfactant [9, 10, 11, 12]. The assumed configuration is maintained by

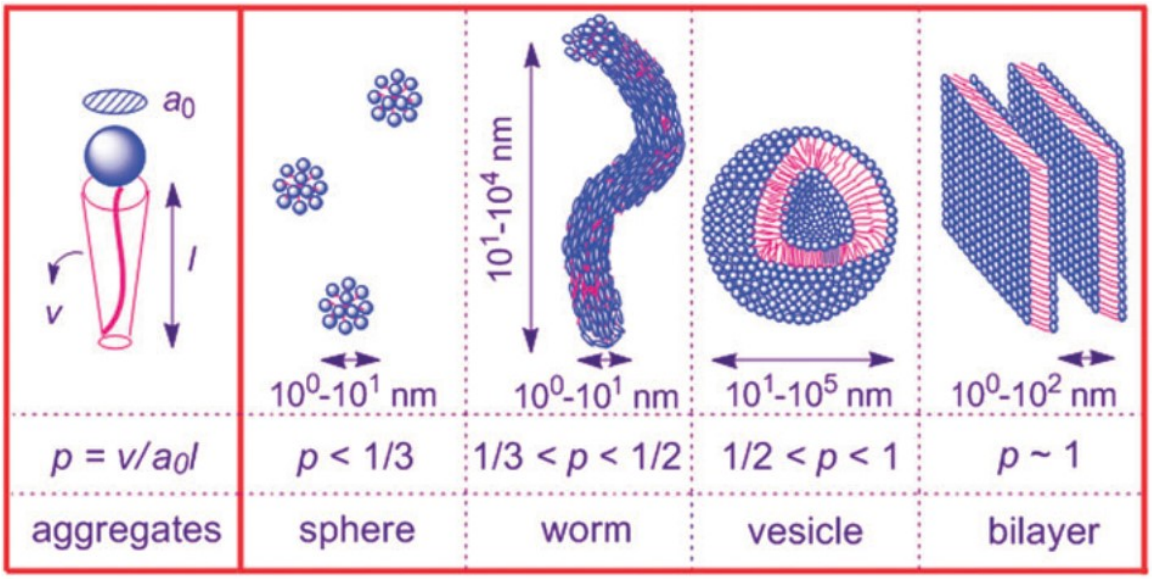

Figure 1.1: Amphiphilic molecules aggregate into different micelle structures based on their packing parameter. Reproduced ("Adapted" or "in part") from [8] with permission of The Royal Society of Chemistry.

competing forces: attractive van der Waals interactions between the hydrophobic tails that are opposed by hydrocarbon-water interfacial force, and the repulsion between the hydrophilic head groups [13]. Spherical aggregates are favored because it leaves the hydrophilic head of the micelle exposed to the water while it shields the hydrophobic tails from the water at the center of the micelle. An increase in surfactant concentration beyond a second cmc (also referred to as the critical wormlike micelle concentration (cwmc) [14]) can lead to a one-dimensional uniaxial growth of the micelles. This growth causes a sphere-to-worm/rodlike transition [15] leading to the formation of cylindrical geometries known as rods [11] with semi-spherical end caps [16]. The co-existence of spherical and wormlike micelles have been observed directly by cryogenic transmission electron microscopy (cryo-TEM) [15, 17, 18, 12] and indirectly by fluorescence [19]. The rods elongate as aggregation progresses and become flexible on a length-scale of the order of the persistent length [10] and are referred to as threadlike or wormlike micelles. The persistent length is the characteristic length for which there is no tangential correlation in the direction along the

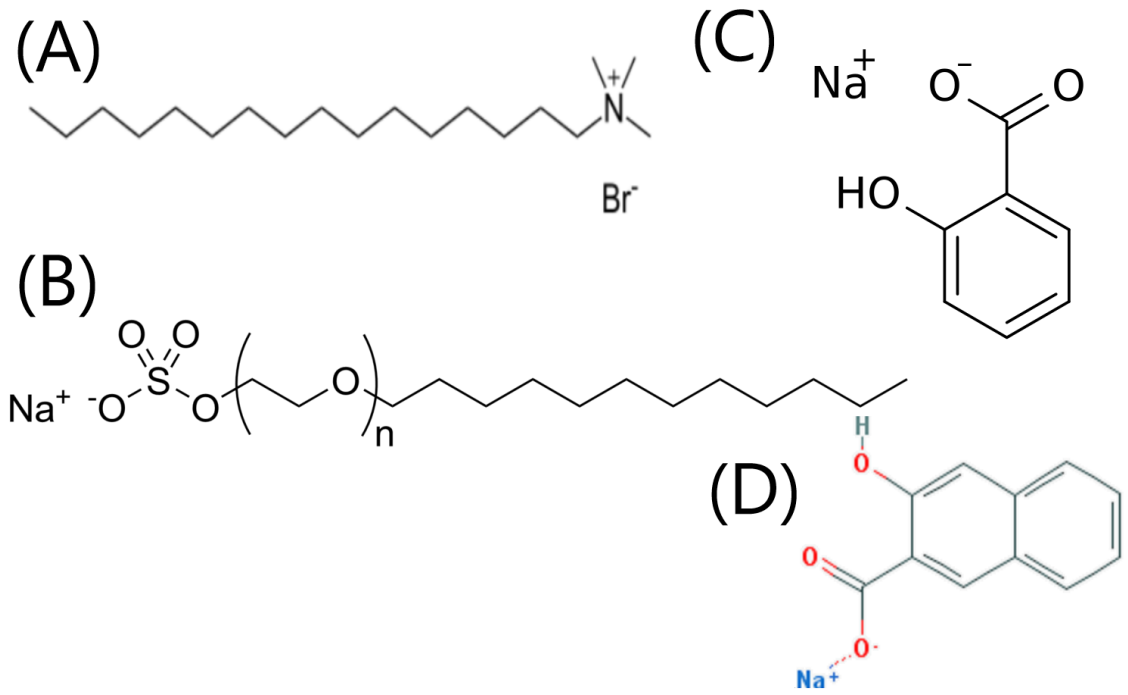

Figure 1.2: Chemical structures of common surfactants and salts used in making wormlike micelles. Cationic cetyl trimethyl ammonium bromide (CTAB) and anionic sodium lauryl sulfate (SLS) surfactants are depicted in (A) and (B) respectively. (C) and (D) represents the chemical structures of hydrotropic salts, sodium salicylate (NaSal) and sodium 3-hydroxy-2-naphthoate (SHNC) respectively.

contour of the micelle. Typically, micelle sizes are described in units of their Kuhn segments; the kuhn length, denoted by b_K, is a statistical length that equals double the persistent length [20].

Cetyl trimethyl ammonium bromide (CTAB)/NaSal and cetyl pyridinium chloride (CPyCl)/NaSal solutions are examples of surfactant-based micelle systems that have been studied extensively in the literature [13]. The structures of common wormlike micelle constituents are shown in Fig. 1.2. Certain salts, known as hydrotropes, are mostly aromatic salts that have the extraordinary ability of dissolving hydrophobic moieties and penetrating the micelle head group. In the formation of cationic CTAB-NaSal wormlike micelles, salicylate ions (Sal^-) from the hydrotropic salt, sodium salicylate (NaSal) have been reported to intercalate with cetyl trimethyl ammonium (CTA^+) head-groups [21, 10, 22] by binding to them at the hydrophobic-hydrophilic

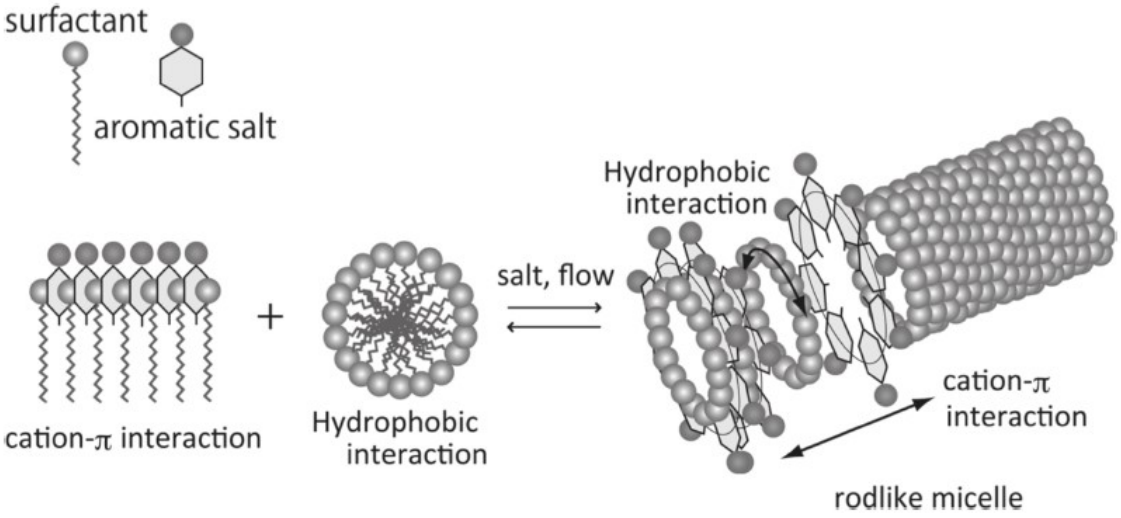

Figure 1.3: Cation-π and hydrophobic interaction in surfactant wormlike micelles that contain hydrotropes. Reprinted (adapted) with permission from [23]. Copyright (2011) American Chemical Society.

interface. They occupy the region between the outer head group and hydrophobic tails. The binding to the micelle head group is possible because of their size and the cation-π interaction, portrayed in Fig. 1.3, between the phenyl ring(s) of the hydrotrope and the cations of the surfactant head group [23]. The salicylate ions are relatively larger moieties compared to halide ions. They therefore act as a co-surfactant [9] in promoting aggregation. The presence of hydrotropes cause an electrostatic screening of the oppositely charged surfactant headgroups. This screening significantly reduces the repulsion in the head groups thereby facilitating further aggregation. The hydrophobic interaction produces the curvature while the cation-π interaction allows the micelles to stack longitudinally in one direction to form wormlike micelles even at relatively low surfactant concentrations. Sodium salicylate (NaSal) also bind strongly with CPyCl and is reported [21] to form long wormlike micelles at the *cmc* without intermediary spherical micelles formed in the process.

Anionic surfactants have also formed long threadlike micelles with bivalent and trivalent counterions [9] and cationic hydrotropes [24]. WLMs have been reported to be formed with anionic surfactants like sodium hexadecyl sulfate using quaternary am-

monium salts such as n-pentyl-N,N-diethyl-N-methylammonium bromide (C_5Et_2MeNBr) and alkyl toluidine halides such as N,N-dimethyl-N-ethyl-p-toluidine bromide ($Me_2EttolBr$) and p-toluidine hydrochloride [22, 24] via hydrophobic and anion-π interactions. Mixed surfactant systems in which one acts as a co-surfactant have also led to the formation of wormlike micelles [9]. For example, we study the nonlinear rheological behavior of sodium lauryl ether (3) sulfate (SLE3S)/sodium lauryl sulfate (SLS)/sodium chloride (NaCl) mixed-anionic surfactant wormlike micelle in Chapter IV. A number of possibilities exist with forming hybrid wormlike micelles by combining polymers and surfactants [25], proteins [2], polyelectrolytes [25, 26] and colloids. These hybrid combinations and variations are used to achieve different functionalities for the wormlike micelles.

1.2.2 Equilibrium Reaction Kinetics

As mentioned in Section 1.2.1, micelles form by assembling to form aggregates. The initial aggregates are bound together by hydrophobic interactions. They aggregate further by cation-π electrostatic interactions when hydrotropes are present. In addition, less common CH-π and π-π interactions also contribute to the assembly. The CH-π interactions occur between the C-H groups along the surfactant tails and phenyl rings while the π-π interactions occur between the phenyl rings themselves. However, these interactions are through Coloumbic and van der Waals forces which are weak compared to the covalent bonds found in polymeric assemblies. The cation-π binding strength is a factor of the nature of the cation, π system, geometry of interaction and solvation [27, 28, 29]. In solution, the strength of the cation-π bond is reduced with increasing polarity of the solvent [27]. Cation-π interaction contribute binding energies of the order of 0.844 kT per phenyl ring in aqueous media [28]. Therefore, these non-covalent bonds are easily perturbed by Brownian motion and thermal fluctuations. This perturbation causes the interacting species to dif-

fuse far beyond the van der Waals contact distance thereby leading to disaggregation and break-down of assembled structures. The continuous interplay between aggregation by non-covalent interactions and Brownian perturbation leads to the reversible scission of the wormlike micelle structure in equilibrium.

Reversible scission is a stress relaxation mechanism for the wormlike micelles. The breaking of long micelles into smaller pieces allow for quicker relaxation of the shorter micelles by chain stretch relaxation and reptation. Reptation is the curvilinear diffusion of the micelles in what appears to be in a snake-like motion to free itself of the constrictions imposed by surrounding micelles [30, 11]. Bond- and end- interchange are reaction mechanisms similar to reversible scission. Fig. 1.4 depicts the reaction mechanisms in equilibrium. During reversible scission, the wormlike micelles are assumed to break and fuse end-to-end along the longitudinal axis causing them to shorten and lengthen respectively. End interchange occurs when a micelle collides into another and breaks off with a part of it, thus getting new ones in the process. On the other hand, bond interchange occurs when two micelles cross each other to form an intermediary four-fold junction before dissociating into two micelles, each with a new set of links from the other. Both end and bond interchange conserve the total number of micelles. Therefore, they do not contribute much to the relaxation of the micelles to equilibrium when a perturbation that changes the total number of micelles is felt like in a temperature jump (T-jump) experiment [12, 31]. For this reason, reversible scission is a more important reaction mechanism in micelle dynamics and would be the focus of this study.

1.2.3 Structural Features

Micelles exist in three concentration regimes: dilute, semi-dilute and concentrated. In dilute concentrations, the micelles are shorter than the inter-micelle distance and cannot feel the influence of surrounding micelles. Beyond an overlap concentration c*,

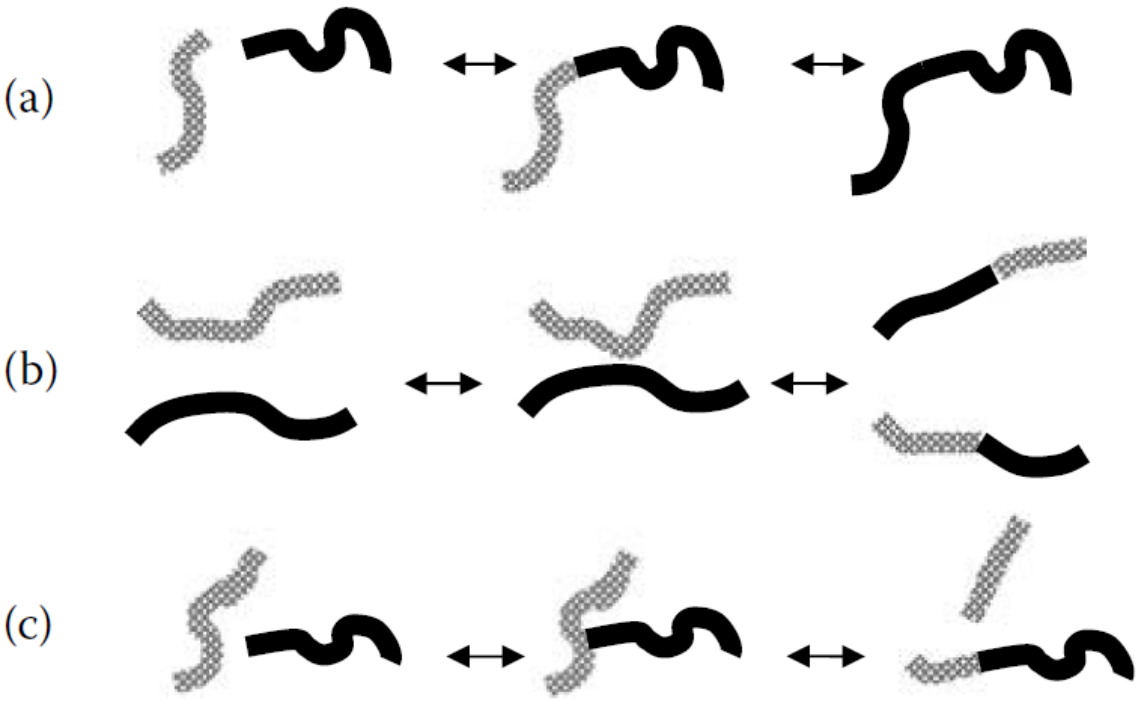

Figure 1.4: Schematic showing micellar reaction mechanisms: reversible scission (top), end interchange (middle) and bond interchange (bottom). Reproduced from [12] with permission from Taylor & Francis Group, LLC.

the micelles are longer than the inter-micelle distance and start to impose topological constraints on the diffusion of one another, thereby restricting their motion to a tube-like region. This causes the micelles to entangle with one another in what is referred to as the "loosely" entangled and semi-dilute regime [32]. Upon further aggregation, or increased concentration, the micelles elongate and become very entangled and form viscoelastic networks. This is the concentrated regime with tight entanglements. From concentrations above C^*, the linear wormlike micelles entangle with one another (and can also form branches) but maintain an isotropic configuration without a long-range orientational order [7]. Wormlike micellar (WLM) systems in this semi-dilute regime have been shown to have pronounced viscoelasticity [10, 13]. In addition to reversible scission, entangled wormlike micelles can slide along those entanglement points which are physically connected to relax stress.

Structural features such as rings are predicted to occur in the concentration region

just below the strongly entangled regime. Rings can link up and interlock to form a ring-network which could affect the rates of bond-interchange and other processes. This mechanism has been linked to shear thickening process [7]. Branches have been observed in wormlike micelles using experimental techniques such as Cryo-TEM [33]. The occurrence of branches would change the rheology of wormlike micelles in and out of equilibrium. It affords the wormlike micelles a leeway to relieve stress through a grid-like network of veins and sliding branch points. Introducing branches have caused a failure of the reptation-reaction model of Cates. This was resolved but can only be applied in wormlike micelles with relatively low counterion binding, high hydrophobicity and low ionic strength (affinity) [7].

1.3 Rheology of Wormlike Micelles

1.3.1 Linear Rheology of Wormlike Micelles

Rheological properties of micellar solutions are similar to those of polymers [34] however, their uniqueness lies in the reversibility of their structure via reversible scission. Wormlike micelles, when present at semi-dilute concentrations, exhibit pronounced viscoelasticity [10, 31]. In this concentration regime, the average micelle length is longer than the inter-micelle distance and leads to the formation of entanglements between the micelles. The implication is that the time for reptation is comparable to the wait time for a scission to occur along the contour of the long wormlike micelles. The timescales of these processes are observable within the timeframe of macroscopic rheological experiments. In small amplitude oscillatory shear flows, the linear viscoelastic response of many wormlike micelles are thus explained by a combination of reversible scission and reptation [34]. The linear rheology can be described by a two-mode Maxwell model with characteristic times scales for reptation and breakage represented by τ_{rep} and τ_b respectively [34].

1.3.1.1 Relaxation Times

Micelles at dilute concentrations, generally have low viscosities and exhibit Newtonian or near-Newtonian behavior unless they form long wormlike micelles [34, 35]. The micelle chains are relatively short that they reptate out of the surrounding constrictions before scission can occur along the chain. Reptation is thus the dominant stress relaxation mechanism [36, 11] when $\tau_b >> \tau_{rep}$, and deviation from Maxwellian behavior is observed. This has been reported in surfactant solutions at low volume fractions [10] or concentrations [36] of surfactant and salt and at low salt-to-surfactant concentration ratios. A plot of the frequency sweep exhibits a minimum in the loss modulus (G") curve at high frequencies which is roughly the inverse of the break-up time, τ_b [37]. This linear viscoelastic behavior of this category of wormlike micelles is akin to those of unentangled, unbreakable flexible polymers.

However, at semi-dilute and concentrated regimes, entanglement networks are formed and stress relaxation is by competing mechanisms of reversible scission and reptation [36]. The linear viscoelastic response of such micelles resemble that of semi-dilute to concentrated flexible-chain polymer solutions [36]. The wormlike micelles are sufficiently long that they break along their contour before they can reptate out of the surrounding constrictions. The stress decay can be modeled by a single exponential when chain scission is faster than reptation, i.e. $\tau_b << \tau_{rep}$. The characteristic time of the relaxation was predicted [30] to be equal to the geometric mean of the times for scission and reptation, $\tau = (\tau_b \tau_{rep})^{1/2}$. The signature representation for this is a perfect semi-circle plot of the relationship of the G" and G' known as the Cole-Cole plot.

Mono-exponential and Maxwellian behavior have been observed in wormlike micelle systems with high salt concentrations [38] where long and entangled wormlike micelles are present. The extent of agreement to this Maxwellian behavior depends on the micelle length, entanglement density, the concentration of free salt

ions in the bulk, and the ratio of salt to surfactant in the wormlike micelle complex [36, 38]. However, in some systems, such as cetyltrimethylammonium p-toluene sulfonate (CTApTS) with or without the hydrotrope, sodium p-toluene sulfonate (NapTS), the single mode Maxwell response has been reported to be independent of the salt-to-surfactant concentration ratios [38].

1.3.1.2 Plateau Modulus

In linear rheological experiments of Shikata and coworkers, the relaxation time τ has been reported to depend on the concentration of the free dissociated hydrotrope ions, C_S^*. The plateau modulus, G_N^0 is reported to be proportional to the square of the surfactant concentration, C_D for cationic [38, 25], anionic [24] and hybrid surfactant-polymer [39] wormlike micelles. This scaling was observed to be $G_N^0 \propto C^{9/4}$ in wormlike solutions involving CTAB and simple salts like potassium bromide (KBr) [40, 41, 42] and hydrotropes like chlorobenzoates [43]. The free hydrotrope ions in bulk aqueous phase act as catalysts for crossing-through reaction of two wormlike micelles at entanglement points, effectively controlling the entanglement release mechanism [38]. Presence of strong binding salt ions and the formation of branched micellar networks introduce new relaxation dynamics to the wormlike micelles. It allows for stress to be relaxed by the free-sliding of the branch points along the cylindrical structure of the wormlike micelles which complicates the dependence of viscosity and relaxation time on salt concentration [35].

1.3.1.3 Zero-shear Viscosity

The zero-shear viscosity scales with a power law dependence on surfactant concentration, $\eta_0 \propto C^\alpha$ with α decreasing with increasing ionic strength [43] suggesting that it is controlled by electrostatic interactions [44]. The dependence of the zero-shear viscosity on the salt concentration is logarithmically or semi-logarithmically plotted

as the "salt curve". Three types of dependences are observed. (i) the zero-shear viscosity increases to a maximum viscosity where it plateaus till phase separation occurs [45, 46] (ii) a single maximum in viscosity and (iii) double maxima of the zero-shear viscosities are observed with a minimum at intermediate concentrations.

The first type of salt curve has been observed in dilute solutions of sodium oleate (NaOA) with potassium chloride (KCl) or triethylammonium chloride (Et_3NHCl) [47]. The viscosity plateau was attributed to the electrostatic screening of the head group interactions till the head group area reaches a minimum, upon which further salt addition has no effect [45, 47].

The second behavior is reported for anionic wormlike micelle solutions with simple salts e.g. SLE3S/SLS/NaCl and sodium lauryl ether (1) sulfate (SLE1S)/NaCl (Chapter IV, [48]), anionic surfactants with hydrotropes [49, 24], mixed anionic-cationic surfactant wormlike micelles [50, 51, 52], mixtures of nonionic and ionic surfactant micelles [9, 53, 54, 55], zwitterionic with anionic or cationic surfactants [56]. The decrease in viscosity from the maximum was attributed to the formation of branches [57, 46, 58, 59] that allow faster relaxation and a reduction in the micelle length as a result of increased scission [45, 58, 57].

In the third kind of salt curve, observed in wormlike micelles composed of cationic surfactants, e.g. CTAB (Chapter IV, [48]) and CPyCl [60, 61] and hydrotropic salts, e.g. NaSal, the left peak of the cationic salt curve was attributed to elongation of the micelles and formation of highly entangled wormlike micelles [48]. The rheological behavior observed before this peak was similar to that of an entangled polymer. The relaxation could not be described by a single Maxwell time but with a continuous spectrum of relaxation times. It is indicative of multiple relaxation processes due to configurational fluctuations of the flexible chains [60]. At the regions beyond the first maximum, the linear rheology can be described as Maxwellian suggesting the importance of micelle kinetics in the relaxation in this region. The zero-shear viscosity,

η_0 then reduces towards a minimum. Although this reduction in viscosity is not predicted by the reptation-reaction model of Cates [62, 63], we believe it is attributed to a reduction of the wormlike micelle contour length due to dense entanglements and an increase in the rate of scission [33, 64] leading to shorter micelles and also aiding the relaxation of stress. The relative decrease in viscosity was associated to the formation of crosslinks between the micelles hence, branching [65] in which the branch points can slide along the micelles. The increased branching can lead to the formation of a saturated and multi-connected network [62]. The rise of η_0 to the second maximum has been subject to much debate [62, 47]. Some authors [63, 66, 67, 68] attribute it to increase in micelle branching density while others [33, 48] attribute it to the increased entanglement density or the formation of higher-order assemblies e.g. micelle bundles. The structural relaxation time, τ_R is observed to decrease after the first maximum to a minimum and increase again. However, the plateau elastic modulus, G_0 is relatively insensitive to the parameter [44, 69].

1.3.2 Nonlinear rheology of wormlike micelles

Interesting and more complicated nonlinear rheological behaviors are observed as the applied deformation exceeds the small strain limit and shear rates become strong enough to perturb the equilibrium structure [47]. WLM solutions exhibit nonlinear rheological properties such as shear banding [70, 71, 21], flow-induced phase transitions [33, 72], shear thinning, shear thickening [47] and strain hardening [73, 74, 75, 48].

1.3.2.1 Strain Hardening

Strain hardening is a solid-like behavior in which the WLMs resist deformation and exhibit an increased stiffness with increasing deformation. Strain hardening in shear is usually probed by performing step strain experiments and is defined by a nonlinear

stress relaxation modulus that increases relative to the response within the linear strain limit. A lower nonlinear relaxation modulus relative to the linear response indicates strain softening. Strain hardening has been observed at and near equal molar concentrations of CTAB with hydrotrope, NaSal [73, 74]. Shikata *et al.* [73] showed that strain hardening in aqueous solutions of CTAB with added hydrotrope, NaSal depends on the salt-to-surfactant concentration ratio. They observed that at low concentration of free salicylate ion, C_S^*, the relaxation modulus increases with strain [73] and the stress and viscosity growth function, $\eta^+ = \sigma(t, \dot{\gamma})/\dot{\gamma}$ increase with increasing rate of shear. They proposed that the strain hardening occurs due to a mechanism of entanglement relaxation [73] that cannot be predicted by Cates' nonlinear model [76] which involves reversible scission and chain retraction [75]. They noted that quantitatively similar results were obtained over the range of temperatures studied (10 - 15 ^{0}C).

Brown, Burghardt, and Venerus [74] further investigated the CTAB/NaSal solution at equal molar concentrations and observed that the Lodge-Meissner rule held for strains where strain hardening was observed. The Lodge-Meissner rule states that the ratio of first normal stress difference to shear stress is equal to the imposed step shear strain at all times. They [74] showed that the relaxation moduli were factorable into time- and strain- dependent functions in the strain hardening regime ($2.0 < \gamma < 3.5$). The strain-dependent function is calculated as the amount of vertical shift on a log-log plot needed for the nonlinear stress relaxation curve to superimpose on the linear relaxation curve. This shift as a function of strain is the damping function. Such factorability has been observed in some polymers and the damping function is usually a strain softening function [77]. For a CTAB/NaSal surfactant solution, beyond a strain of 350% ($3.5 < \gamma < 4.0$), Brown, Burghardt, and Venerus observed a time-dependent collapse of the relaxation modulus from a strain hardening to a strain softening or linear response at a critical time after the step strain [74].

In step strain experiments, strain hardening has been observed in wormlike micelles of CTAB with the hydrotrope NaSal at equal molar concentrations [74] and at a hydrotrope-to-surfactant molar concentration ratio, C_S/C_D of 1.5. [73]. However, the mechanism and conditions necessary for strain hardening in wormlike micelles is not clearly understood. The dependence of strain hardening on parameters such as salt concentration and temperature have not been studied extensively.

In start-up shear flows, an increase in the shear stress growth coefficient (defined as the ratio of shear stress to shear rate) relative to the linear response is also termed "strain hardening" [75, 25, 26]. In such start-up shear flow experiments on CTAB/NaSal wormlike micelles, Inoue, Inoue, and Watanabe [75] observed strain hardening at shear rates higher than a critical shear rate. They suggested that the molecular origin of strain hardening in the CTAB/NaSal system was the suppression of chain retraction due to sticky cross-links which act as long-lived entanglements [75]. They reported that strain hardening was strongly dependent on the effective elastic modulus — defined as the ratio of the shear stress growth function (after inception of steady shear flow) to strain — and independent of C_S^* at very high shear rate. This was attributed to the finite extensibility of the network strands described by three-chain model [75].

1.3.2.2 Shear Thickening

Shear thickening, that is, an apparent increase in viscosity with increasing shear rates [78] has been observed in wormlike micelle solutions when the solutions are sheared beyond a critical shear rate, $\dot{\gamma}_c$ or critical shear stress, σ_c [47]. This behavior has been observed in CTAB solutions with hydrotropes, NaSal and sodium tosylate. However, it was not observed with sodium benzoate although the three hydrotropes had similar chemical structures except for their polar head group. Therefore, it was concluded that shear thickening depended on the strength of the cation-π bonds

formed in the wormlike micelles and whether the hydrotrope ions intercalated in the surfactant head group [79].

The critical shear rate, $\dot{\gamma}_c$ increases with temperature, T and decreases with increasing surfactant concentration, C [80]. It varies with both parameters according to $\dot{\gamma}_c \approx C^{\alpha} exp(-E_a/k_B T)$ where E_a is the activation energy [81, 47]. Upon shearing the solutions beyond the critical shear rate or stress, a wait time, t_{ind} is observed before a 20-50 fold increase in viscosity [80, 47]. It then takes another t_{sat} for the viscosity to attain a steady value. t_{ind} and t_{sat} depend on the shear and thermal histories of the solutions. t_{ind} is the time for shear-thickening transition ranging from seconds to minutes. During this time, shear-induced structures are formed in the solution which leads to the increase in viscosity. A power-law dependence of $t_{ind} \approx \dot{\gamma}^{-m}$ on the shear rate is reported [82, 83]. Flow-induced structures have not been reported for purely extensional flows [47]. However, in mixed shear and extensional flows, obtained by flowing the wormlike micelles through micro-posts, the formation of stable flow-induced structured phase was obtained [84, 33].

Shear thickening and the actual morphology of the shear-induced structures formed in dilute surfactant solutions have been explained with two arguments: the shear-induced transition and the shear-induced phase. In the shear-induced transition argument, two structures - short rod-like micelles and aligned wormlike micelles- are believed to co-exist in the same phase. As the shear rate exceeds $\dot{\gamma}_c$, the small rod-like micelles aggregate further and align under flow. The geometry gap is thus filled with aligned wormlike micelles. t_{ind} and t_{sat} are then said to represent the time for aggregation of rod-like micelles to a critical aggregation size and the time for the growth of aligned wormlike micelles respectively [80, 85, 82, 47]. The shear-induced phase argument postulates that a flow-induced phase separation of the wormlike micelles occur and results in a highly viscous gel phase and a low viscosity sol phase containing smaller micelles [78, 47, 33, 79, 80, 86]. Both points of views have been supported

by rheo-optical techniques such as flow birefrigence [82], Rheometry on Small Angle Light Scattering (Rheo-SALS) [87, 88, 89] and Rheometry on Small Angle Neutron Scattering (Rheo-SANS) [86, 85, 81, 90, 91].

1.3.2.3 Shear banding

Shear banding occurs as a result of the stratification of the flow into distinct regions of varying shear rates, viscosities and morphologies [92]. It is observed on a shear stress-shear rate flow curve as a discontinuity between two critical shear rates, $\dot{\gamma}_{c1}$ and $\dot{\gamma}_{c2}$ in which a stress plateau [47] or non-monotonic trend occurs [93]. Newtonian behavior is typically observed at shear rates below $\dot{\gamma}_{c1}$ and above $\dot{\gamma}_{c2}$ [47]. The flow in the aforementioned regions are homogeneous and stable. However, at shear rates between both critical shear rates, $\dot{\gamma}_{c1} < \dot{\gamma} < \dot{\gamma}_{c2}$, a negative slope in the flow curve implies decreasing stress with increasing shear rate. The initially homogeneous flow becomes mechanically unstable [94]. The non-monotonic flow curve is thus attributed to mechanical instability [94, 47] which can be exacerbated by concentration fluctuations [95]. This mechanism has been invoked to explain shear banding in semi-dilute micelle solutions [47].

Another explanation of the stress plateau informed by Rheo-SANS [72, 96, 80], Rheo-SALS [97] and birefringence studies [96, 82] under shear attribute the stress plateau to an isotropic-nematic phase transition in concentrated wormlike micelle solutions near the equilibrium isotropic/nematic phase boundary [94]. The region before the plateau was characterized as a homogeneous flow of isotropic micelles while that after the plateau was determined to be homogeneous flow of nematic micelles. The flow region spanning the stress plateau was characterized as an inhomogeneous and biphasic (isotropic/nematic) flow with shear rates relative to the proportions of both phases [94]. Start-up experiments [94] reveal both the flow-induced phase transition occur on a different timescale, $t > \tau_R$ than the mechanical instability which occurs

after stress overshoots at about τ_R [94]. The shear bands were reportedly triggered by shear causing non-equilibrium phase transitions. However, both mechanisms of phase transitions and mechanical instabilities seem intertwined [94, 47].

Shear bands have been observed along the gradient and vorticity directions and are referred to as gradient [93, 47, 80, 97, 82, 92, 98] and vorticity shear banding respectively [93, 99, 80, 92, 98]. Gradient banding have been linked to micelle alignment and concentration fluctuations [93, 100]. Vorticity banding have been attributed to normal stress differences across bands, viscoelastic instabilities (in curved streamlines) and fluctuating slip in the high shear rate band [93, 101, 102]. Shear banding has also been associated with long transients that are longer than the relaxation times [99], elastic instabilities [103, 104], oscillating bands [101, 93], spatiotemporal rheo-chaos [105] and interfacial instabilities [93, 106, 101, 102, 107].

1.3.3 Constitutive Equations

Macromolecules form transient networks that have the ability to break and recombine dynamically in solution and are known to exhibit remarkably different rheological properties from ordinary polymers solutions including shear thickening, shear banding, strain hardening and thixotropy [108]. To accurately predict these unique rheological properties, the constitutive equations used to describe the stress-strain relationships of these macromolecules have to reflect the reversibility of their structure. Hence, there is the need to develop constitutive equations for wormlike micelles that include reversible scission. Unlike polymer solutions, whose response to different deformations have been studied and reported in classical texts [20, 77, 109], few models include both reversible scission and deformation dynamics in their description of the stress response of micelles. In this section, we would briefly review theories for polymer rheology, transient network theories that include reversibility of structure and theories for wormlike micelles that aim to build on ideas from polymer and transient

network theories.

1.3.3.1 Tube Model and Reptation Theory for Polymers

A flexible polymer chain in a semi-dilute or concentrated solution is surrounded by other chains that constrict its motion. The effect of the surrounding chains can be represented as a tube [109]. The chain is in a random walk configuration, therefore the tube also follows a random walk configuration. The tube has a diameter, a with a step-length, b [7]. The polymer chain can therefore only free itself of the constraints by a curvilinear diffusion along the axis of the tube known as reptation [110, 30, 7]. The curvilinear diffusion constant, D_c is inversely proportional to the chain length, L, i.e. $D_c = D_0/L$, where $D_0 = k_B T/\zeta$ is the diffusivity or mobility constant, independent of L [30]. The fraction of the original tube remaining at time, t after a small step-strain, γ is [109]

$$\mu(t) = \sum_{p=odd} \frac{8}{p^2\pi^2} exp[-tp^2/\tau_{rep}] \tag{1.1}$$

where $\tau_{rep} = L^2/D_c\pi^2$ is the reptation time.

If the polymer is suddenly deformed by applying a small shear strain, γ, the deformation tensor, $E_{ij} = \delta_{ij} + \gamma\delta_{ix}\delta jy$. The corresponding stress tensor, σ_{ij} has the following non-zero deviatoric components,

$$\sigma_{yx} = \sigma_{xy} = G(t - t_1)\gamma \tag{1.2}$$

Linearity demands that the other deviatoric components of σ_{ij} are zero by symmetry [7]. $G(t)$ is the linear step-strain response. Applying a time-dependent shear strain, $\gamma(t)$, the strain can be fragmented into infinitesimally small strains, $\dot{\gamma}(t')dt'$ by linearity. The stress response is therefore, $d\sigma_{xy}(t) = G(t - t')\dot{\gamma}(t')dt'$ which can be

integrated to give the constitutive equation for linear deformations

$$\sigma_{xy}(t) = \int_{-\infty}^{t} G(t-t')\dot{\gamma}(t')dt' \tag{1.3}$$

If a nonlinear step-strain is suddenly applied at t_1, the modulus becomes a factor of both time and strain. The stress response is of the form,

$$\sigma_{yx} = \sigma_{xy} = G(t-t_1,\gamma)\gamma \tag{1.4}$$

In contrast to the linear case, the other deviatoric components of σ_{ij} do not varnish by symmetry. First and second normal stress differences are defined as $N_1 = \sigma_{xx} - \sigma_{yy}$ and $N_2 = \sigma_{yy} - \sigma_{zz}$ respectively. The stress response of the deformed polymer chain in the tube, and assuming independent alignment approximation [109] is given as

$$\sigma_{ij}^{pol}(t) = G_0 \int_{-\infty}^{t} \dot{\mu}(t-t')Q_{ij}(E_{mn}^{tt'})dt' \tag{1.5}$$

where tensor Q_{ij} is a function of deformation tensor, $E_{mn}^{tt'}$ which represents the deformation felt by the tube segments between times t' and t. The product, $G_0 Q_{ij}$ gives the stress contribution [7]. Further details about the proof of Eq. (1.5) can be found in the text by Doi and Edwards [109].

1.3.3.2 Cates' Reptation-Reaction Model

Cates' reptation-reaction model [30] was introduced in Section 1.3.1.1. In this model, he incorporated micelle kinetics into the reptation theory developed by [109] and summarized in Section 1.3.3.1. The model is based on the following assumptions: (i) scission occurs at a fixed probability per unit length per unit time anywhere along the length of the chain, L (ii) fusion occurs at a rate proportional to the product

of the concentrations of the fusing subchains, and (iii) successive scission and fusion events are uncorrelated, i.e. a chain is equally likely to fuse with a random chain in the vicinity as it is with the chain it recently dissociated from [30]. Based on these assumptions, the micelle kinetics yields a distribution of lengths of micelles in steady state given by,

$$N(L) = (2c_1/c_2)exp(-L/\bar{L}) \tag{1.6}$$

where, c_1 and c_2 are the rate constants for scission and fusion respectively. $\bar{L}$, the mean chain length depends on the rate constants according to

$$\bar{L} = \rho c_2/2c_1 \tag{1.7}$$

ρ is the contour length of micelles per unit volume of solution

$$\rho = \int_0^\infty LN(L)dL \tag{1.8}$$

with $N(L)dL$ being the number density of chains of length $L \pm 1/2dL$. The characteristic time for a chain of mean length, $\bar{L}$ to break in two is defined as

$$\tau_b = (c_1\bar{L})^{-1} \tag{1.9}$$

When $\tau_b << \tau_{rep}$, reversible scission occurs before the chain ends can reptate out of the tube. Therefore, the dominant relaxation mechanism for a tube segment not close to a chain end is such that when the chain breaks along the contour, at a distance λ from the tube segment, the newly formed chain end reptates past the tube segment before it is fused with a neighboring chain [30]. The largest distance, λ at which a break can occur for relaxation by this mechanism is given by $\lambda^2 \cong D_c(L)\tau_b$. Assuming

the length of the newly broken chain, L is of mean length, $\bar{L}$, then

$$\lambda^2 \cong D_0 \bar{L}^{-2} / c_1 = \bar{L}^2 \zeta \quad (\zeta << 1) \tag{1.10}$$

where $\zeta = \tau_b / \tau_{rep}$. Taking λ as the mean chain length, $\bar{L}$ and substituting Eq. (1.10) in Eq. (1.9), the relaxation time for the tube segment by the described mechanism is obtained as [30]

$$\tau \cong (c_1 \lambda)^{-1} \cong D_0^{-1/2} c_1^{-1/2} \bar{L} \tag{1.11}$$

Eq. (1.11) can be re-written as

$$\tau \simeq (\tau_b \tau_{rep})^{1/2} \quad (\zeta \leq 1) \tag{1.12}$$

When $\bar{\zeta} = \tau_) b / \tau << 1$, the relaxation function $\mu(t) = exp[-t/\tau]$ is a mono-exponential decay with a single relaxation time [30, 7] as discussed in Section 1.3.1.1. When $\zeta < N_T^{-1}$, where N_T is the number of tube segments per average micelle chain, the dominant relaxation mechanism is no longer reptation but contour length fluctuations (CLF) or "breathing" [7]. CLF accounts for changes in the contour length of the tube in time [32]. In the breathing regime, the mean stress relaxation time is corrected as [30]

$$\tau \simeq \tau_b^{3/4} \tau_{rep}^{1/4} N_T^{1/4} \tag{1.13}$$

The time for stress relaxation by breathing relative to reptation is set by the number of entanglements, $\bar{Z}$ on the average micelle of chain length, $\bar{L}$ [32]. Deviations from Maxwell behavior such as an up-turn in the storage and loss moduli at high frequency is observed [7].

Cates [76] extended his reptation-reaction model [30] to describe nonlinear effects by assuming that (i) nonlinear effects of the flow are introduced only through the effects on micelle diffusion. Such effects on scission/fusion rates are neglected; and

(ii) stress contribution is dominated by micelle entropy [76]. The constitutive equation is given as [7] in terms of the deviatoric part of the polymer stress

$$\sigma_{ij}^{pol,dev} = \frac{15}{4} G_0 \left[W_{ij} - \frac{\delta_{ij}}{3} \right] \tag{1.14}$$

$$W_{ij}(t) = \int_{-\infty}^{t} \mathcal{B}(\nu(t')) exp \left[- \int_{t'}^{t} \mathcal{D}(\nu(t")) \right] Q_{ij}(E_{mn}^{tt'}) dt' \tag{1.15}$$

$$\nu(t) = W_{ij}(t) K_{ij}(t) \tag{1.16}$$

$$Q_{ij}(E_{mn}) = \left\langle \frac{E_{ik} u_k E_{jl} u_l}{|E_{im} u_m|} \right\rangle_0 \tag{1.17}$$

The Cates' nonlinear reptation-reaction model predicts nonlinear rheological properties such as flow-instabilities characteristic of shear banding [111]. The shear banding behavior is reviewed in Section 1.3.2.3.

Further modifications were applied to the Cates' reptation-reaction model to suit pairwise associating polymers [112], and including new physics previously neglected: breathing with high frequency Rouse modes [113, 114], contour length fluctuations [115, 32], longitudinal relaxation of stress along the tube [115], (convective and reptation-driven) constraint release [116, 117, 115, 118, 32], chain stretch [118], micelle bending modes, constraint release or tube rearrangement, correlations of micelle lengths after reversible scission with that before it occurred; with a view of accurately predicting the micelle rheology even in the crossover regime between "loosely" and "tightly" entangled micelle solutions [32].

1.3.3.3 Transient Network Theories

Several approaches have been considered to include micelle reaction kinetics such as reversible scission in constitutive equations. Bond interchange for instance, proceeds through a four-armed intermediate to exchange two interior bonds without the

need of a chain end (see Section 1.2.2). Therefore, in such a case the tube model might be inapplicable [76], and network theories capable of tracking the state and dynamics of chain segments in a network would be more suitable. Transient network theories are based on classical network theories for rubber elasticity. In the network theories for rubber (and other solids), the chemical crosslinks are treated as junctions that move connected network segments together. However, for macromolecular liquids, the junctions are treated as temporary, in the sense that they can be created and destroyed [20].

These transient network theories can be categorized into single-, two- and three-species models. The single species models incorporate reversible scission into their constitutive equations by defining a kinetic or reactionary term and coupling it with the equation for the deformation dynamics. Bautista et. al [119] coupled a kinetic equation for the creation and destruction of structure to the Upper Convected Maxwell equation. Their model could predict thixotropy, rheopexy and creep in transient stress cycles. Hernández Cifre et. al [120] presented a pseudo-two-species model of two ensembles of dumbbells, one for 'active' chains which are connected to the network by both ends and the other for 'dangling' chains which connect to the network by one end only. There is no explicit exchange of species in their model. However, transition probabilities were defined for the association of dangling chains to the network to form active chains and vice versa. The ensembles were thus differentiated by characterizing the attached beads of the dangling and active chains with a friction coefficient that lowers its effective diffusivity. The model predicts shear thickening and shear thinning. Although the single species models have been able to predict some nonlinear rheological phenomena, they have two major disadvantages. First, the models do not account for the topological changes of the species or network during reversible scission and secondly, there is no interaction (exchange) of species during the reversible scission.

Two-species and three-species models account for the exchange in species by introducing equations for the evolution of the number densities of the interacting species. One of such models is proposed by van den Brule et al. [108] based on the model of Tanaka and Edwards [121]. Van den Brule and coworkers performed Brownian dynamics simulations of cross-linked gels modeled as polymeric networks. In their work, the dynamics of the system is governed by the association and dissociation of "crosslinks" in the polymer network and Brownian motion. They represented the macromolecules as Hookean dumbbells with two beads and a spring, and nodes which connect to beads within a critical distance and move together with them in the fluid. The chains exist in two states: 'dangling' and 'active'. Van den Brule et al. assumed linear spring force law and a fixed rate of dissociation of the beads from the nodes.

Despite these limitations, they observed shear thickening behavior of the polymeric network. The shear thickening was attributed to higher association probability of long dangling segments to the network before they can completely relax to equilibrium. The higher association probability results from the quicker retraction of the long dangling segments due to their higher elasticity compared to shorter segments. Also, a retracting long segment has a larger configuration space to explore and a greater chance of re-associating with the network than a short segment. Thus, the probability of association increases with segment length [108].

Vaccaro and Marrucci [122] employed closure approximations to obtain a constitutive equation for similar structures simulated by [108]. They observed shear thickening at the onset of nonlinear response followed by shear thinning at higher shear rates. Tripathi et al. [123] incorporated finite extensibility of the chains, a stretch-induced dissociation rate, and a shear-induced rate of association of dangling chains to the elastic network described in previous work [108, 120]. They also observed shear thickening followed by shear thinning at higher shear rates and scaling of the network relaxation time and zero-shear viscosity that were comparable to those

obtained in experiments [123].

1.3.3.4 Macroscopic Constitutive Equations

The constitutive equation of Bautista *et al.* [124] relies on the formulation of a parameter, namely shear band intensity coefficient, to make predictions without relating the parameter to the microstructure of the wormlike micelles.

Cates [112] improved on their earlier model [30] to account for interactions of pairwise associating polymers with end-groups such that 'monomers' could combine into 'dimers' and 'dimers' could break into 'monomers'. With this framework, he was able to establish relationships between the zero-shear viscosity and the equilibrium ratio of dimers to monomers. Despite the possible predictions including shear banding [111] made by this model, the fundamental fixed-tube assumption [30] implies that the chains do not stretch even during nonlinear flows [76]. To permit chain stretch with deformation, the Vasquez-Cook-McKinley (VCM) model [125] incorporated reversible scission into the elastic network response of a discrete, two-species wormlike micelle model. Similar to Cates' [112], they modeled the micelles as two different species, one of length L that breaks to form two strands of equal length, $L/2$; these strands can rejoin to form a species of length L. The reversible scission in this model was developed as a simplification of the reaction kinetics proposed by Cates [30]. Germann et al. [126] refined the work of [125] to produce a three-species model in which short micelles of length, L could combine to form intermediate micelles of length, $2L$ which can further join to form a longer micelle of length, $4L$.

The VCM model was able to predict flow instability of the shear-banding type. However, we believe dimensionality problems in the formulation of the model would pose errors in the predictions by the model. Comparisons of the VCM model to analogous Brownian dynamics (BD) simulations in Chapter II reveal inadequacies in depicting the micelle reversible scission kinetics using dumbbell models.

1.4 Organization of the Dissertation

In this dissertation, we seek to understand nonlinear rheological phenomena in wormlike micelles. We employ rheological experiments, simulations and theory to achieve this.

In Chapter II, we validate the predictions of the Vasquez-Cook-McKinley (VCM) constitutive equations using parallel Brownian dynamics (BD) simulations. Based on our findings, we develop a novel constitutive equation that addresses the shortcomings of the VCM model and can accurately predict nonlinear rheological behaviors in transient and steady states. The method can be extended to nonlinear force-extension relationships.

In Chapter III, we incorporate slip-springs into the BD simulation developed in Chapter II to simulate wormlike micelles in the semi-dilute and concentrated regimes. The slip-springs act as entanglements to the simulated micelle chains. We study the effects of the entanglements on the micelle rheology vis-a-vis reversible scission kinetics.

In Chapter IV, we investigate systematically the effect of salt concentration and temperature on the strain hardening of different kinds of wormlike micelle solutions by performing step-strain measurements on a rheometer. We analyze the findings and provide insights into plausible mechanisms of stain hardening in wormlike micelles.

Finally, in Chapter V we conclude and give future directions for the work based on our findings.

Bibliography

[1] T. Hughes, E. Nelson, P. Sullivan, and V. Anderson, in *Giant Micelles*, Surfactant Science (CRC Press, 2007) pp. 453–472.

[2] Y. Feng, Z. Chu, and C. A. Dreiss, *Smart Wormlike Micelles*, SpringerBriefs in Molecular Science (Springer Berlin Heidelberg, Berlin, Heidelberg, 2015).

[3] J. Yang, Current Opinion in Colloid & Interface Science **7**, 276 (2002).

[4] D. Myers, *Surfactant science and technology*, 3rd ed. (John Wiley & Sons, 2005) p. 448.

[5] M. J. Lawrence, "Surfactant systems: their use in drug delivery," (1994).

[6] J. Barber, "Change the Way You Spray to Minimize Clogging," (2008).

[7] M. E. Cates and S. M. Fielding, Advances in Physics **55**, 799 (2006), arXiv:0702047 [cond-mat] .

[8] Z. Chu, C. A. Dreiss, and Y. Feng, Chemical Society Reviews **42**, 7174 (2013).

[9] D. P. Acharya and H. Kunieda, Advances in colloid and interface science **123-126**, 401 (2006).

[10] L. J. Magid, The Journal of Physical Chemistry B **102**, 4064 (1998).

[11] S. Ezrahi, E. Tuval, and A. Aserin, Advances in colloid and interface science **128-130**, 77 (2006).

[12] G. Waton and R. Zana, in *Giant Micelles*, Surfactant Science (CRC Press, 2007) pp. 323–349.

[13] E. Kaler and R. Zana, *Giant Micelles*, edited by E. Kaler and R. Zana, Surfactant Science, Vol. 20074445 (CRC Press, 2007) p. 2013.

[14] R. Abdel-Rahem, Advances in colloid and interface science **141**, 24 (2008).

[15] A. Bernheim-Groswasser, R. Zana, and Y. Talmon, The Journal of Physical Chemistry B **104**, 4005 (2000).

[16] R. Nagarajan, in *Giant Micelles*, Surfactant Science (CRC Press, 2007) pp. 1–40.

[17] A. Bernheim-Groswasser, E. Wachtel, and Y. Talmon, Langmuir **16**, 4131 (2000).

[18] D. Danino, Colloids and Surfaces A: Physicochemical and Engineering Aspects **183-185**, 113 (2001).

[19] M. Almgren, J.-E. Löfroth, and R. Rydholm, Chemical Physics Letters **63**, 265 (1979).

[20] R. B. Bird, F. C. Curtiss, C. R. Amstrong, and H. Ole, *Wiley-Interscience*, 2nd ed., Vol. 2 (John Wiley & Sons, New York, 1987) p. 464.

[21] J. F. Berret, in *Molecular Gels: Materials with Self-Assembled Fibrillar Networks*, edited by R. Weiss and P. Terech (Springer Netherlands, 2006) pp. 667–720.

[22] C. A. Dreiss, Soft Matter **3**, 956 (2007).

[23] M. Takeda, T. Kusano, T. Matsunaga, H. Endo, M. Shibayama, and T. Shikata, Langmuir **27**, 1731 (2011).

[24] K. Nakamura and T. Shikata, Langmuir **22**, 9853 (2006).

[25] K. Nakamura and T. Shikata, Nihon Reoroji Gakkaishi **36**, 167 (2008).

[26] K. Nakamura, S. Takase, and T. Shikata, Nihon Reoroji Gakkaishi **38**, 31 (2010).

[27] R. Kumpf and D. Dougherty, Science **261**, 1708 (1993).

[28] J. C. Ma and D. A. Dougherty, Chemical Reviews **97**, 1303 (1997).

[29] D. A. Dougherty, Accounts of Chemical Research **46**, 885 (2013).

[30] M. E. Cates, Macromolecules **20**, 2289 (1987).

[31] M. Cates and S. Fielding, in *Giant Micelles*, Surfactant Science (CRC Press, 2007) pp. 109–161.

[32] W. Zou and R. G. Larson, Journal of Rheology **58**, 681 (2014).

[33] J. J. Cardiel, A. C. Dohnalkova, N. Dubash, Y. Zhao, P. Cheung, and A. Q. Shen, Proceedings of the National Academy of Sciences of the United States of America **110**, E1653 (2013).

[34] M. E. Cates and S. J. Candau, Journal of Physics: Condensed Matter **2**, 6869 (1990).

[35] H. Rehage and H. Hoffmann, Molecular Physics **74**, 933 (1991).

[36] T. Shikata, H. Hirata, and T. Kotaka, Langmuir **3**, 1081 (1987).

[37] F. Kern, F. Lequeux, R. Zana, and S. J. Candau, Langmuir **10**, 1714 (1994).

[38] T. Shikata, M. Shiokawa, and S.-I. Imai, Journal of Colloid and Interface Science **259**, 367 (2003).

[39] K. Nakamura and T. Shikata, Macromolecules **37**, 8381 (2004).

[40] S. Candau, E. Hirsch, R. Zana, and M. Adam, Journal of Colloid and Interface Science **122**, 430 (1988).

[41] T. Shikata and T. Kotaka, Journal of Non-Crystalline Solids **131-133**, 831 (1991).

[42] A. Khatory, F. Lequeux, F. Kern, and S. J. Candau, Langmuir **9**, 1456 (1993).

[43] M. In, in *Giant Micelles*, Surfactant Science (CRC Press, 2007) pp. 249–287.

[44] H. Hoffmann and W. Ulbricht, Surfactant science series **70**, 285 (1997).

[45] J.-H. Mu and G. Z. Li, Colloid & Polymer Science **279**, 872 (2001).

[46] D. Angelescu, A. Khan, and H. Caldararu, Langmuir **19**, 9155 (2003).

[47] J. Felix Armando Soltero, F. Bautista, J. Puig, and O. Manero, in *Giant Micelles*, Surfactant Science (CRC Press, 2007) pp. 289–322.

[48] A. A. Adams, M. J. Solomon, R. G. Larson, and X. Xia, Journal of Rheology **61**, 967 (2017).

[49] P. a. Hassan, S. R. Raghavan, and E. W. Kaler, Langmuir **18**, 2543 (2002).

[50] S. R. Raghavan, G. Fritz, and E. W. Kaler, Langmuir **18**, 3797 (2002).

[51] R. D. Koehler, S. R. Raghavan, and E. W. Kaler, Journal of Physical Chemistry B **104**, 11035 (2000).

[52] B. A. Schubert, E. W. Kaler, and N. J. Wagner, Langmuir **19**, 4079 (2003).

[53] C. Rodriguez, D. P. Acharya, K. Hattori, T. Sakai, and H. Kunieda, Langmuir **19**, 8692 (2003).

[54] C. Rodriguez, D. P. Acharya, A. Maestro, K. Hattori, K. Aramaki, and H. Kunieda, Journal of Chemical Engineering of Japan **37**, 622 (2004).

[55] D. P. Acharya, K. Hattori, T. Sakai, and H. Kunieda, Langmuir **19**, 9173 (2003).

[56] H. Hoffmann, A. Rauscher, M. Gradzielski, and S. F. Schulz, Langmuir **8**, 2140 (1992).

[57] M. In, G. G. Warr, and R. Zana, Physical Review Letters **83**, 2278 (1999).

[58] J. H. Mu, G. Z. Li, and Z. W. Wang, Rheologica Acta **41**, 493 (2002).

[59] J.-H. Mu, G.-Z. Li, X.-L. Jia, H.-X. Wang, and G.-Y. Zhang, The Journal of Physical Chemistry B **106**, 11685 (2002).

[60] H. Rehage and H. Hoffmann, The Journal of Physical Chemistry **92**, 4712 (1988).

[61] E. Kaler and F. Nettesheim, in *Giant Micelles*, Surfactant Science (CRC Press, 2007) pp. 223–247.

[62] F. Lequeux, Europhysics Letters (EPL) **19**, 675 (1992).

[63] E. Cappelaere and R. Cressely, Colloid and Polymer Science **275**, 407 (1997).

[64] T. Shikata, H. Hirata, and T. Kotaka, Langmuir **4**, 354 (1988).

[65] a. Khatory, F. Kern, F. Lequeux, J. Appel, G. Porte, N. Morie, a. Ott, and W. Urbach, Langmuir , 933 (1993).

[66] E. Cappelaere and R. Cressely, Colloid & Polymer Science **276**, 1050 (1998).

[67] M. E. Helgeson, T. K. Hodgdon, E. W. Kaler, and N. J. Wagner, Journal of colloid and interface science **349**, 1 (2010).

[68] S. A. Rogers, M. A. Calabrese, and N. J. Wagner, Current Opinion in Colloid and Interface Science **19**, 530 (2014).

[69] H. Hoffmann, in *Structure-Performance Relationships in Surfactants*, Surfactant Science (CRC Press, 2003).

[70] P. D. Olmsted, Rheologica Acta **47**, 283 (2008).

[71] J. K. G. Dhont and W. J. Briels, Rheologica Acta **47**, 257 (2008).

[72] J.-F. Berret, D. C. Roux, and G. Porte, Journal de Physique II **4**, 1261 (1994).

[73] T. Shikata, H. Hirata, E. Takatori, and K. Osaki, Journal of Non-Newtonian Fluid Mechanics **28**, 171 (1988).

[74] E. Brown, W. Burghardt, and D. Venerus, Langmuir **7463**, 3902 (1997).

[75] T. Inoue, Y. Inoue, and H. Watanabe, Langmuir : the ACS journal of surfaces and colloids **21**, 1201 (2005).

[76] M. E. Cates, The Journal of Physical Chemistry **94**, 371 (1990).

[77] R. Larson, *Constitutive equations for polymer melts and solutions* (Butterworth Publishers, 1988).

[78] M. Vasudevan, A. Shen, B. Khomami, and R. Sureshkumar, Journal of Rheology **52**, 527 (2008), arXiv:0706.3063 .

[79] V. Hartmann and R. Cressely, Colloid & Polymer Science **276**, 169 (1998).

[80] J. F. Berret, R. Gamez-Corrales, J. Oberdisse, L. M. Walker, P. Lindner, R. Gámez-Corrales, J. Oberdisse, L. M. Walker, and P. Lindner, Europhysics Letters **41**, 677 (1998).

[81] R. Gamez-Corrales, J.-F. Berret, L. M. Walker, and J. Oberdisse, Langmuir **15**, 6755 (1999).

[82] J. F. Berret, S. Lerouge, and J. P. Decruppe, Langmuir **18**, 7279 (2002).

[83] E. R. Macías, F. Bautista, J. F. a. Soltero, J. E. Puig, P. Attané, and O. Manero, Journal of Rheology **47**, 643 (2003).

[84] M. Vasudevan, E. Buse, D. Lu, H. Krishna, R. Kalyanaraman, A. Q. Shen, B. Khomami, and R. Sureshkumar, Nature Materials **9**, 436 (2010).

[85] J.-F. F. Berret, R. Gamez-Corrales, Y. Séréro, F. Molino, and P. Lindner, Europhysics Letters **54**, 605 (2001).

[86] J.-F. Berret, D. Roux, and P. Lindner, The European Physical Journal B **5**, 67 (1998).

[87] C. Oelschlaeger, G. Waton, E. Buhler, S. J. Candau, and M. E. Cates, Langmuir **18**, 3076 (2002).

[88] E. Buhler, C. Oelschlaeger, G. Waton, and S. J. Candau, Journal of Physical Chemistry B **108**, 11236 (2004).

[89] C. Oelschlaeger, G. Waton, S. J. Candau, and M. E. Cates, Langmuir **18**, 7265 (2002).

[90] R. Oda, V. Weber, P. Lindner, D. J. Pine, E. Mendes, and F. Schosseler, Langmuir **16**, 4859 (2000).

[91] M. T. Truong and L. M. Walker, Langmuir **16**, 7991 (2000).

[92] S. M. Fielding, Soft Matter **3**, 1262 (2007).

[93] Y. Kim, A. Adams, W. H. Hartt, R. G. Larson, and M. J. Solomon, Journal of Non-Newtonian Fluid Mechanics **232**, 77 (2016).

[94] J.-F. Berret, Langmuir **13**, 2227 (1997).

[95] S. M. Fielding and P. D. Olmsted, European Physical Journal E **11**, 65 (2003), arXiv:0302098 [cond-mat] .

[96] E. Cappelaere, J. F. Berret, J. P. Decruppe, R. Cressely, and P. Lindner, Physical Review E - Statistical Physics, Plasmas, Fluids, and Related Interdisciplinary Topics **56**, 1869 (1997).

[97] J. P. Decruppe, S. Lerouge, and J. F. Berret, Physical Review E - Statistical Physics, Plasmas, Fluids, and Related Interdisciplinary Topics **63**, 4 (2001).

[98] S. Manneville, Rheologica Acta **47**, 301 (2008), arXiv:0903.5389 .

[99] C. R. López-Barrón, a. K. Gurnon, A. P. R. Eberle, L. Porcar, and N. J. Wagner, Physical Review E - Statistical, Nonlinear, and Soft Matter Physics **89**, 042301 (2014).

[100] a. K. Gurnon, C. R. Lopez-Barron, A. P. R. Eberle, L. Porcar, and N. J. Wagner, Soft Matter **10**, 2889 (2014).

[101] M. A. Fardin, T. Divoux, M. A. Guedeau-Boudeville, I. Buchet-Maulien, J. Browaeys, G. H. McKinley, S. Manneville, and S. Lerouge, Soft Matter **8**, 2535 (2012).

[102] A. Nicolas and A. Morozov, Physical Review Letters **108** (2012), 10.1103/PhysRevLett.108.088302, arXiv:arXiv:1201.1492v1 .

[103] L. Casanellas, C. J. Dimitriou, T. J. Ober, and G. H. McKinley, Journal of Non-Newtonian Fluid Mechanics **222**, 234 (2014).

[104] T. Divoux, M. A. Fardin, S. S. Manneville, and S. Lerouge, Annual Review of Fluid Mechanics **48**, 13 (2016), arXiv:1503.04130 .

[105] A. Aradian and M. E. Cates, Europhysics Letters **70**, 397 (2005), arXiv:0410509 [cond-mat] .

[106] X. F. Yuan, Europhysics Letters **46**, 542 (1999).

[107] H. J. Wilson and S. M. Fielding, Journal of Non-Newtonian Fluid Mechanics **138**, 181 (2006), arXiv:0511114 [cond-mat] .

[108] B. van den Brule and P. Hoogerbrugge, Journal of Non-Newtonian Fluid Mechanics **60**, 303 (1995).

[109] M. Doi and S. F. Edwards, *The theory of polymer dynamics* (Oxford University Press, Oxford, 1986) p. 391.

[110] P.-G. de Gennes, *Scaling Concepts in Polymer Physics*, 1st ed. (Cornell University Press, Ithaca and London, 1979) p. 326.

[111] N. a. Spenley, M. E. Cates, and T. C. B. McLeish, Physical Review Letters **71**, 939 (1993).

[112] M. E. Cates, Macromolecules **21**, 256 (1988).

[113] R. Granek and M. E. Cates, The Journal of Chemical Physics **96**, 4758 (1992).

[114] R. Granek, Langmuir **10**, 1627 (1994).

[115] A. A. E. Likhtman and T. T. C. B. McLeish, Macromolecules **35**, 6332 (2002).

[116] G. Marrucci, Journal of Non-Newtonian Fluid Mechanics **62**, 279 (1996).

[117] S. T. Milner, T. C. B. McLeish, and A. E. Likhtman, Journal of Rheology **45**, 539 (2001).

[118] R. S. R. Graham, A. A. E. Likhtman, T. C. B. McLeish, and S. T. Milner, Journal of Rheology **47**, 1171 (2003).

[119] F. Bautista, J. de Santos, J. Puig, and O. Manero, Journal of Non-Newtonian Fluid Mechanics **80**, 93 (1999).

[120] J. Hernández Cifre, T. Barenbrug, J. Schieber, and B. van den Brule, Journal of Non-Newtonian Fluid Mechanics **113**, 73 (2003).

[121] F. Tanaka and S. F. Edwards, Macromolecules **25**, 1516 (1992).

[122] A. Vaccaro and G. Marrucci, Journal of Non-Newtonian Fluid Mechanics **92**, 261 (2000).

[123] A. Tripathi, K. C. Tam, and G. H. McKinley, Macromolecules **39**, 1981 (2006).

[124] F. Bautista, J. F. A. Soltero, J. H. Pérez-López, J. E. Puig, and O. Manero, Journal of Non-Newtonian Fluid Mechanics **94**, 57 (2000).

[125] P. a. Vasquez, G. H. McKinley, and L. Pamela Cook, Journal of Non-Newtonian Fluid Mechanics **144**, 122 (2007).

[126] N. Germann, L. Cook, and A. Beris, Journal of Non-Newtonian Fluid Mechanics **196**, 51 (2013).

CHAPTER II

A Nonlinear Kinetic-Rheology Model for Reversible Scission and Deformation of Worm-like micelles

2.1 Introduction

While many simple and sophisticated nonlinear constitutive equations have been developed for polymer solutions and melts, few are available for solutions of worm-like micelles. Since worm-like micelles behave as "living polymers," many aspects of their dynamics are similar to those of polymers, and theories for polymers can inform the development of models for the dynamics and rheology of worm-like micelles. This strategy has been particularly successful in the development of a theory for the linear rheology of entanglement wormlike micelles by Cates [1]. Cates' theory for the linear rheology of worm-like micelles accounts for the distribution of micelle lengths and their linear relaxation times, resulting from the combination of breakage, rejoining, and reptation of the micelles in their entanglement tubes. This linear model of Cates, especially when generalized to account for additional relaxation dynamics [2], provides a semi-quantitative description of the linear rheology of entangled solutions of worm-like micelles, and so provides a sound basis for development of a model for nonlinear rheology. The major difficulty in the development of constitutive models for worm-like

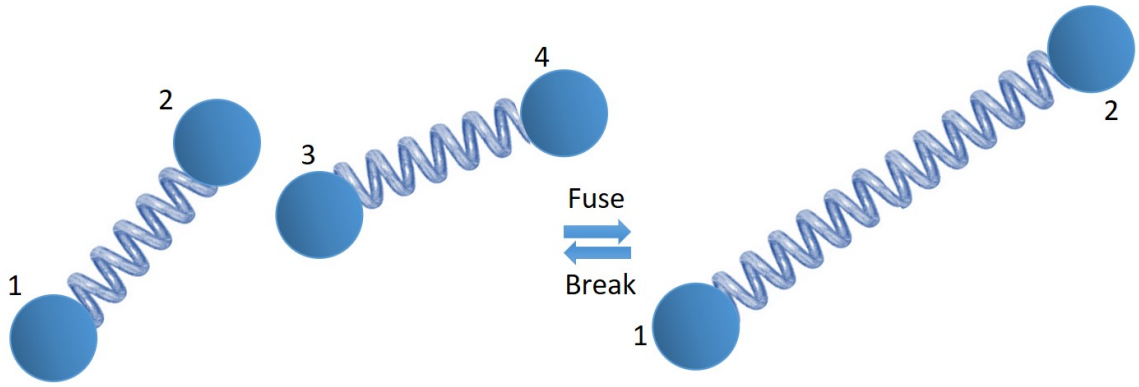

Figure 2.1: Reveersible scission of wormlike micelles in the VCM model. Two short dumbbells of length, L fuse to form a longer dumbbell of length, $2L$. The long dumbbell can also break in the middle to give two shorter dumbbells each of length, L.

micelles is in accounting simultaneously for their dynamic breakage and re-formation, and their nonlinear dynamics produced by flow. A few nonlinear constitutive models that account for both aspects of the dynamics are available, however. The nonlinear model by Cates and coworkers [3, 4] modifies the Doi-Edwards theory by including micelle breakage and rejoining, but suffers from the limitations of the Doi-Edwards theory in its neglect of chain stretching dynamics in fast flows. The "VCM" model of Vasquez, Cook, and McKinley, on the other hand, is derived from equations of ordinary dumbbell dynamics, modified to allow fusion of short dumbbells into long ones as depicted in Fig. 2.1. This two-species model, while ignoring entanglements, is able to allow for fully nonlinear stretching dynamics of micelles, and includes a phenomenological description of shear-induced breakage. It also could be readily extended to a multi-species model, which would allow for a range of micelle lengths, rather than just the short and long species of the original VCM model. This opens up the intriguing possibility of linking the nonlinear VCM constitutive equation to the rather well-developed theories for the linear rheology of wormlike micelles, which originated from the work of Cates in 1987 discussed above.

To realize this vision, the VCM model would need to be extended beyond its current (but easily alleviated) restriction to two micelle species. While this gener-

alization would be not be difficult conceptually, and in fact the extension to three species has already been carried out by Germann et al. [5], it would necessitate the use of considerably greater computational resources, especially if many, rather than a few, micelle species, are to be tracked. A more serious conceptual difficulty is the need to include entanglement interactions among micelles, which would be required in any physically realistic model of worm-like micelles at concentrations beyond the very dilute. A final issue is in the validation and improvement of the VCM model itself, even in its two-species version. As we discuss below, the VCM model, while originally derived from a kinetic theory in phase space, contains some ad hoc steps and errors in its derivation. The theory has been re-derived on a thermodynamically sound basis by Germann et al. [5] using the Poisson bracket formalism, yielding similar equations as those of the original VCM model, but the bracket formulation involves ensemble averaged quantities, not necessarily rigorously related to averages over the dynamics of individual micelles.

Therefore, in this work, we carry out Brownian dynamics (BD) simulations of the original physical model underlying the VCM model, that is, we simulate Hookean dumbbells that can can fuse into two-spring chains, and break again into individual dumbbells, while subjected to flow. We show that the rheological properties predicted by these BD simulations in shear flow disagree with the predictions of the VCM model for the same set of input parameters. We find that the key problem in the VCM model is its loss of information regarding the conformation of individual dumbbells when they fuse into a longer dumbbell or when this longer dumbbell is broken down again into the shorter dumbbells. We show how the VCM model can be re-derived more rigorously, by retaining conformations of the individual shorter species as they are combined into the longer species. This allows the predictions of the revised "VCM-R" model to match those of the BD simulations. The work therefore sets the stage for physically more detailed extensions of the VCM model, hopefully advancing towards

the goal of a quantitative theory. The paper is arranged as follows: in Section 2.2, we develop a Brownian dynamics simulation method to test the predictions of the VCM model. We compare the predictions of the BD simulations to the VCM model and discuss the results in Section 2.3.1. We then proceed to offer a revision of the VCM in Section 2.4 that give results consistent with the predictions of an analogous BD simulation.

2.2 Formulation of the two-species Brownian Dynamics simulation

We first consider the dynamics of a chain of N beads connected by N-1 massless springs. In the absence of excluded volume and hydrodynamic interaction, the equation of motion for each bead, i, in the bead-spring chain is given by Langevin equation [6]

$$\frac{d\mathbf{r}_i}{dt} = \boldsymbol{\kappa} \cdot \mathbf{r}_i + \frac{1}{\zeta}\mathbf{F}_i^{sp} + \left(\frac{6k_BT}{dt\zeta}\right)^{1/2} \mathbf{n}_i \tag{2.1}$$

where $\mathbf{r}_i$ is the position vector of bead, i, ζ is the bead drag coefficient per bead, $\boldsymbol{\kappa}$ is the transpose of the velocity gradient tensor, i.e., $\boldsymbol{\kappa} = (\boldsymbol{\nabla}\mathbf{v})^T$, and $\mathbf{F}_i^{sp}$ is the force-extension relation for the springs in the chains. The last term in Eq. (2.1) is the Brownian force which represents the rate of thermal bombardment of the micelles by the solvent. $\mathbf{n}$ is a three-dimensional vector with each component generated from random numbers that are uniformly distributed between -1 and 1 and with zero mean. k_B and T represent the Boltzmann constant and temperature respectively. The springs in the bead-spring chains are considered to be Hookean, similar to the VCM model. Therefore,

$$\mathbf{F}_i^{sp} = H\mathbf{Q}_i \tag{2.2}$$

where $\mathbf{Q}_i = \mathbf{r}_{i+1} - \mathbf{r}_i$ is the connecting vector between consecutive beads (or spring vector) and the linear spring constant, H is given by

$$H = 2k_BT\beta_s^2; \quad with \quad \beta_s^2 = \frac{3}{2N_{K,s}b_K^2} \tag{2.3}$$

where β_s^2 controls the elasticity of the spring and $N_{K,s}$ is the number of Kuhn segments, of length, b_K in a spring. To represent the VCM model, consider two ensembles of micelles: long and short, that exchange species during breaking and rejoining events. As in the VCM model, a micelle of the long species, twice the size of those of the short species, breaks to give two of the short species; that is $A \rightleftarrows 2B$, where A and B denotes long and short species respectively (see Fig. 2.1). We therefore represent the evolution of the number density of long (n_A) and short (n_B) species by Eq. (2.4) assuming homogeneous, unidirectional flows and no spatial variation.

$$\frac{dn_A}{dt} = \frac{c_B}{2}n_B^2 - c_An_A \tag{2.4a}$$

$$\frac{dn_B}{dt} = -c_Bn_B^2 + 2c_An_A \tag{2.4b}$$

where N_{A0} is the dimensional number density of long species chains at equilibrium. $c_A = c_{Aeq}\lambda_{1A}$ and $c_B = c_{Beq}\lambda_{1A}N_{A0}$ are the rates for breaking and rejoining of long and short chains respectively. The above equations are identical to the corresponding equations of the VCM model.

Given the dimensional number density of long species of micelles in equilibrium are represented by N_{A0}, the number of chains that will break in a given time step Δt is given as $c_An_AN_{A0}\Delta t$ while the number of recombination events is given by $0.5c_Bn_B^2N_{A0}\Delta t$. The number of springs in a long-species chain is chosen such that in a scission event, a long-species chain (which is selected at random) is broken in the middle resulting in two short-species chains with equal number of springs in each of them. One of the newly formed short chains takes the configuration of the first to

middle bead of the long-species chain that broke while the other short chain assumes the configuration of the middle bead to the last. When a fusion event is to occur, two short-species chains are each selected at random, and either of the end beads of each co-fusing chain are merged into a single bead with equal probabilities. The newly formed chain maintains the relative bead positions of each of the two fusing chains; and the spring vectors of the co-fusing short-species chains are used to propagate the new bead positions across the entire fused chain. This ensures that the relative extensions and internal configurations of each fusing chain are maintained in the resulting long-species chain. 500 chains are each contained in the ensemble of long and short species at the beginning of the simulations. The time step used for the simulations was 10^{-3} in dimensionless time units.

2.3 Results and Discussion

2.3.1 Comparison of VCM model predictions to Brownian Dynamics (BD) results

The VCM model accounts for both long and short species wormlike micelles as dumbbells in which two short dumbbells can fuse into one long one. We note that Cates [7] has also presented a model for two (polymeric) species that can fuse end-to-end. Therefore, each short-species chain is chosen to have one spring and two beads (a dumbbell) in our two-species Brownian dynamics (BD) simulation. We can implement the fusion such that the orientation of the newly formed long dumbbell is in the direction of the resultant vector of the connecting spring vectors of the fusing short dumbbells. We represent this schematically in Fig. 2.2. The length of the long dumbbell is taken as the sum of the lengths of the connecting spring vectors of the fusing short dumbbells. However, the breakage of the long dumbbell into two shorter ones is not so easily handled. The simplest approach is to break the long chain in

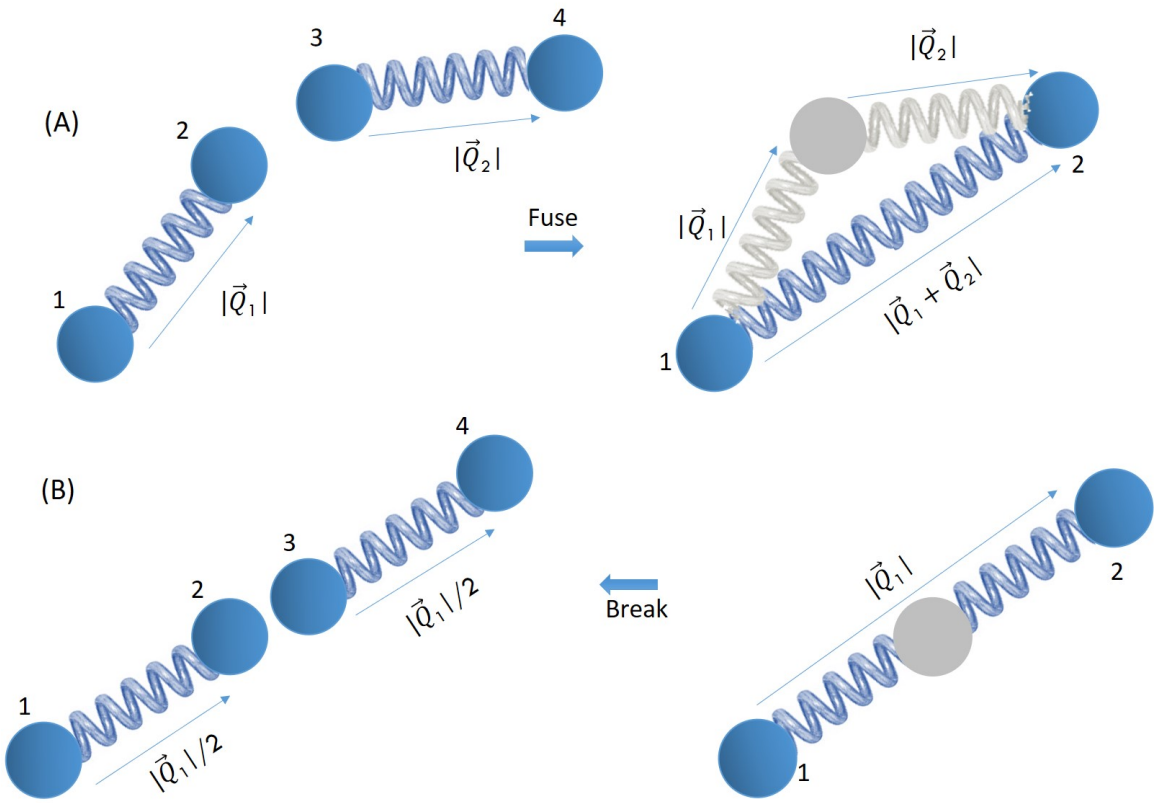

Figure 2.2: Implementation of VCM-type reversible scission in BD simulations where (A) two short dumbbells fuse end-to-end, and the formed long chain has an end-to-end vector equal to the sum of the connecting vectors of the fusing short dumbbells and (B) a long dumbbell breaks in the middle along its contour such that the newly formed short dumbbells have lengths equal to half that of the original long species and each inherits the orientation of the long dumbbell. The gray bead and springs in (A) represent the part of the fusing dumbbells that morphs into the long species. The gray bead in (B) denotes the point along the contour of the long dumbbell where the scission occurs leading to the formation of two short species dumbbells.

the middle to give two shorter dumbbells each with length equal to half that of the broken long dumbbell. However, this approach is not microscopically reversible and so will not be consistent with equilibrium thermodynamics, as we illustrate next. This thermodynamic problem can be remedied readily by tracking an internal variable in the long dumbbell, as shown shortly.

2.3.1.1 VCM comparison to BD simulations under equilibrium conditions

Dumbbells of varying initial conformations were allowed to equilibrate using the aforementioned reversible scission scheme represented in Fig. 2.2. At equilibrium, $\boldsymbol{\kappa} = \mathbf{0}$, therefore, the ensemble average stress tensor is given as [8]

$$\langle \mathbf{F}^{sp}\mathbf{Q} \rangle_{\alpha eq} = N_{\alpha 0} k_B T \boldsymbol{\delta} \tag{2.5}$$

where $\alpha = A, B$. The stress can be normalized by the modulus $G = N_{\alpha 0} k_B T$ which gives a normalized stress of $\boldsymbol{\delta}$ at equilibrium. Therefore the isotropic stress components which are the diagonal terms of are unity while other non-diagonal terms are zero. We observed that the normalized isotropic stresses for both micelle species were not equal to unity during reversible scission when there is no flow as shown in Fig. 2.3. However, the normalized isotropic stress fluctuated about unity for both micelle species when reversible scission was prevented by setting the scission rate is set to zero. This shows that the breaking dumbbells in the middle to give equal-length shorter dumbbells and fusing short dumbbells into longer dumbbells by adding the end-to-end vectors of the short micelles violates thermodynamic equilibrium as we surmised above.

We can repair the thermodynamic problem while preserving the dumbbell description of both the long and short chains by noting that a chain with 3 beads and 2 springs has the same (longest Rouse) relaxation time as a dumbbell with the same number of Kuhn segments as the two-spring chain. We therefore incorporate an internal bead within the long "dumbbell," making it a chain with 3 beads and 2 springs. However, to retain similarity to the VCM model, for which the long chain is a dumbbell, in our BD simulations the end-to-end vector of the long species is used in computing the stress contributed by the long chain, rather than taking the stress to be the sum of the contributions from the two springs making up the long chain. Thus,

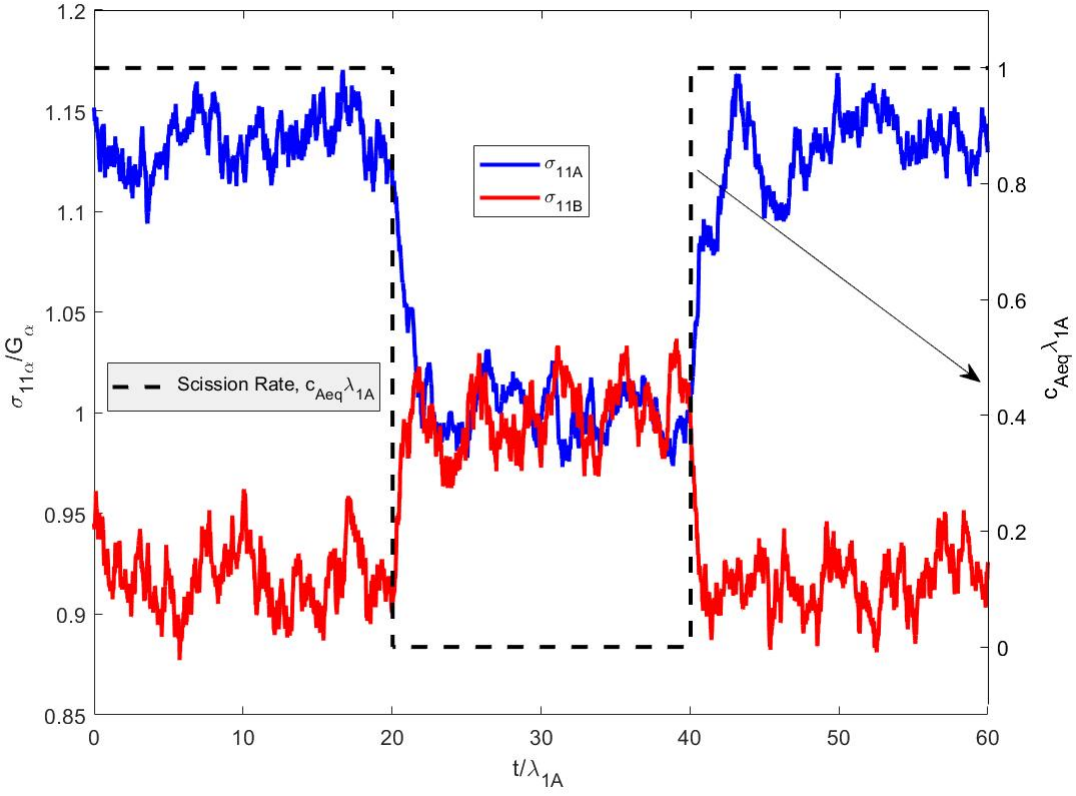

Figure 2.3: Evolution of normalized isotropic stress component for equal numbers of long (denoted by A) and short (B) dumbbells equilibrating without shear flow and with and without reversible scission. The reversible scission is implemented using the scheme described in Fig. 2.2. The dashed line indicates the rate of scission given along the right axis while the stress normalized by the modulus ($G_\alpha = N_{\alpha 0}kT$) of each species is recorded on the left axis. Between 0 and 20 Rouse times, a scission rate, $c_{Aeq}\lambda_{1A} = 1$ is allowed, where λ_{1A} is the longest relaxation time of the long species micelles and c_{Aeq} is the rate of scission of the long micelles at equilibrium. Between 20 and 40 Rouse times, the reversible scission is turned off by setting $c_{Aeq}\lambda_{1A} = 0$ and reversible scission is reinstated after 40 Rouse times.

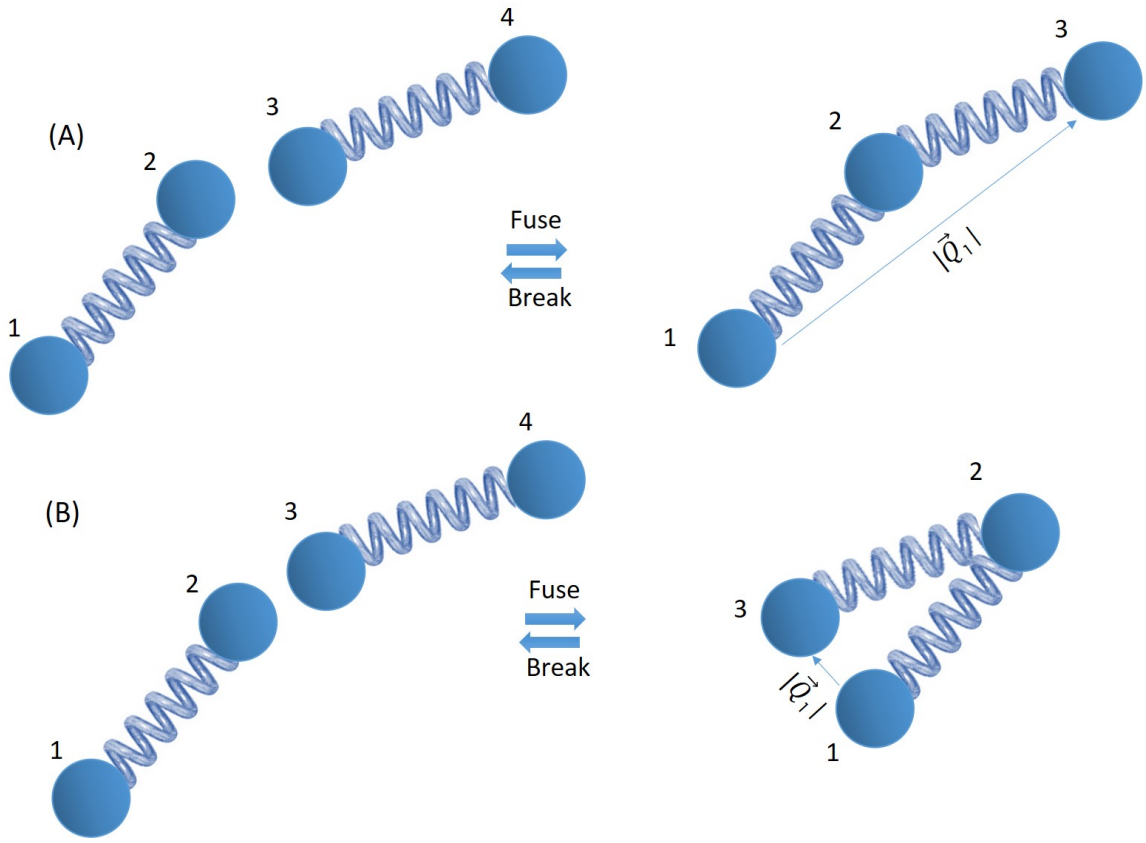

Figure 2.4: Fusion of two short dumbbells into a two-spring chain. The position of the middle bead is always tracked in the simulation and therefore the chain is broken at that bead position when scission occurs. The stress of the long dumbbell is calculated using the two end-to-end vectors of the two-spring chain (details in text). Fusion can occur in (A) with springs aligned end-to-end roughly parallel, with bead 2 fusing with bead 3 or (B) roughly anti-parallel in folded fashion with bead 2 fusing with bead 4. We take these two cases to occur with equal probability.

for the long chain, the internal bead is ignored in computing the stress, and is only used as a marker to determine the lengths and orientations of the short dumbbells formed upon breakage of the long chain.

The reversible scission mechanism is shown in Fig. 2.4. When fusion of two short dumbbells occurs, we fuse them with equal probability in the approximately parallel and anti-parallel configurations. Thus, the stress contributions from the long chains, $\boldsymbol{\sigma}_A$ and short chains, $\boldsymbol{\sigma}_B$ are computed as

$$\boldsymbol{\sigma}_A = n_A H_A \left\langle (\mathbf{r_3} - \mathbf{r_1})(\mathbf{r_3} - \mathbf{r_1}) \right\rangle_A \tag{2.6a}$$

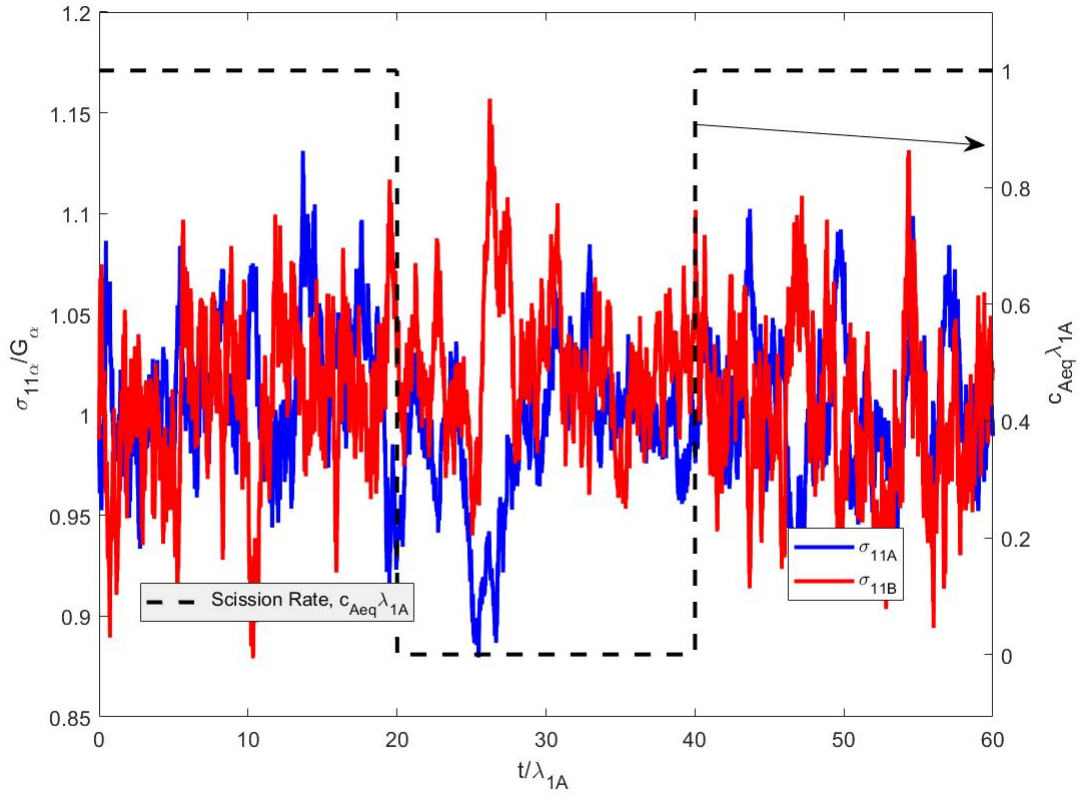

Figure 2.5: Similar to Fig. 2.3 but with reversible scission mechanism described in Fig. 2.4.

$$\boldsymbol{\sigma}_B = n_B H_B \left\langle (\mathbf{r_2} - \mathbf{r_1})(\mathbf{r_2} - \mathbf{r_1}) \right\rangle_B \tag{2.6b}$$

where each vector, $\mathbf{r}_i$ is the bead position in a chain drawn from the ensemble of A chains in Eq. (2.6a), and from the ensemble of B chains in Eq. (2.6b). With these definitions, our BD model has the same relaxation times and formulas for stress contributions as in the VCM model for both the long and short chains. Using the same breakage and fusion rates, the only difference between our model and the VCM model is then in the flow-induced conformations of long and short chains. Using the reversible scission mechanism described above (see Fig. 2.4), we find in Fig. 2.5 that the normalized isotropic stresses for the long and short micelles fluctuate about unity during reversible scission thereby satisfying thermodynamic equilibrium.

2.3.1.2 VCM comparison to BD simulations under flow conditions

Based on the findings in Section 2.3.1.1, we therefore compare the VCM model predictions to the BD simulations using the end-to-end stresses of the 2-spring chains for the stresses of the long dumbbells as described earlier (see Fig. 2.4). When $c_A, c_B = 0$, that is, there is no reversible scission, for a Weissenberg number, $Wi = \dot{\gamma}\lambda_{eff} = 1$ where λ_{eff} is the effective relaxation time of the system [9], defined by Eq. (2.7), both the VCM model and Brownian dynamics simulations give the same results as shown in Fig. 2.6. Here,

$$\lambda_{eff} = \frac{\lambda_{1A}}{1 + \lambda_{1A} c_{Aeq}} \tag{2.7}$$

where λ_{1A} is the longest relaxation time of the long micelles and c_{Aeq} is the rate of scission of the long micelles at equilibrium. In this work, we take the rate of scission $c_A = c_{Aeq}$ to be a constant, independent of the micelle configuration, although a dependence on configuration or stress could readily be included, as is done in the VCM model. The agreement of the methods is expected because without reversible scission, the VCM model becomes two sets of non-interacting Upper-Convected Maxwell (UCM) models. The two-species BD simulation also gives two non-interacting ensembles of micelles whose averaged stress responses fluctuate slightly about the UCM model predictions due to the finite size of the ensemble.

Figure 2.7 shows discrepancies in the predictions of the BD simulation and the VCM model when reversible scission occurs. In the results depicted in the figure, there are equal numbers of long and short species at equilibrium, the dimensionless rate of scission of long species is taken as $c_{Aeq}\lambda_{A1} = 1$ and the shear rate corresponds to a Weissenberg number of unity. The discrepancy in the predictions is mainly due to the relatively higher stresses for the short micelle species in the VCM model compared to that of the BD simulations. The higher stress arises in the VCM model because the short micelles resulting from the scission of a long micelle are taken to have the same

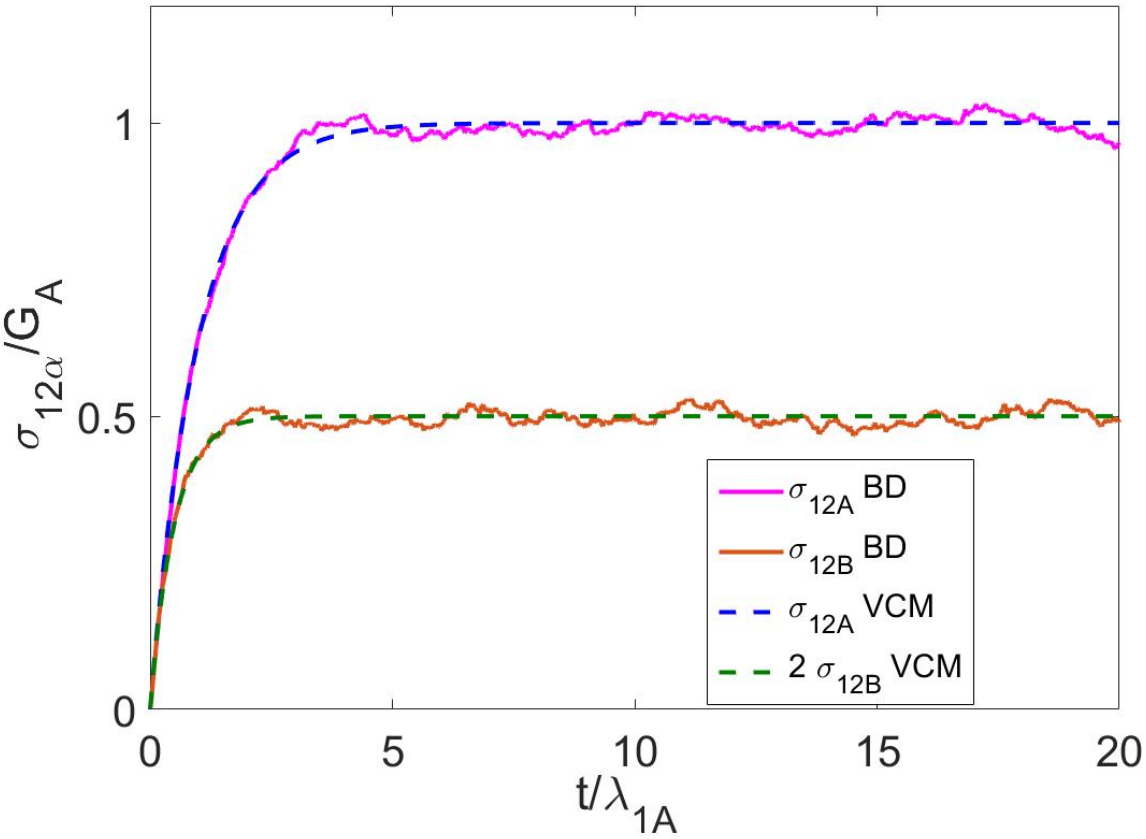

Figure 2.6: Comparison of stress contributions from equal numbers of long (A) and short (B) chains (i.e. $n_B^0 = 1$) for Brownian Dynamics simulation and for the Vasquez-Cook-McKinley (VCM) model [9] without reversible scission at Weissenberg number of unity. The ratio of relaxation times of short to long chains is taken to be $\epsilon = 0.5$ in both the simulations and the VCM model.

conformation tensor as the long micelles from which they arose. Similarly, when short chains fuse, in the VCM model, the fused short chains contribute their conformation tensor to that of the long chains created from them, without accounting for the change in conformation resulting from the end-to-end joining of the short chains. The BD simulations track the conformations of the individual springs in the long chain, which then influences the configuration distribution of the short chains that result from long-chain scission. Similarly, the conformations of short chains are retained when those chains are merged into long chains, since the long chain is represented in the BD model by two explicit short chains, rather than by a dumbbell, as is the case in the VCM model.

We also note here that while the VCM equations are nominally derived from a phase space kinetic theory, the derivation is not rigorous. In particular, in each of Eqs. 1a and 1b of Vasquez et al. [9], a term appears involving the product of two micelle distribution functions. This nonlinear term cannot be integrated out with a single conformation integral and would require two three dimensional integrals, one over the conformation space of each configuration function. In fact, Eqs. 1a and 1b in Vasquez et al. [9] are dimensionally incompatible with Eqs. 4a and 4b, since each configuration function has units of inverse real volume and inverse configurational volume. The coefficient c'_B of the product of two distribution functions must therefore have units of configuration volume needed to make the equation dimensionally balanced, but these units are incompatible with the units required for the corresponding coefficient c'_B in Eqs. 4a and 4b. The basic problem is that the effect of scission and fusion on the configuration distribution functions of the species is not addressed at a detailed level in the VCM model. Thus the final equations, which are dimensionally self-consistent despite the dimensional inconsistencies in the steps of its derivation, should be regarded as phenomenological, rather than resting on a clear physical theory. This lack of a rigorous derivation from phase space means that the model predictions

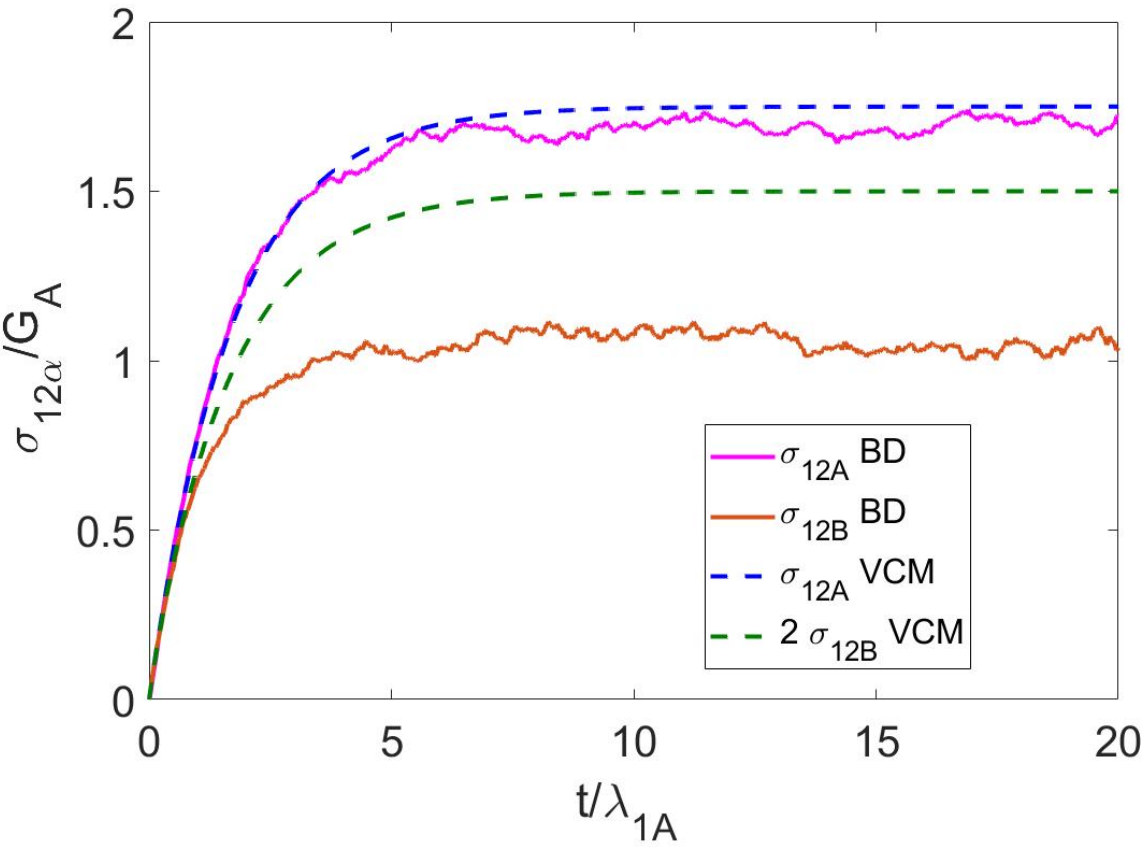

Figure 2.7: The same as Fig. 2.6, except with reversible scission present (dimensionless equilibrium breakage rate, $c_{Aeq}\lambda_A = 1$).

cannot be related to the dynamics of the individual micelle species in any precise way.

2.4 Formulation of VCM-R, the revised two-species reversible scission model

To rectify the discrepancies in the predictions of the VCM model and the BD simulations, we now present a two-species reversible scission model, the "VCM-R" model, based on the multi bead-spring model of Wiest et al. [10] and the reaction dynamics of the VCM model [9]. In the revised model, depicted in Fig. 2.8, the wormlike micelles are represented by a series of beads and springs which can break at the middle along the contour of the chain to give two shorter micelles. The short

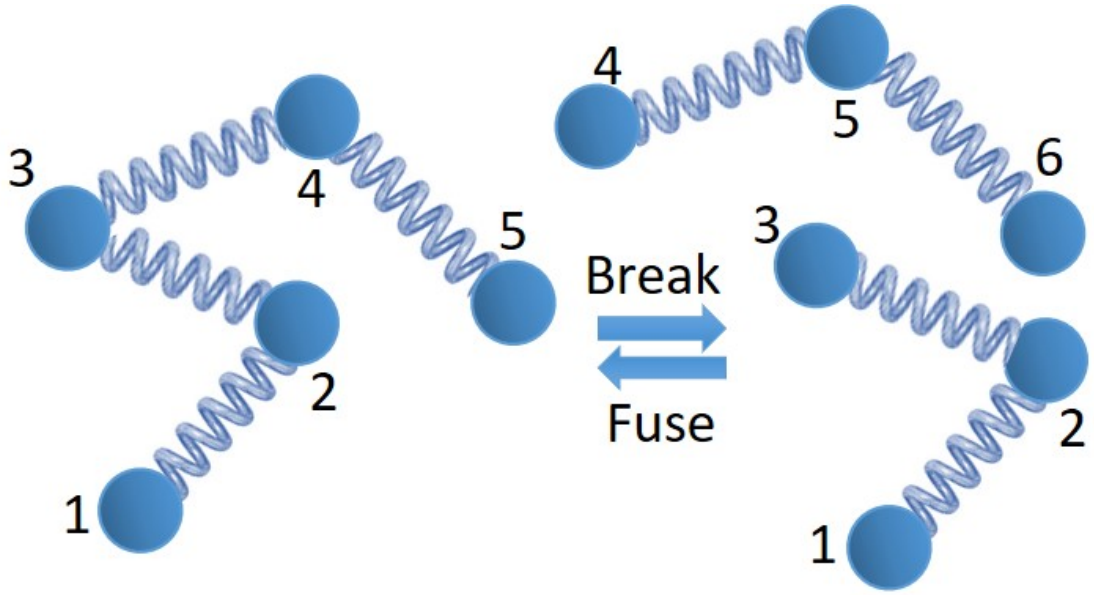

Figure 2.8: Scission of micelle represented with $(N-1)$ springs at the middle to form two shorter micelles each with $(N-1)/2$ springs. The fusion of the two short micelles can occur between any of their end beads to form a long micelle with springs aligned in a roughly parallel or anti-parallel folded configuration similar to Fig. 2.4a and Fig. 2.4b respectively. The relative orientations of the short micelles are retained in the long micelle. In the particular case shown in this figure, $N = 5$, therefore, the long micelle is a four-spring chain while the short micelles are two-spring chains.

micelles can also fuse to give long ones. We develop the model for chains with arbitrary numbers of springs, but will later apply it to the case where the long chains have only two spring, and the short chains have only one. For simplicity, we restrict ourselves, however, to the case where breakage always occurs only at the mid-point of the long chains, so that there are only two species, although this could obviously be generalized. This gives a more realistic model compared to the VCM model where both long and short species are considered dumbbells. This also allows for a direct comparison of the stress to that of the BD simulations without losing the configurations of the micelle species during reversible scission.

The evolution equation for the configurational distribution function, ψ of the

micelles is given by Eq. (2.8) [8]

$$\frac{\partial \psi_\alpha}{\partial t} = -\sum_{j\alpha} \frac{\partial}{\partial \mathbf{Q}_{j\alpha}} \cdot \left\{ \boldsymbol{\kappa} \cdot \boldsymbol{Q}_{j\alpha} \psi_\alpha - \frac{1}{\zeta} \sum_{k\alpha} A_{jk} \times \left[k_B T \frac{\partial \psi_\alpha}{\partial \mathbf{Q}_{k\alpha}} + H f_{k\alpha} \mathbf{Q}_{k\alpha} \psi_\alpha \right] \right\} \quad (2.8)$$

where $\alpha = A, B$ denoting the long and short species respectively and the matrix A is the Rouse matrix describing the connections of the springs. The summations over j and over k are over all spring vectors in the chain, which is the number of beads minus 1. Integrating Eq. (2.8) over the configuration space, $d\mathbf{Q}_{j\alpha}$ gives the evolution equations for the number densities of the long and short species, which is Eq. (2.4), valid under the assumption of homogeneous flow. Calculating the second moments of the configurational distribution function, ψ by multiplying Eq. (2.8) by the dyad $\mathbf{Q}_i \mathbf{Q}_j$ and integrating over all $\mathbf{Q}^{N-1}$ degrees of freedom gives Eq. (2.9) after adding the rate of formation and loss of the respective $< \mathbf{Q}_i \mathbf{Q}_j >$ for long and short species micelles due to scission and fusion of micelles.

$$\begin{aligned} \frac{d}{dt}(n_A < \mathbf{Q}_i \mathbf{Q}_j >_A) = \boldsymbol{\kappa} \cdot n_A < \mathbf{Q}_i \mathbf{Q}_j >_A + n_A < \mathbf{Q}_i \mathbf{Q}_j >_A \cdot \boldsymbol{\kappa}^T + (2k_B T/\zeta_A) n_A A_{ij} \boldsymbol{\delta} \\ - (H/\zeta_A) \sum_{k}^{N-1} f_{kA} [A_{ik} n_A < \mathbf{Q}_k \mathbf{Q}_j >_A + A_{jk} n_A < \mathbf{Q}_i \mathbf{Q}_k >_A] \\ + \frac{c_B}{2} n_B^2 < \mathbf{Q}_i \mathbf{Q}_j >_B - c_A n_A < \mathbf{Q}_i \mathbf{Q}_j >_A \quad (2.9a) \end{aligned}$$

$$\begin{aligned} \frac{d}{dt}(n_B < \mathbf{Q}_i \mathbf{Q}_j >_B) = \boldsymbol{\kappa} \cdot n_B < \mathbf{Q}_i \mathbf{Q}_j >_B + n_B < \mathbf{Q}_i \mathbf{Q}_j >_A \cdot \boldsymbol{\kappa}^T + (2k_B T/\zeta_B) n_B A_{ij} \boldsymbol{\delta} \\ - (H/\zeta_B) \sum_{k}^{N_B - 1} f_{kB} [A_{ik} n_A < \mathbf{Q}_k \mathbf{Q}_j >_A + A_{jk} n_A < \mathbf{Q}_i \mathbf{Q}_k >_A] \\ - c_B n_B^2 < \mathbf{Q}_i \mathbf{Q}_j >_B + 2 c_A n_A < \mathbf{Q}_i \mathbf{Q}_j >_A \quad (2.9b) \end{aligned}$$

where $\boldsymbol{\delta}$ is the second order unit tensor, N and $N_B = (N+1)/2$ are the number of beads in the long and short chains respectively, and $f_{k\alpha}$ represents the force-extension

relationship for the spring. For Finite Extensible Nonlinear Elastic (FENE) springs with the Peterlin approximation, it is given as

$$f_{k\alpha} = [1 - (< Q_{k\alpha}^2 > / Q_0^2)]^{-1} \tag{2.10}$$

For Hookean springs, the maximum extension of the spring, Q_0 is infinite, and therefore, $f_{k\alpha} = 1$. The initial conditions for the revised model are

$$< \mathbf{Q}_i \mathbf{Q}_j >_\alpha = n_\alpha^0 \frac{Q_0^2}{b+3} \delta_{ij} \boldsymbol{\delta} \quad at \quad t = -\infty \tag{2.11}$$

where $b = HQ_0^2/k_BT$ is a dimensionless finite extensibility parameter, H is defined by Eq. (2.3) and n_α^0 represents the equilibrium number density of species, α. Note that Eqs. (2.9a) and (2.9b) include evolution equations for all dyads $< \mathbf{Q}_i \mathbf{Q}_j >$ including dyads for which $i \neq j$. Thus, the above equations include the evolution of cross correlations in orientations of different springs in a multi-spring chain. Inclusion of these cross terms strongly differentiates this model from the VCM model in which the long chain is represented by a dumbbell, which is incapable of tracking such cross-correlations, and their influence on the response of the chain to flow.

Note also that the last two terms in both Eqs. (2.9a) and (2.9b) are creation and destruction terms arising from scission and fusion of micelles. For the creation term in the long micelle (second to last term in Eq. (2.9a)), cross terms involving springs from two different short micelles are here set to zero, implying that the two short micelles can fuse either "head-to-head" or "head-to-tail" with equal probability, which cancels out any contribution to this cross-correlation from fusion of the short micelles. This implies that two B chains that are roughly parallel to each other are just as likely to fuse into a "back-folded" or nearly anti-parallel configuration as they are to fuse into a relatively straight or nearly parallel configuration. If a bias towards fusion into straight configurations is desired, then any equation for a spring-spring

cross-term $< \mathbf{Q}_i \mathbf{Q}_j >$ with $i \neq j$ for species A would need to contain contributions from fusion of species B. An expression for this contribution would then need to be developed based on the distribution or configurations of species B and the probability of fusion into a "straight" configuration. We avoid this difficulty here by assuming that the rate of fusion (or of scission) is not influenced by the orientations of the springs involved.

Thus, we set the term $< \mathbf{Q}_i \mathbf{Q}_j >_B$ in Eq. (2.9a) to zero if i and j are not either both less than N_B or both greater than or equal to N_B. Also, if they are both greater than or equal to N_B, we simply subtract $N_B - 1$ from each subscript, since the B chain is described by spring subscripts less than N_B. We note the head-tail symmetry of both the long and short chains reduces significantly the number of tensors that need to be tracked. Equations (2.9a) and (2.9b) are integrated in time as a set of coupled nonlinear ordinary differential equations using the fourth-order Runge-Kutta method. The stress contributions from the long and short species are calculated as

$$\boldsymbol{\sigma}_A = n_A \sum_{k=1}^{N-1} H f_{kA} < \mathbf{Q}_k \mathbf{Q}_k >_A \tag{2.12a}$$

$$\boldsymbol{\sigma}_B = n_B \sum_{k=1}^{N_B-1} H f_{kB} < \mathbf{Q}_k \mathbf{Q}_k >_B \tag{2.12b}$$

We also note that the above formulation is readily extended to multi-spring chains that can break at any bead along their contour, creating species that range from one-spring chains up to some assigned maximum number $N - 1$. However, the number of equations to be solved grows rapidly, since for each species, the self-correlations and cross-correlations of all spring vectors need to be tracked. Symmetry reduces the number of equations by a numerical pre-factor, but the number of equations scales roughly as N^3. One limit where breakage occurs so that only chains containing $1, 2, 4, 8$, etc. springs are allowed and these only break in the middle, but the number of equations still increases as N^3 because of the cross-correlations. The cross-correlations

are avoided in normal bead-spring chains by using normal modes, but when breakage and rejoining are considered, it does not seem obvious how to carry out such an analysis. Thus, for large numbers of micelle species, it may actually be cheaper to carry out Brownian dynamics simulations, which though slow, have better scaling properties when the number of species becomes large.

Comparison of revised two-species VCM-R constitutive equation to analogous Brownian Dynamics simulation

In comparing the revised constitutive equation to the BD simulation, $N = 3$ and $N_B = 2$ were used, that is, the long species were represented with 3 beads and 2 springs which could break to give short species, which are dumbbells. We also take the springs to be Hookean. This case is chosen for simplicity to reduce computation time and because this case corresponds most closely with the VCM model. Theoretically, any value could be used for N. The stresses in the BD simulation are calculated as a sum of the stress contributions from individual segments of the chain and given by Eq. (2.13).

$$\boldsymbol{\sigma}_A = n_A \sum_{k=1}^{N-1} H \left\langle \mathbf{Q}_k \mathbf{Q}_k \right\rangle_A \tag{2.13a}$$

$$\boldsymbol{\sigma}_B = n_B \sum_{k=1}^{N_B-1} H \left\langle \mathbf{Q}_k \mathbf{Q}_k \right\rangle_B \tag{2.13b}$$

Note that we now compute the stress for the long chain as the sum of the contributions from each of the springs in that chain, rather than using the end-to-end vector of the whole molecule, as we did earlier, since our new VCM-R model explicitly tracks the configurations of each spring in the two-spring chain.

In the absence of reversible scission, the revised model gives the same predictions as the corresponding two-species Brownian Dynamics simulation (with stress from the long chain given by the contributions from each of the two springs) as shown in

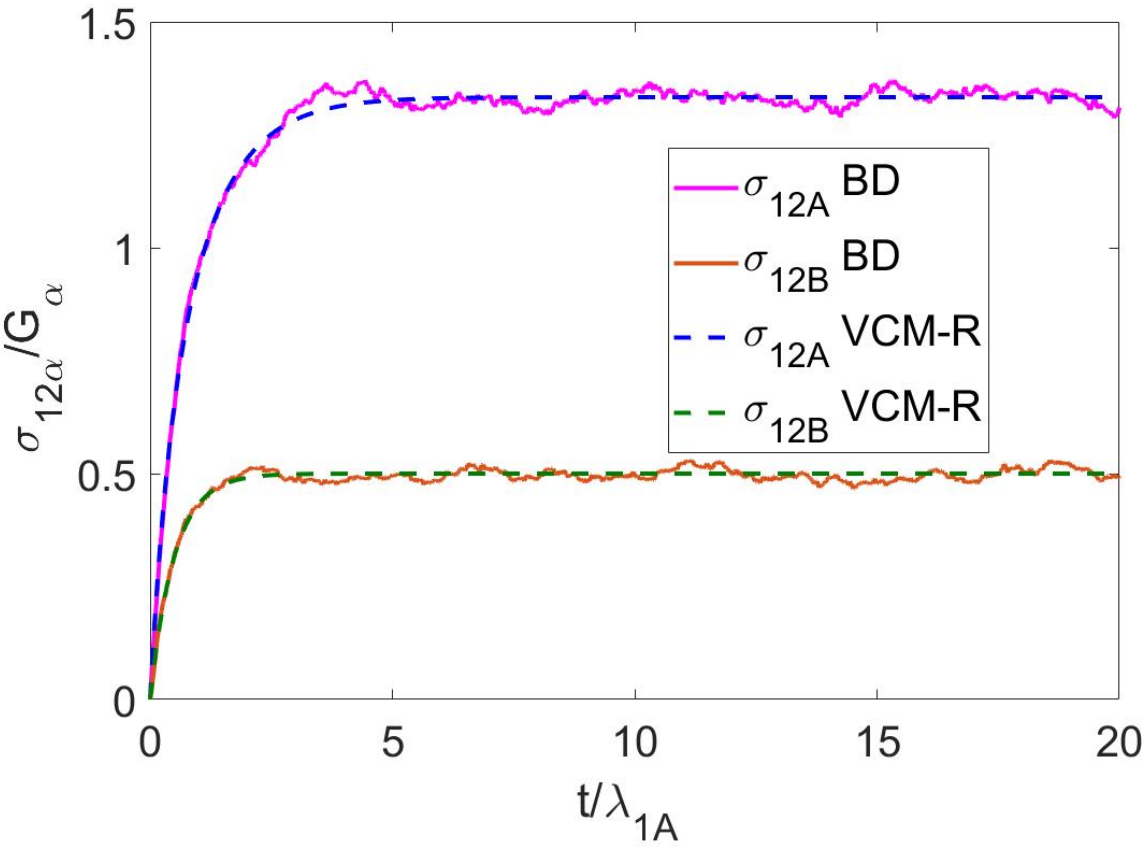

Figure 2.9: Comparison of stress contributions from long and short chains for Brownian Dynamics simulation and for the revised Vasquez-Cook-McKinley (VCM-R) model without reversible scission at a Weissenberg number of unity.

Fig. 2.9. This is because without reversible scission, the revised model becomes a set of decoupled equations for Rouse chains with multiple beads and springs. Similarly, the analogous BD simulations gives predictions that fluctuate about a mean value corresponding to the multi-bead-spring Rouse chain prediction. Figure 2.10 shows agreement between the VCM-R reversible scission model and the BD simulations in the stress response of the long and short micelles during shear with reversible scission characterized by a dimensionless breakage rate, $c_{Aeq}\lambda_{1A}$ of unity. The agreement is achieved because both the revised model and the simulation accurately account for the internal configurations of the long and short micelles.

In general, exchange of species during reversible scission leads to a relaxation of stress and a corresponding reduction in the ensemble-averaged steady stress of the

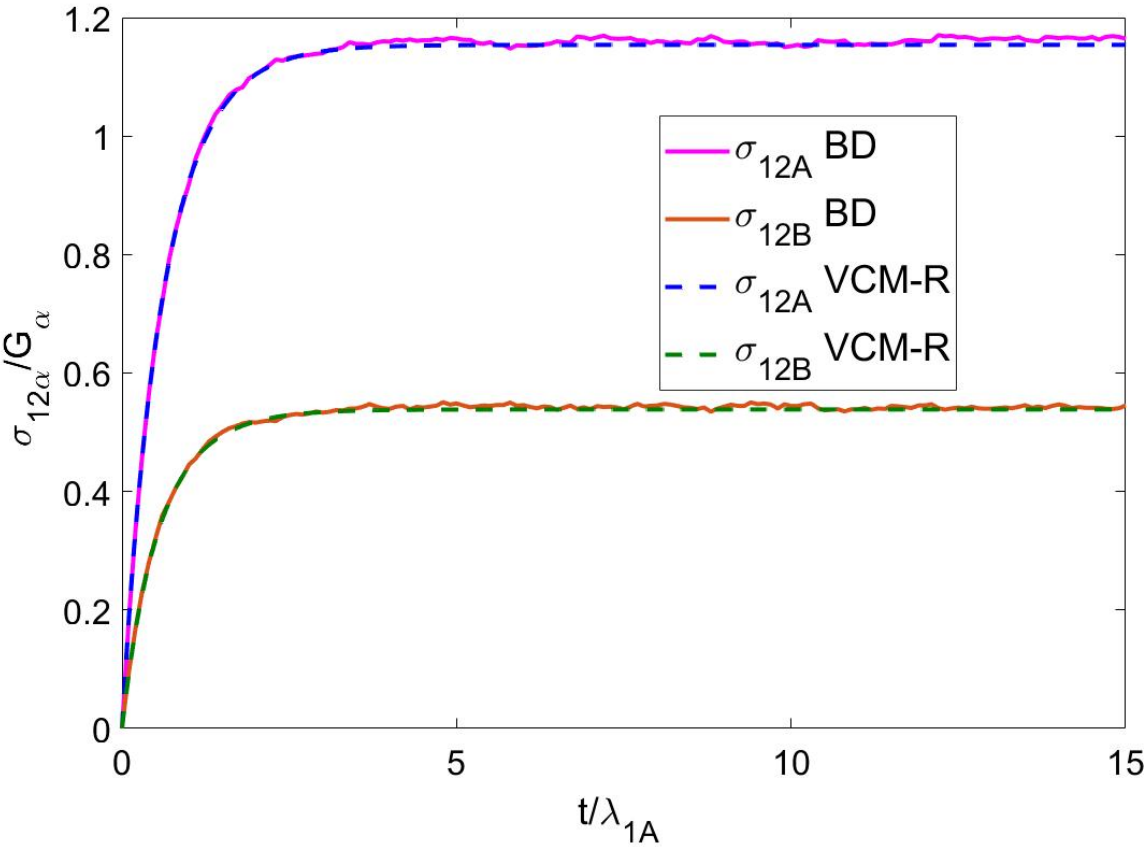

Figure 2.10: Similar to Fig. 2.9 but with dimensionless scission rate, $c_{Aeq}\lambda_{1A} = 1$

long micelles. The stretched chains resulting from the scission of long micelle species are more stretched than the short chains and so boost the instantaneous stress of the short chains before these chain segments relax at a quicker rate as a short micelle than they do when they are in the long micelle. Also, fusion events involving relatively relaxed short micelles reduce the ensemble-average stress of the long micelles.

2.5 Summary and Future Work

We have demonstrated that the implementation of reversible scission of micelles with both species represented as dumbbells, as in the VCM model, differs in its predictions from predictions of Brownian dynamics simulations of nominally the same physical model. This discrepancy occurs because the VCM dumbbell model lacks

the internal degrees of freedom needed to accurately describe reversible scission in wormlike micelles. To repair this, multiple bead-spring chains are needed even in the simplest two-species model to accurately describe the exchange of species during the scission and recombination events. We accomplished this by using differential equations for end-to-end vector dyads developed by Wiest et al. to develop a constitutive equation that tracks the internal configurations of the wormlike micelles during reversible scission. The constitutive equation can describe chains with Hookean springs exactly, as shown by comparison with Brownian dynamics simulations of the same two-species model, and could account approximately for non-linear chains, for example by using finitely extensible nonlinear elastic (FENE) chains with appropriate closure approximations. Future work should explore calculations with a FENE spring, and with models with more than two species. It should also be possible to include scission and fusion rates that depend on average stress and orientation of the micelles.

Bibliography

[1] M. E. Cates, Macromolecules **20**, 2289 (1987).

[2] W. Zou and R. G. Larson, Journal of Rheology **58**, 681 (2014).

[3] M. E. Cates, The Journal of Physical Chemistry **94**, 371 (1990).

[4] N. a. Spenley, M. E. Cates, and T. C. B. McLeish, Physical Review Letters **71**, 939 (1993).

[5] N. Germann, L. Cook, and A. Beris, Journal of Non-Newtonian Fluid Mechanics **196**, 51 (2013).

[6] R. G. Larson, Journal of Rheology **49**, 1 (2005).

[7] M. E. Cates, Macromolecules **21**, 256 (1988).

[8] R. B. Bird, F. C. Curtiss, C. R. Amstrong, and H. Ole, *Wiley-Interscience*, 2nd ed., Vol. 2 (John Wiley & Sons, New York, 1987) p. 464.

[9] P. a. Vasquez, L. P. Cook, G. H. Mckinley, and L. Pamela Cook, Journal of Non-Newtonian Fluid Mechanics **144**, 122 (2007).

[10] J. M. Wiest, L. E. Wedgewood, and R. B. Bird, The Journal of Chemical Physics **90**, 587 (1989).

CHAPTER III

Effect of Entanglements on the Rheology of Worm-like Micelles

3.1 Introduction

Wormlike micelles and polymers in the semi-dilute and concentrated regimes feel the topological constraints of neighboring chains as they diffuse. The topological constraints form a tube around the polymer thus leaving reptation [1] of the chain out of the tube as the primary means of stress relaxation [2]. At concentrations above the overlap concentration, C^*, entanglements form as the polymers are longer than the inter-polymer distance (see Section 1.2.3). The topological entanglements apply a potential on the monomers of the polymer network at all points along the contour of the chain thereby confining their fluctuations to the constricting tube [3]. In the theory of rubber elasticity, these entanglements were treated as slip-links which can slide along the contour of the polymer between crosslinks in a polymer network [4, 5].

The "slip-tube" model [6] was developed by Rubinstein and Panyukov [6] using ideas of earlier models: the Affine Network model [7, 8, 9], Phantom Network model [10, 11], Constrained-Junction model [12, 13], "Edwards Tube model" [3] and the Non-affine Tube model [14]. The Rubinstein and Panyukov [6] model accounts for the redistribution of length stored by network chains along their confining tube by

considering tube contour length fluctuations, first introduced in the analysis of Doi and Edwards [2]. In the slip-tube model, permanent crosslink junction points between network chains and virtual chains are substituted with slip-links that are attached on one end to the network chain and to virtual chains on the other [6]. The virtual chains act as the entanglements and impose a confinement potential on the network chain. The virtual chains are attached to an affinely deformed nonfluctuating elastic background. The slip-links are not allowed to cross one-another, therefore, the segments of network chain must pass through the slip-links in a fixed order. Thus, network chain segments locally free themselves of the constraints as they diffuse through the slip-links [6].

The slip-tube model was successful in giving predictions that matched experimental data of both PDMS (poly dimethyl siloxane) and natural rubbers. However, it does not include the disentanglement and re-entanglement at the chain ends. Likhtman [15] adapted this model to a melt of linear chains by adding these additional processes to the slip-tube model. They did this by allowing the slip-links to slide off the chain ends, therefore destroying them and regenerating new entanglements along the chain. The entanglements were thus represented by slip links tethered to anchor points by a spring of parabolic form in Likhtman's single-chain slip link model [15]. The single-chain slip-link model was able to predict linear rheological behavior for polymers.

In this work, we incorporate micelle reaction kinetics into the slip-link model [15] and report the effects of entanglements on wormlike micelles dynamics. In what follows, we present a Brownian dynamics (BD) simulation of a two-specie multi-chain slip-link model involving the reversible scission of micelles.

3.2 Formulation of the model

The BD simulations of wormlike micelle chains are carried out as described in Section 2.2 but, with additional constraints from entanglements represented by the slip-links. The system is depicted in Fig. 3.1. This following description of the slip link model including Eqs. (3.1), (3.2), (3.5) and (3.6), are taken, with little change, from the work of Likhtman [15]. Added to these equations are rules for accounting for breakage and rejoining of chains, and for tracking the locations of slip links during this process. The slip links travel in straight lines between monomers of the micelle chain. The location of the slip-link is tracked with a continuous variable, $x = 0..N$. The micelle chain monomers experience the entanglements as a mean field potential given as $U = 3k_BT/(2N_sb_k^2)(\mathbf{r}_i - \mathbf{a}_i)^2$ where $\mathbf{r}_i$ and $\mathbf{a}_i$ are the position vectors for the micelle bead and anchor point i respectively. N_s is the number of Kuhn segments in the virtual springs [15]. The potential energy of the micelle chain is therefore a sum of the contributions of potentials from the micelles and the virtual springs.

$$U_\alpha = \frac{3k_BT}{2N_{k,s}b_k^2}\sum_{i=0}^{N_\alpha-1}(\mathbf{r}_{i+1} - \mathbf{r}_i)^2 + \frac{3k_BT}{2N_sb_K^2}\sum_{j=1}^{Z_\alpha}(\mathbf{a}_j - \mathbf{s}_j(x_j, \{r\}))^2 \tag{3.1}$$

where

$$\mathbf{s}_j(x_j, \{r\}) = \mathbf{r}_{trunc(x_j)} + (x_j - trunc(x_j))(\mathbf{r}_{trunc(x_j)+1} - \mathbf{r}_{trunc(x_j)}) \tag{3.2}$$

is the position of the slip-link j on the micelle chain. $N_{k,s}$ is the number of Kuhn segments in a micelle spring, and $trunc(x)$ is the nearest integer less than or equal to x. $Z_\alpha = N_\alpha/N_e$ is the number of slip links per chain on micelle species, α. N_α and N_e are the number of beads in species α and N_e is the number of monomers (Kuhn segments) between entanglements (slip links).

The wormlike micelles break and recombine dynamically in solution. When scis-

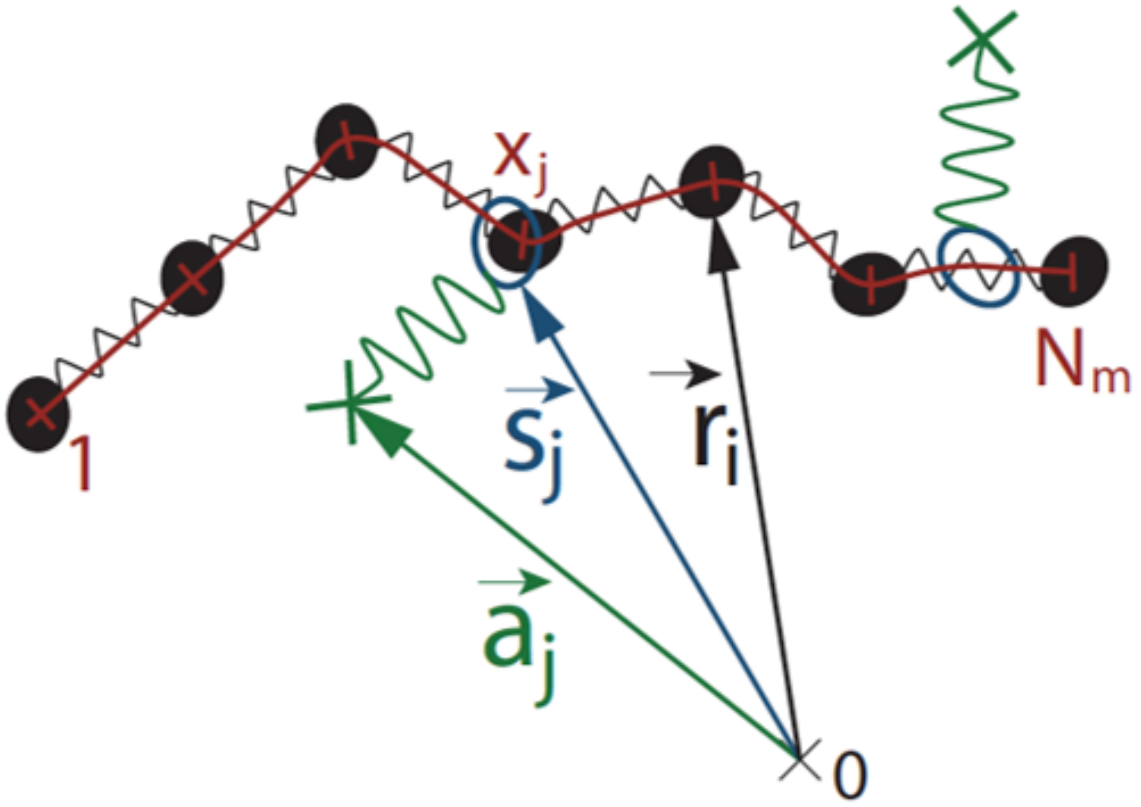

Figure 3.1: Schematic of entangled wormlike micelles. The wormlike micelle is represented by a chain of spherical beads (positioned at $\mathbf{r}_i$) and springs (bead numbered 1 to N_m). The entanglements, represented by green springs are connected to the wormlike micelle chain via slip-links, located at position x_j that slides along the micelle contour. The slip-link exerts an additional potential on the micelle chain at $\mathbf{S}_j$ and each slip link is attached to the affinely deformed elastic background at an by anchor point, $\mathbf{a}_i$ represented by a cross. Reprinted from [16], with the permission of AIP Publishing.

sion occurs, the long micelle breaks at the middle of the chain; thus, the newly formed shorter (daughter) micelles retain their topological entanglements after scission. As a result, the micelle is freed of entanglements beyond the point of scission along the micelle contour. Therefore,

$$Z_{B1} = Z_A - Z_{A|x_j > x_{N_B}}; \quad Z_{B2} = Z_A - Z_{A|x_j < x_{N_B}}; \quad 0 \leq x_j \leq N_A \tag{3.3}$$

where Z_{B1} and Z_{B2} represent the number of slip-links per daughter micelles 1 (spanning beads 1 to $N_B = trunc(N_A/2)$) and 2 (from beads $N_B + 1$ to N_A) resulting from the scission of micelle species, A. Similarly, during fusion, the newly formed micelle contains a sum of the slip-links present in each other fusing micelle chains, $Z_A = Z_{B1} + Z_{B2}$. The slip link and anchor positions, $\mathbf{s}_j$ and $\mathbf{a}_j$ are maintained relative to their positions and orientations in the breaking/recombining micelle(s). As in Chapter II, $A \rightleftarrows 2B$, where A and B denotes long and short species respectively. The evolution of the number density of long (n_A) and short (n_B) species, assuming homogeneous, unidirectional flows and no spatial variation is therefore given as

$$\frac{dn_A}{dt} = \frac{c_B}{2} n_B^2 - c_A n_A \tag{3.4a}$$

$$\frac{dn_B}{dt} = -c_B n_B^2 + 2c_A n_A \tag{3.4b}$$

where $c_A = c_{Aeq}\lambda_{1A}$ and $c_B = c_{Beq}\lambda_{1A}N_{A0}$ are the rates for breaking and rejoining of long and short chains respectively. Eq. (3.4) is identical to Eq. (2.4) in Chapter II. N_{A0} is the number of long chains at equilibrium.

The equations for the motion of the micelle beads and slip-links are then given by

Eq. (3.5) and Eq. (3.6)

$$\zeta\frac{d\mathbf{r}_i}{dt} = \frac{3k_BT}{N_{k,s}b_K^2}(\mathbf{r}_{i+1}-2\mathbf{r}_i+\mathbf{r}_{i-1})+\mathbf{f}_i(t)+\frac{3k_BT}{N_sb_K^2}\sum_{j:trunc(x_j)=i}(1-(x_j-trunc(x_j)))(\mathbf{a}_j-\mathbf{s}_j) + \sum_{j:trunc(x_j)=i-1}\frac{3k_BT}{N_sb_K^2}(x_j-trunc(x_j))(\mathbf{a}_j-\mathbf{s}_j) \quad (3.5)$$

$$\zeta_s\frac{dx_j}{dt} = \frac{3k_BT}{N_sb_K^2}(\mathbf{r}_{trunc(x_j)+1}-\mathbf{r}_{trunc(x_j)})(\mathbf{a}_j-\mathbf{s}_j)+\mathbf{g}_j(t) \quad (3.6)$$

$\mathbf{f}_i(t)$ and $\mathbf{g}_j(t)$ are Brownian forces from the bombardment of the micelle beads and slip-links respectively by solvent molecules. They have a zero-mean and variances given by Eq. (3.7) and Eq. (3.8) respectively.

$$< f_i(t)f_j(t') >= 6k_BT\zeta\mathbf{I}\delta(t-t')\delta_{ij} \quad (3.7)$$

where $\mathbf{I}$ is the unit tensor.

$$< g_i(t)g_j(t') >= 6k_BT\zeta_s\delta(t-t')\delta_{ij} \quad (3.8)$$

The stress is computed (Eq. (3.9))as an ensemble average of the stress contributions from the individual springs in the wormlike micelles.

$$\boldsymbol{\sigma}_A = n_A\sum_{k=1}^{N-1}H\langle\mathbf{Q}_k\mathbf{Q}_k\rangle \quad (3.9a)$$

$$\boldsymbol{\sigma}_B = n_B\sum_{k=1}^{N_B-1}H\langle\mathbf{Q}_k\mathbf{Q}_k\rangle \quad (3.9b)$$

where N_A and N_B are the number of beads in chains A and B respectively. In absence of reversible scission, this formulation is a two-specie multi-chain equivalent of the single-chain slip-link model [15]. It is noteworthy to mention that in contrast to [15, 6], we do not prevent the slip-links from passing through each other in these simulations.

Allowing them to pass through each other was acknowledged as producing "a very small" difference by Likhtman [15].

In our simulations, for simplicity, we represent the wormlike micelles as Hookean beads and springs. N_A was chosen to be 13 with $Z = 3$ implying that the long micelles have one entanglement for every four beads, in line with the recommendation of Likhtman [15]. This places the system in the semi-dilute regime. $N_{k,s}$ and N_s were set to 6, i.e. 6 Kuhn segments per spring in the micelles and virtual chains. The simulations were run using with a time step of $\lambda_{R|(N_A-1)}/250$, where $\lambda_{R|(N_A-1)}$ is the shortest Rouse time of the relaxation spectrum for long micelles (Eq. (3.10) for Rouse chains) and an ensemble of 5,000 long and short chains each. Cruz, Chinesta, and Régnier reported that a BD simulation time-step of $\lambda_{R|(N-1)}/500$ for an ensemble of 5,000 ordinary Rouse chains provides a good compromise between computational cost and accuracy [17]. We find that a time step that is twice as big for an ensemble of 5,000 chains each for each species chain seems to be a good compromise between speed and accuracy for our simulations.

$$\lambda_{R|(N_A-1)} = \frac{\zeta N_{k,.s} b_K^2}{24 k_B T \sin^2\left((N_A-1)\pi/2N_A\right)} \tag{3.10}$$

3.3 Results and Discussion

In the absence of reversible scission, that is, simulating as the chains as unbreakable ordinary polymers, Fig. 3.2 shows that the presence of entanglements lead to increased stress. There is over a four-fold increase in the steady stress of the long species due to the additional forces that the three entanglements exert on the monomers of the polymer. An initial stress overshoot is observed in the stress response curve indicative of a nonlinear response of the polymers to the deformation. In this case, the additional effect of the potentials from the entanglements lead to nonlinear stretching of the polymers at a rate faster than they can relax the stretch by reptation.

This in turn causes the polymer to feel stresses beyond their steady values hence the stress overshoot. However, at long enough times, say about three times the longest Rouse times, λ_{RA}, the effect of the relaxation by reptation on the stretched polymers leads to a down-turn in the transient stress. At about $6\lambda_{RA}$, the instantaneous stress approaches a steady state value. The stress seems not to reach its steady value at this point but oscillates about it for up to 20 Rouse times. Occurrence of such long transients after stress overshoots have been reported [18] for entangled polymer-like micelle solutions under start-up shear flow.

The dynamics of the short polymers (blue curves in Fig. 3.2) reveal that the impact of an additional entanglement on the polymer is minimal compared to the case of 3 entanglements described above. The added potential of the entanglement to the 6-spring polymer chains caused less than a two-fold increase in steady stress. The transient stress response did not exhibit stress overshoot. This implies that the polymers were only stretched moderately and they could relax the stretch relatively quickly, with little influence of entanglements. The relaxation is possible because (i) the short micelles are not sufficiently entangled to produce nonlinear stretching of the chains as in the case of the long polymers, and (ii) the relaxation time is an order of magnitude smaller than the inverse of the shear rate, $\lambda_{RB} < 1/\dot{\gamma}$ therefore, the short micelles can relax much of their stress before becoming highly stretched.

We now investigate the effect of reversible scission along with entanglements on the transient stress response of wormlike micelles in Fig. 3.3. We observe that the transient stress in the wormlike micelles with entanglements (continuous lines) increased significantly relative to wormlike micelles without entanglements. For similar reasons explained above, the stress increase as a result of the additional forces from the entanglements caused the chains to become highly stretched. There is therefore about a five-fold increase in the steady stress of the entangled long wormlike micelles compared to the unentangled ones. The relative increase in steady stress of the

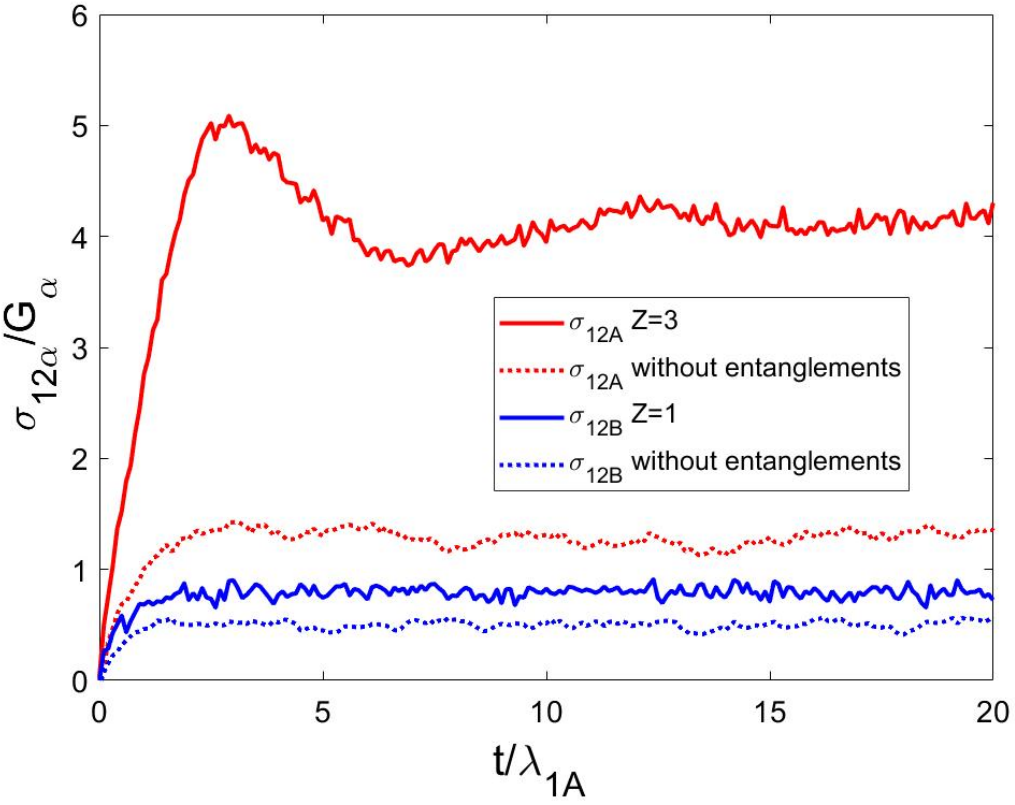

Figure 3.2: Transient stress response to start-up shear flow at Weissenberg number of unity based on the longest Rouse relaxation time of the long species. Increased steady stresses were observed in long and short species of 12 and 6 Hookean springs with 3 and 1 slip-links per chain respectively. Continuous lines represent the stress response of polymers with entanglements while the dashed lines represent the stress response of those without entanglements. A stress overshoot due to nonlinear stretching of the polymer chains was obtained for the long species that is sufficiently entangled to produce an overshoot. Stresses were averaged over an ensemble of 10^3 chains each for long and short polymers.

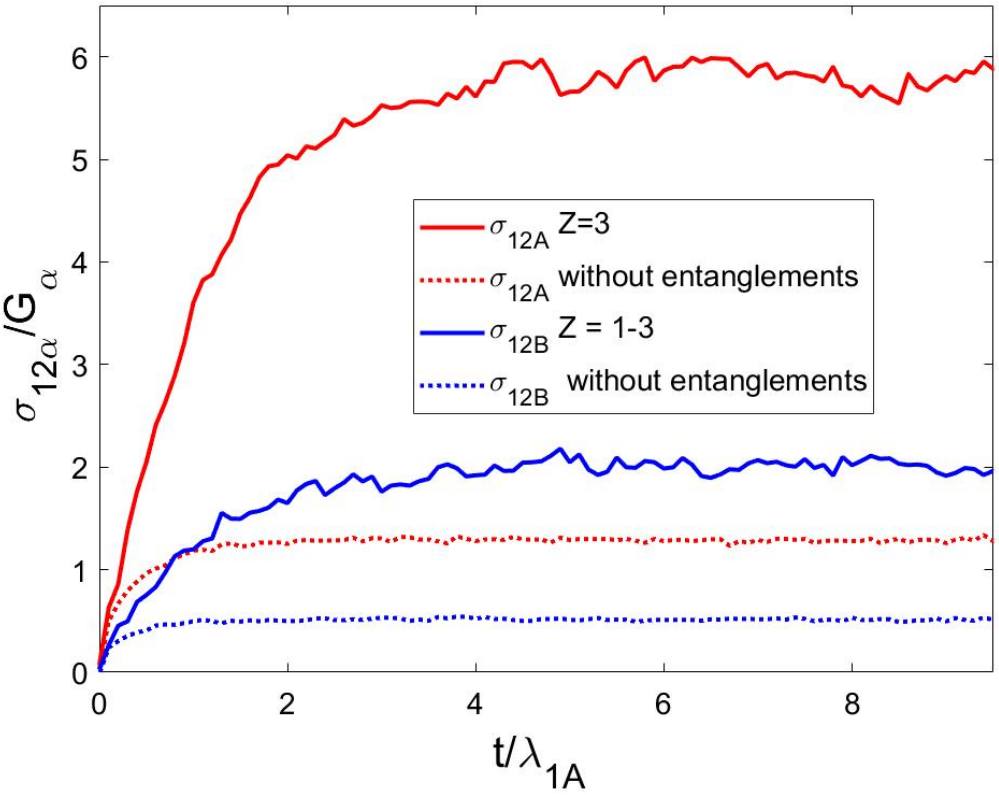

Figure 3.3: Transient stress response of wormlike micelles at conditions similar to Fig. 3.2 but with reversible scission at a scission rate of $c_{Aeq}\lambda_{1A} = 1$.

entangled micelles is slightly higher than that of the unentangled ones. A direct comparison of the stress response of the entangled wormlike micelles (continuous lines) and entangled unbreakable polymers (dashed lines) is shown in Fig. 3.4. This result is striking because it is counter-intuitive that reversible scission can lead to increase stress despite being a stress relaxation mechanism. We would offer explanations as to why this is possible in this simulated case below.

First, let's focus again on Fig. 3.3 to explain the interplay between the effects of reversible scission and entanglements. In the foregoing discussion, we explained that reptation is a slow relaxation process that cannot free the chains fast enough from their topological constrictions (and entanglements) before thy become highly stretched by the flow and entanglement forces. The rate of scission employed in entangled wormlike

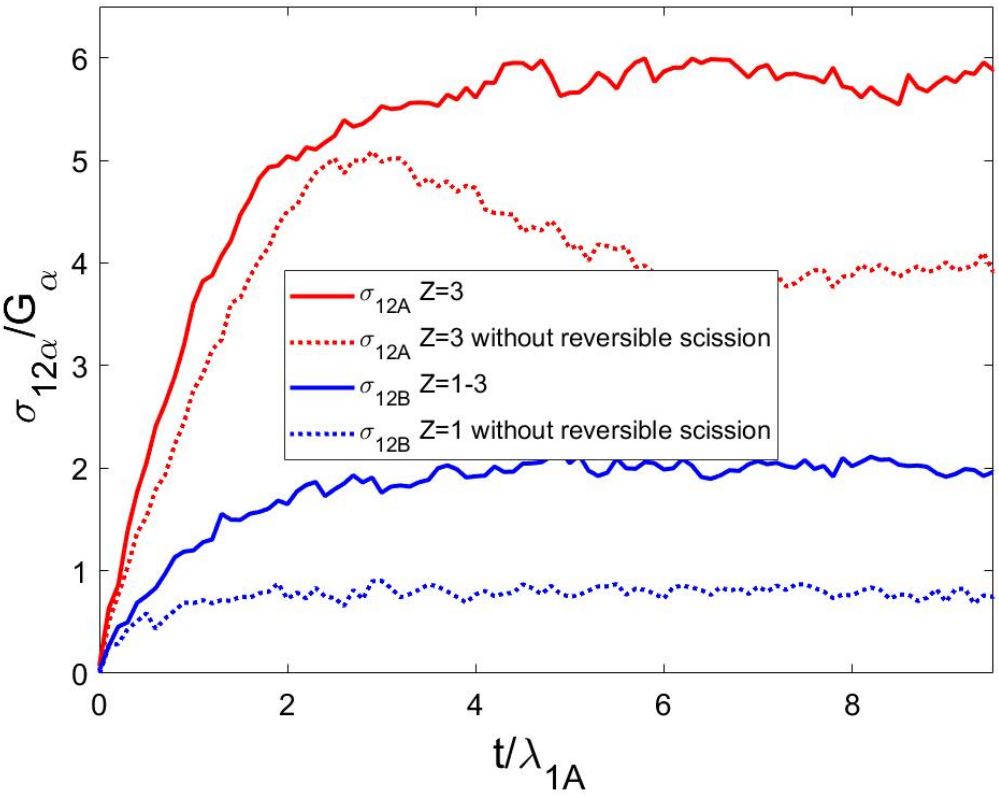

Figure 3.4: Comparison of the transient stress response of wormlike micelles -with and without reversible scission- at Weissenberg number of unity. Continuous lines represent the stress response of entangled wormlike micelles while the dashed lines represent the stress response of entangled polymers in which the reversible scission is shut off. Stress overshoot is absent in entangled wormlike micelles due to additional relaxation mechanism of reversible scission.

micelles of Fig. 3.3 is $c_{Aeq}\lambda_{1A} = 1$, where c_{Aeq} is the equilibrium scission rate and λ_{1A} or τ_{rep} is the longest Rouse relaxation time (or time for reptation). A dimensionless scission rate of one implies $\tau_b = \tau_{rep}$. Therefore, in our simulation results shown in Fig. 3.3, we can assume reptation as the dominant mode of relaxation. However, this does not explain the discrepancy in stress when making direct comparison between entangled wormlike micelles and polymers (see Fig. 3.4) for this particular case where relaxation is of the order of the reptation time in both cases.

The discrepancy can be explained by the effect of reversible scission. During reversible scission, the highly stretched long wormlike micelles break into shorter

pieces that (i) do not relax the stretch fast enough by reptation and (ii) contain entanglements of their own that imposes additional stress on them. The short micelles in the simulation described in Fig. 3.3 have between 0 and 3 entanglements with an average entanglement number, $\bar{Z} = 1.5$ on the 6-spring chain. Therefore, unlike in the polymer case, without exchange of species, additional stresses from unrelaxed entangled shorter micelles contribute to the total stress in the long micelles. As a result, the longer micelles cannot relax the high stress at the peak of the stress overshoot given the time for reptation and scission to a lower steady state value (as in the polymeric case). Consequently, the transient stress response curve plateaus by smoothing out the "overshoot" to steady state. It is possible that the stress relaxes to the final steady stress after several Rouse times. This behavior is reminiscent of flow-induced gel phases formed in shear thickening wormlike micelle solutions. They have been reported to take several hours or days to achieve steady stress [19, 20, 21]. Based on these findings, we anticipate that the entangled wormlike micelles have to be in the fast-breaking regime, $\tau_b << \tau_{rep}$ for the effects of reversible scission in stress relaxation to be effective.

An alternative explanation is that the reversible scission acts as a form of "constraint release" for the wormlike micelles. In the entangled polymer case (without reversible scission), the entanglements cause disorientation of the springs, thereby allowing the shear flow to stretch them. The long chains then orientate in the flow direction. Thus, there is little drag force on them and they retract in the "tube" leading to the overshoot and large drop in stress. However, in entangled wormlike micelles, the reversible scission causes new ends to be formed and allow for nearby slip-links to easily disentangle from the chain. The chain can reptate out of the new ends, free of the "tubular" constraints imposed by the slip-links and orientate freely in the flow. The freedom of chain segments to explore new conformations allow them diffuse across the gradient direction and lead to higher stress. Therefore, breaking

and rejoining of micelles act like constraint release and also prevent the retraction in the tube created by the slip links. This kind of behavior has been reported for entangled polymers with convective constraint release [22]. In our simulation, we have not explicitly implemented constraint release in the traditional sense [23, 24, 22, 25], it therefore suggests that reversible scission acts as a mechanism of constraint release.

We observed in Fig. 3.5 that as the dimensionless scission rate, $c_{Aeq}\lambda_{1A}$ is increased from 1 to 10, the transient stress increases. Additionally, we observe that for $c_{Aeq}\lambda_{1A} = 10$, the transient stress peaked after 3 Rouse times (of the long chains) at a stress of about 5 and 7 times the steady stress values obtained when $c_{Aeq}\lambda_{1A} = 1$ for long and short chains respectively. The transient stress then reduced to a steady stress which is roughly the same as the steady stress for $c_{Aeq}\lambda_{1A} = 2$, thereby creating a stress overshoot in the start-up flow curve. Therefore, we conclude that reversible scission, controlled by the scission rate, is partly responsible for the initial increase in stress of entangled wormlike micelles in response to start-up flow. The other factor is the entanglement effects. However, at very high scission rates, when the breakage time $\tau_b = 1/c_A$ is about an order of magnitude lower than the reptation time, τ_{rep}, the role of reversible scission as a mechanism of stress relaxation becomes more significant in lowering the stress from its initial peak value. Hence, we can state that the stress response in entangled wormlike micelles is an interplay between entanglement and reversible scission. The initial stress to the peak value is by stretching of the chains by entanglements coupled with reversible scission acting as a means of constraint-release thus reorienting the micelles along the flow gradient direction. The subsequent relaxation is by reversible scission and reptation.

3.4 Summary

We present a novel formulation for simulating entangled wormlike micelles by incorporating reversible scission in an established slip-link model. This enables us add

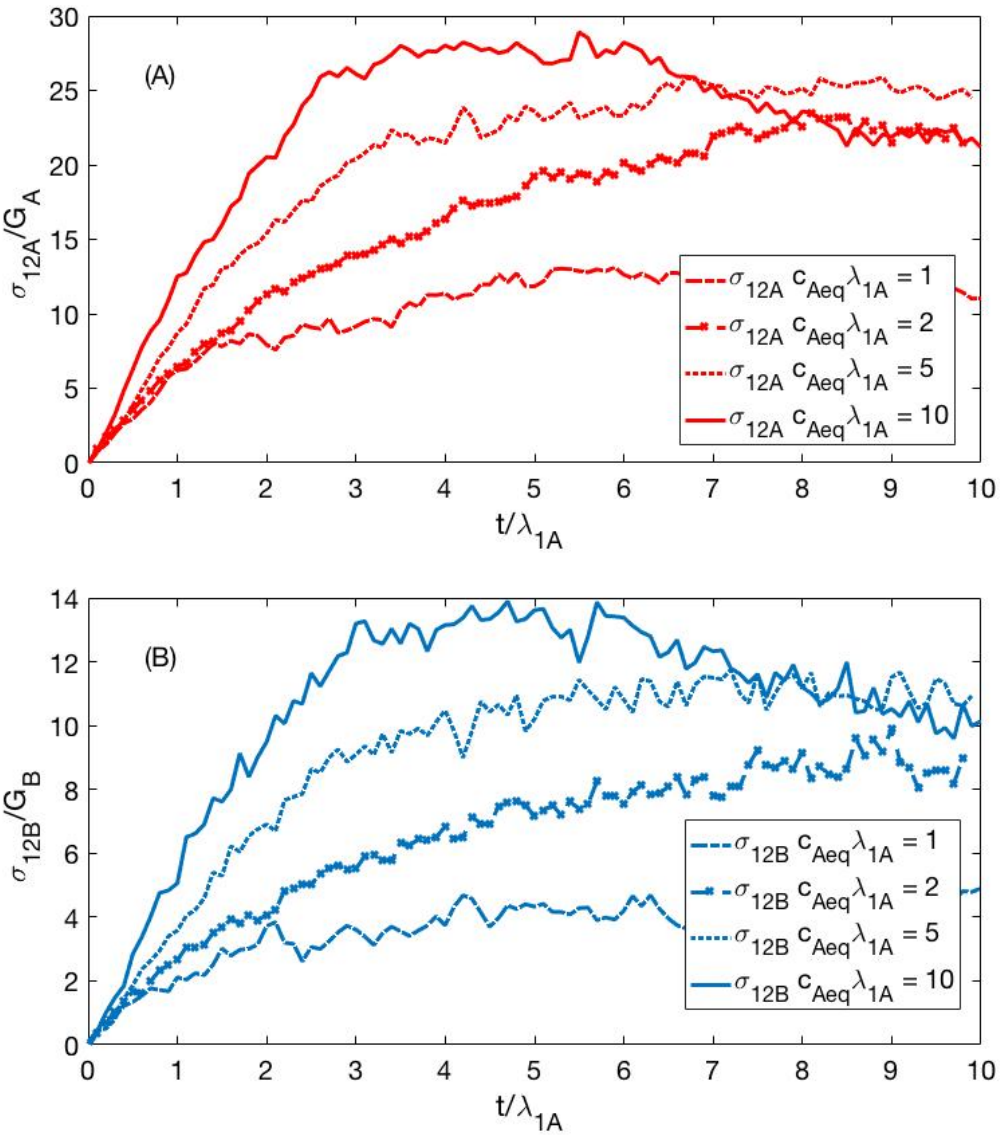

Figure 3.5: Comparison of the transient stress response of wormlike micelles with varying scission rates at Weissenberg number of unity. The long micelles have 12 springs with an average of 6 slip links per chain and short micelle chains have 6 springs with an average of 3 slip links per chain. The transient stresses of long chains are shown in (A) while the comparison for the short chains are in (B).

entanglement dynamics to the existing reversible scission and reptation dynamics for wormlike micelles. We therefore study the effects of reversible scission and entanglements on the rheology of wormlike micelles. We find that entanglements cause increased steady stress and stress overshoot in polymer species with sufficient entanglements (about one entanglement per four beads). In entangled wormlike micelles, reversible scission on the order of Rouse time leads to an even higher steady stress without stress overshoot, for same conditions as in polymers. Reversible scission in the fast-breaking regime, where breakage times are much more faster than reptation is needed for the stress relaxation effects to be significant, causing a corresponding decrease in steady stress and therefore, the occurrence of a stress overshoot.

Bibliography

[1] P.-G. de Gennes, *Scaling Concepts in Polymer Physics*, 1st ed. (Cornell University Press, Ithaca and London, 1979) p. 326.

[2] M. Doi and S. F. Edwards, *The theory of polymer dynamics* (Oxford University Press, Oxford, 1986) p. 391.

[3] S. Edwards, Proc. Phys. Soc. **92**, 9 (1967).

[4] R. C. Ball, M. Doi, S. F. Edwards, and M. Warner, Polymer **22**, 1010 (1981).

[5] S. F. Edwards and T. Vilgis, Polymer **27**, 483 (1986).

[6] M. Rubinstein and S. Panyukov, Macromolecules **35**, 6670 (2002), arXiv:0303592 [cond-mat] .

[7] W. Kuhn, Journal of Polymer Science **1**, 380 (1946).

[8] F. T. Wall and P. J. Flory, The Journal of Chemical Physics **19**, 1435 (1951).

[9] P. J. Flory, Proceedings of the Royal Society of London. Series A, Mathematical and Physical Sciences **351**, 351 (1976).

[10] H. M. James and E. Guth, The Journal of Chemical Physics **11**, 455 (1943).

[11] H. M. James and E. Guth, The Journal of Chemical Physics **15**, 669 (1947).

[12] G. Ronca and G. Allegra, The Journal of Chemical Physics **63**, 4990 (1975).

[13] B. Erman and J. E. Mark, *Structures and Properties of Rubberlike Networks*, edited by J. E. Mark (Oxford University Press, New York, 1997) p. 383.

[14] M. Rubinstein and S. Panyukov, Macromolecules **30**, 8036 (1997).

[15] A. E. Likhtman, Macromolecules **38**, 6128 (2005).

[16] D. Del Biondo, E. M. Masnada, S. Merabia, M. Couty, and J. L. Barrat, Journal of Chemical Physics **138** (2013), 10.1063/1.4799263, arXiv:1306.2107 .

[17] C. Cruz, F. Chinesta, and G. Régnier, Archives of Computational Methods in Engineering **19**, 227 (2012).

[18] C. R. López-Barrón, a. K. Gurnon, A. P. R. Eberle, L. Porcar, and N. J. Wagner, Physical Review E - Statistical, Nonlinear, and Soft Matter Physics **89**, 042301 (2014).

[19] E. Kaler and R. Zana, *Giant Micelles*, edited by E. Kaler and R. Zana, Surfactant Science, Vol. 20074445 (CRC Press, 2007) p. 2013.

[20] J. F. Berret, R. Gamez-Corrales, J. Oberdisse, L. M. Walker, P. Lindner, R. Gámez-Corrales, J. Oberdisse, L. M. Walker, and P. Lindner, Europhysics Letters **41**, 677 (1998).

[21] R. Oda, V. Weber, P. Lindner, D. J. Pine, E. Mendes, and F. Schosseler, Langmuir **16**, 4859 (2000).

[22] D. W. Mead, R. G. Larson, and M. Doi, Macromolecules **31**, 7895 (1998).

[23] G. Marrucci, Journal of Non-Newtonian Fluid Mechanics **62**, 279 (1996).

[24] G. Ianniruberto and G. Marrucci, Journal of Non-Newtonian Fluid Mechanics **65**, 241 (1996).

[25] J. M. Dealy and R. G. Larson, *Structure and rheology of molten polymers: from structure to flow behavior and back again* (Hanser Publishers, Cincinnati, 2006) p. 516 p.

CHAPTER IV

Concentration and Temperature Dependence of Strain Hardening in CTAB/NaSal Surfactant Solutions

4.1 Introduction

Surfactant molecules can reversibly self-assemble into micelles at concentrations above the critical micelle concentration (cmc). The structure of the micelles depends upon factors such as surfactant concentration, ionic strength, type of solvent, temperature and presence of counterion and/or co-surfactant [1, 2, 3]. In ionic micellar solutions, electrostatic screening of the charged head-groups induces the growth of micelles by lowering the effective area that each head-group occupies on the surface of the micelle, thereby favoring lower curvature of the micelle surface. This allows the micelles to grow rapidly and transform from spherical to cylindrical morphologies at much lower surfactant concentrations. The screening is achieved by adding a suitable counterion, co-surfactant, and/or salt [4]. Upon addition of salts, the aggregation number therefore typically increases, leading to the formation of giant wormlike micelles (WLMs) [5]. Certain salts can have additional effects on surfactant micelles. For example, hydrotropes, which are aqueous salts of organic molecules (mostly aromatics), have the exceptional ability to solubilize hydrophobic compounds

[4]. Hydrotropes tend to be incorporated into the region of the micelle spanning the head group and the outer tail region due to their charge, hydrophobicity and size [5]. These micelles, when present at semi-dilute concentrations, exhibit pronounced viscoelasticity [2, 6]. They break and recombine dynamically which gives them stability in high-shear-rate applications [7]. Wormlike micelles (WLMs) relax stress primarily by two mechanisms: reversible scission (breaking and reforming along the micelle chain) and reptation - the snake-like motion of the wormlike micelle to free itself of the constrictions imposed by surrounding micelles [8, 3].

In small amplitude oscillatory shear flows, the linear viscoelastic response of many wormlike micelles is explained by a combination of reversible scission and reptation [9]. The stress decay can be modeled by a single exponential when chain scission is faster than reptation. WLM solutions also exhibit nonlinear rheological properties such as shear banding [10, 11, 4], flow-induced phase transitions [12, 13], shear thinning, shear thickening and strain hardening [14, 15, 16]. Shear-induced structures with entangled, branched and multi-connected micellar bundles have been reported [12] to form when wormlike micelles are subjected to high shear rates and strains. These shear-induced structures formed under strong shear flows have been invoked to explain shear-thickening [17].

Strain hardening in shear is usually probed by performing step strain experiments and is defined by a nonlinear stress relaxation modulus that increases relative to the response within the linear strain limit. A lower nonlinear relaxation modulus relative to the linear response indicates strain softening. Shikata *et al.* [14] showed that strain hardening in aqueous solutions of cetyltrimethylammonium bromide (CTAB) with added hydrotrope, sodium salicylate (NaSal) depends on the salt-to-surfactant concentration ratio. Brown, Burghardt, and Venerus [15] further investigated the CTAB/NaSal solution at equal molar concentrations and observed that the relaxation moduli were factorable into time- and strain- dependent functions in the strain

hardening regime ($2.0 < \gamma < 3.5$). The strain-dependent function is calculated as the amount of vertical shift on a log-log plot needed for the nonlinear stress relaxation curve to superimpose on the linear relaxation curve. This shift as a function of strain is the damping function. Such factorability has been observed in some polymers and the damping function is usually a strain softening function [18]. For a CTAB/NaSal surfactant solution, beyond a strain of 350% ($3.5 < \gamma < 4.0$), Brown, Burghardt, and Venerus observed a time-dependent collapse of the relaxation modulus from a strain hardening to a strain softening or linear response at a critical time after the step strain [15]. In start-up shear flows, an increase in the shear stress growth coefficient (defined as the ratio of shear stress to shear rate) relative to the linear response is also termed "strain hardening" [16, 19, 20]. In such start-up shear flow experiments on CTAB/NaSal wormlike micelles, Inoue, Inoue, and Watanabe [16] observed strain hardening at shear rates higher than a critical shear rate.

In step strain experiments, strain hardening has been observed in wormlike micelles of CTAB with the hydrotrope NaSal at equal molar concentrations [15] and at a hydrotrope-to-surfactant molar concentration ratio, C_S/C_D of 1.5 [14]. However, the mechanism and conditions necessary for strain hardening in wormlike micelles is not clearly understood. A detailed study of the salt dependence of strain hardening is yet to be conducted, to the best of our knowledge. The dependence of strain hardening on parameters such as temperature has also not been studied. In this paper, we use stress relaxation after a sudden step strain to explore strain hardening in CTAB/NaSal wormlike micelles over a wide range of salt-to-surfactant concentration ratios, from 0.3-5.0. We also investigate the effects of temperature on strain hardening by performing experiments within the range 15 - 25 °C. We introduce a quantitative measure for strain hardening and extend previous work [14, 15] to give a more complete picture of the effect of hydrotrope concentration and temperature on strain hardening. For comparison and contrast, we also present step-strain results

of other wormlike micelle solutions without the hydrotrope but in the presence of a simple salt, namely sodium lauryl ether- 1 sulfate (SLE1S) with sodium chloride, and a mixture of sodium lauryl ether- 3 sulfate (SLE3S) and sodium lauryl sulfate (SLS) with NaCl. We conclude with a discussion and propose a mechanism for strain hardening in worm-like micelle solutions.

4.2 Experimental Section

Cetyl trimethylammonium bromide (CTAB) and sodium salicylate (NaSal) were purchased from Sigma-Aldrich. Sodium chloride and high performance liquid crystallography (HPLC) grade water were purchased from Fisher-Scientific. Sodium 3-Hydroxy-2-naphthoate (SHNC) was purchased from TCI America. Sodium lauryl sulfate (SLS), sodium lauryl ether- 3 sulfate (SLE3S) and sodium lauryl ether-1 sulfate (SLE1S) were generously donated by Procter & Gamble. The CTAB-hydrotrope wormlike micellar solutions were prepared by weighing the desired amount of surfactant and dissolving it in double filtered HPLC-grade water using 0.22 micron membrane filters. The appropriate amount of hydrotrope to make the desired salt-to-surfactant ratio, C_S/C_D, was then added to the solution. The mixture was then left to equilibrate at a constant temperature in a water bath for five days. The bath temperature was set higher than the Krafft temperature, the minimum temperature above which micellization occurs. CTAB/NaSal solutions have Krafft temperatures ranging between 22 and 25 °C [21]. Therefore, they were equilibrated at 25 °C. The CTAB/SHNC solutions were equilibrated at 40 °C. The CTAB/NaSal solutions were prepared with fixed surfactant concentration $C_D = 0.1$ mol/L and varying NaSal concentrations to obtain molar concentration ratios C_S/C_D ranging from 0.3 - 5.0. Three CTAB/SHNC solutions were prepared: 60 mM CTAB/ 30 mM SHNC, 100 mM CTAB/ 50 mM SHNC and 75 mM CTAB / 24 mM SHNC giving hydrotrope-to-surfactant concentration ratios of 0.5, 0.5 and 0.32 respectively. The linear rheology

and large amplitude oscillatory shear (LAOS) of 75 mM CTAB / 24 mM SHNC wormlike micelle solution has been studied in the literature [22]. The mixed-anionic wormlike micelle solution contained 42 wt.% sodium lauryl ether- 3 sulfate (SLE3S), 24 wt.% sodium lauryl sulfate (SLS), 3.5 wt.% sodium chloride (NaCl) and 30.5 wt% deionized water. The second anionic wormlike micelle solution was composed of 10 wt.% sodium lauryl ether-1 sulfate (SLE1S), 3.15 wt% sodium chloride(NaCl) and 86.85 wt% deionized water.

Rheological measurements were performed using a stress-controlled AR-G2 rheometer from TA Instruments with a cone-and-plate geometry. The cone had a diameter of 40 mm, an angle of $1°59'$ and a truncation gap of 44 microns. A 50 mm diameter solvent trap was used to prevent evaporation of the sample during measurements. Strain sweep experiments were performed at a frequency of 6.28 rad/s to determine the onset of the nonlinear regime. These showed that the onset of the nonlinear regime was at a strain of around unity for the entire concentration range explored. A frequency sweep from 0.03 to 100 rad/s at a constant strain amplitude of 5 % was used to measure the linear viscoelastic spectrum of the solution. The plateau modulus is strain-insensitive in the linear strain limit, where we measure our linear moduli. The linear plateau moduli, G_0 and relaxation times, τ were determined from these data. The linear plateau moduli were estimated from the nearly frequency-independent high frequency storage moduli. The plateau moduli for CTAB/NaSal wormlike micelles with $C_S/C_D = 0.3-0.8$ were nearly constant in the $0.3-10.0$ rad/s frequency range while solutions for which $C_S/C_D = 0.9-1.4$ and $C_S/C_D = 1.5-5.0$ were almost constant within the frequency ranges of $2.0-80.0$ and $2.0-20.0$ rad/s respectively. The relaxation time was taken as the inverse of the frequency at which storage (G') and loss (G") moduli were equal. Strain hardening was investigated by applying a step strain to the wormlike micelles and then the transient response of the relaxation modulus. The "rise-time" to achieve the desired strain was less than 0.1 s

for all measurements. The temperature was held constant at the desired value using a Peltier plate system. To determine the temperature dependence of strain hardening, the experiments were conducted at 15, 20 and 25 °C. Limited studies were performed for the CTAB/SHNC solutions to discover if they exhibit strain hardening behavior. Step-strain experiments were repeated three times for each surfactant/salt mixture, with good reproducibility for the same mixture. However, significant variation was observed for different remixes of the same composition. As described below, these mix-to-mix variations are quantified by computing the standard error for between 2-5 remixes of the same composition.

4.3 Results

The results are organized as follows. First, we present the linear viscoelastic data of the wormlike micelle solutions. Then, the nonlinear stress relaxation data for the SLES wormlike micelles that lack a hydrotrope are shown. Finally, the stress relaxation data of the CTAB wormlike micelle solutions that contain a hydrotrope are presented with their concentration and temperature dependencies.

4.3.1 Linear viscoelasticity

The linear viscoelastic response for the $C_S/C_D = 1.2$ CTAB/NaSal wormlike micelle solution at 25 °C is shown in Fig. 4.1. A single-mode Maxwell model [2] fit to the curves yields relaxation times of $\tau = 0.87, 0.09$ and 0.14 s and plateau moduli $G_N^0 = 54.2, 399$ and 160 Pa for CTAB/NaSal, SLE3S/SLS/NaCl and SLE1S/NaCl wormlike micelle solutions respectively. We observed modest deviations from the single-mode Maxwell model at high frequencies. Figure 4.2 shows the dependence of the steady shear viscosity on shear rate for the CTAB/NaSal, SLE1S/NaCl and SLE3S/SLS/NaCl solutions. Plotting the low-shear-rate (i.e., the zero-shear-rate) values of the shear viscosities against salt concentration gives the so-called "salt curve"

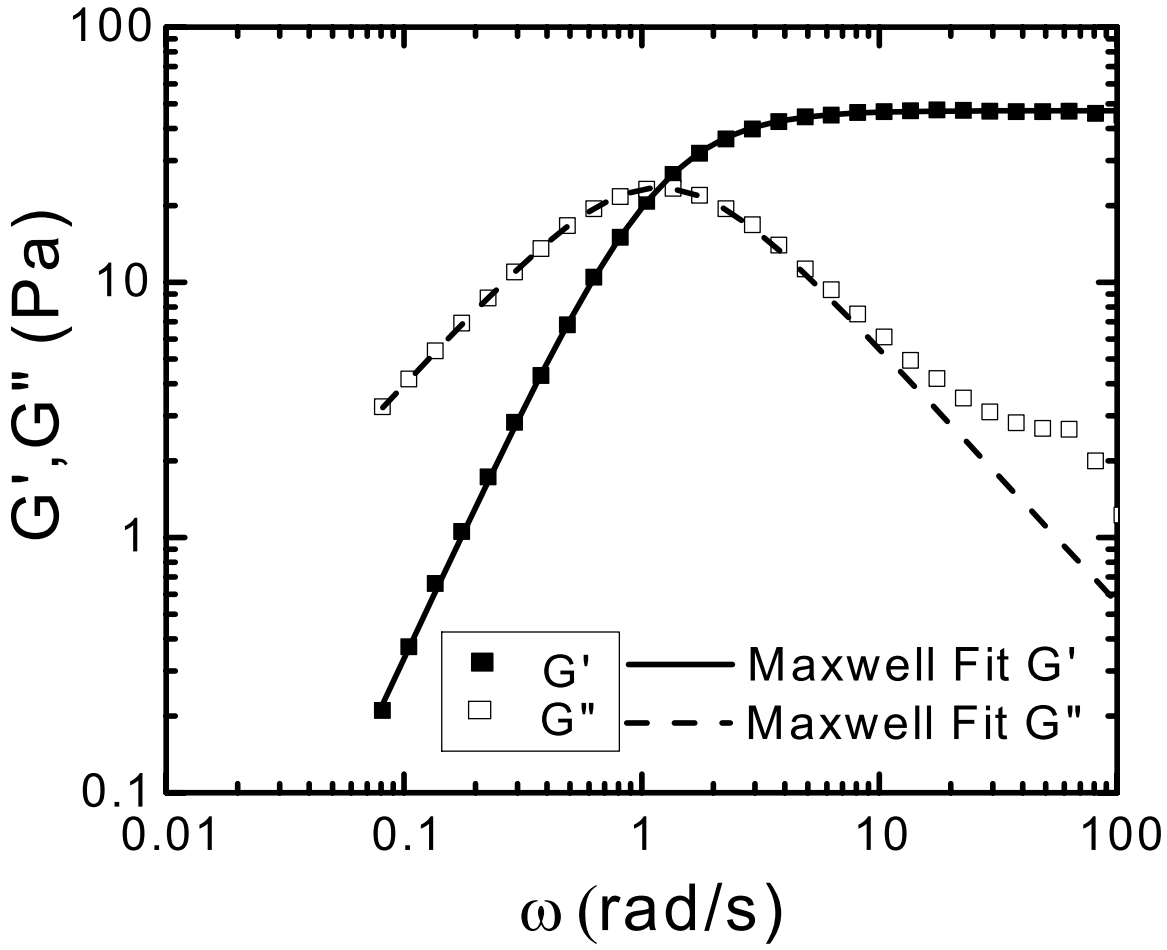

Figure 4.1: Linear viscoelastic moduli of 0.1 M CTAB with NaSal at salt to surfactant concentration ratio, $C_S/C_D = 1.2$. The measurement was taken at 25 °C. Continuous and dashed lines are single-mode Maxwell model fits to the storage and loss moduli respectively.

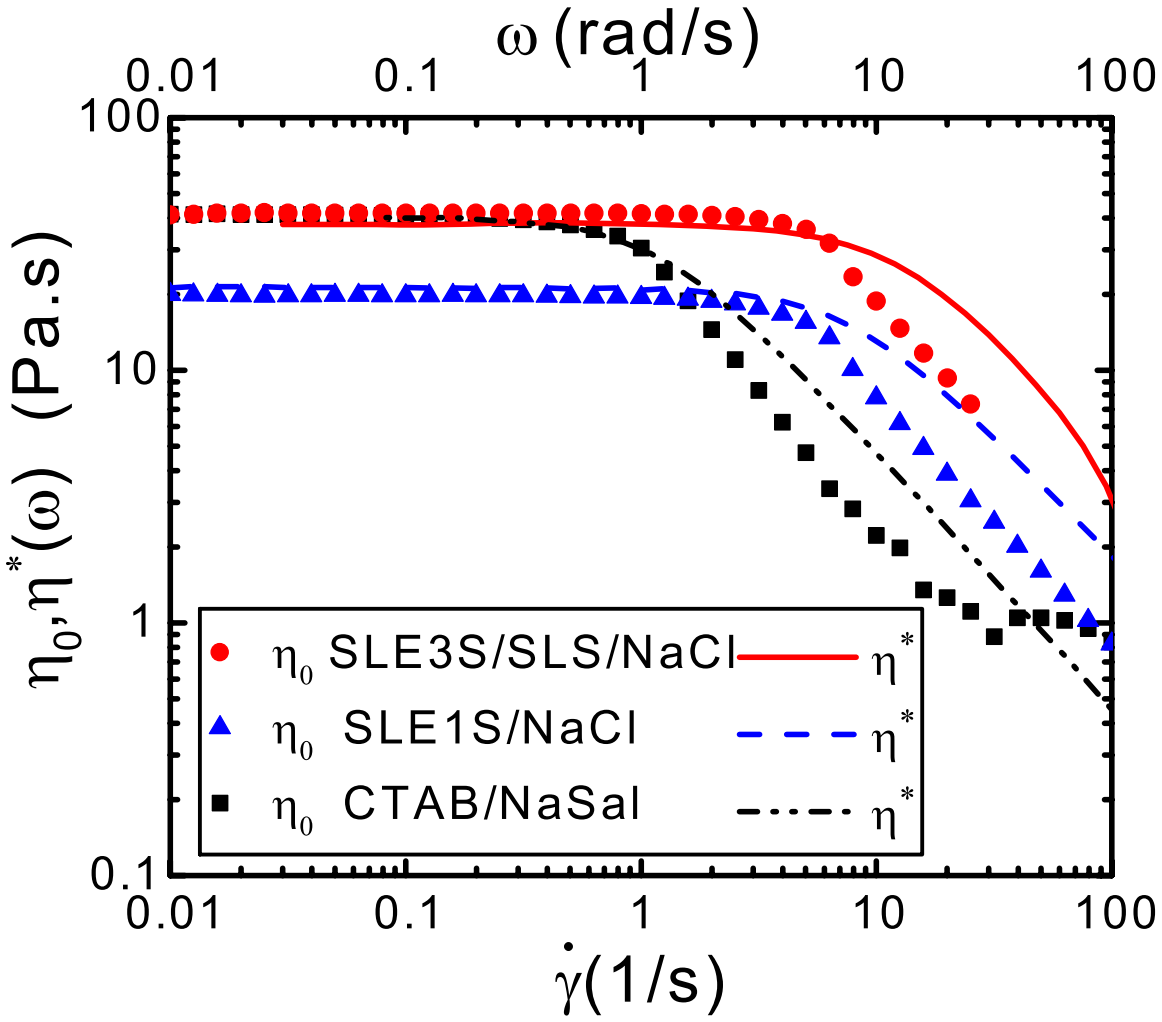

Figure 4.2: Dependence of the steady shear viscosity on shear rate (symbols) and complex viscosity on angular frequency (lines) for 0.1 M CTAB / 0.12 M NaSal, SLE3S (42 wt%) / SLS (24 wt%), 3.5 wt% NaCl in 30.85 wt% deionized water and 10 wt% SLE1S with 3.15 wt% NaCl in 86.85 wt% deionized water are shown in the inset at 25 °C.

[23]. The salt curve for 0.1 M CTAB with varying NaSal concentration reveals two peaks at C_S/C_D values of 0.6 and 2.2 with a minimum at $C_S/C_D = 1.1$ as shown in Fig. 4.3a which is similar to what has been observed in previous work [24, 25]. The salt curves for SLE3S/SLS/NaCl and SLE1S/NaCl in Fig. 4.3b each show a single peak, consistent with findings in previous work [26, 27, 28]. The zero shear viscosities rise as salt concentration increases to peak values of 45 and 20 Pa.s corresponding to 3.5 and 3.15 wt% NaCl for SLE3S/SLS and SLE1S solutions, respectively.

4.3.2 Stress relaxation

The stress relaxation curves for anionic SLE1S and SLE3S wormlike micellar solutions with simple salt, NaCl and no added hydrotrope are shown in Fig. 4.4. The figure shows a progressive strain softening as the magnitude of strain increases above the linear strain limit of about 100 %. The relaxation curves can be shifted vertically and superimposed over the linear strain response and thus show time-strain separability, similar to the behavior of entangled polymer solutions and melts. The relaxation curves on the log-log plot in Fig. 4.4 were vertically shifted to superimpose them onto the linear strain (strain $< 20\%$) response. The vertical shift required for superposition as a function of strain, γ is known as the damping function [18] h(γ) and is shown in Fig. 4.5 for SLE3S/SLS/NaCl and SLE1S/NaCl. The SLE3S/SLS/NaCl solution shows more strain softening (i.e. faster decrease in h with γ) than does SLE1S/NaCl. The damping function for the single-mode Giesekus model (SM-GM) [29] at long time given by eq. 4.1 was fit to the damping functions obtained from the stress relaxation curves.

$$h(\gamma) = \frac{1}{1 + \alpha(1-\alpha)\gamma^2} \tag{4.1}$$

where α is the anisotropic mobility parameter which represents the anisotropy in the relaxation rate of micelles along the direction of the orientation relative to that perpendicular to it. The SLE3S/SLS/NaCl and SLE1S/NaCl data were fit with

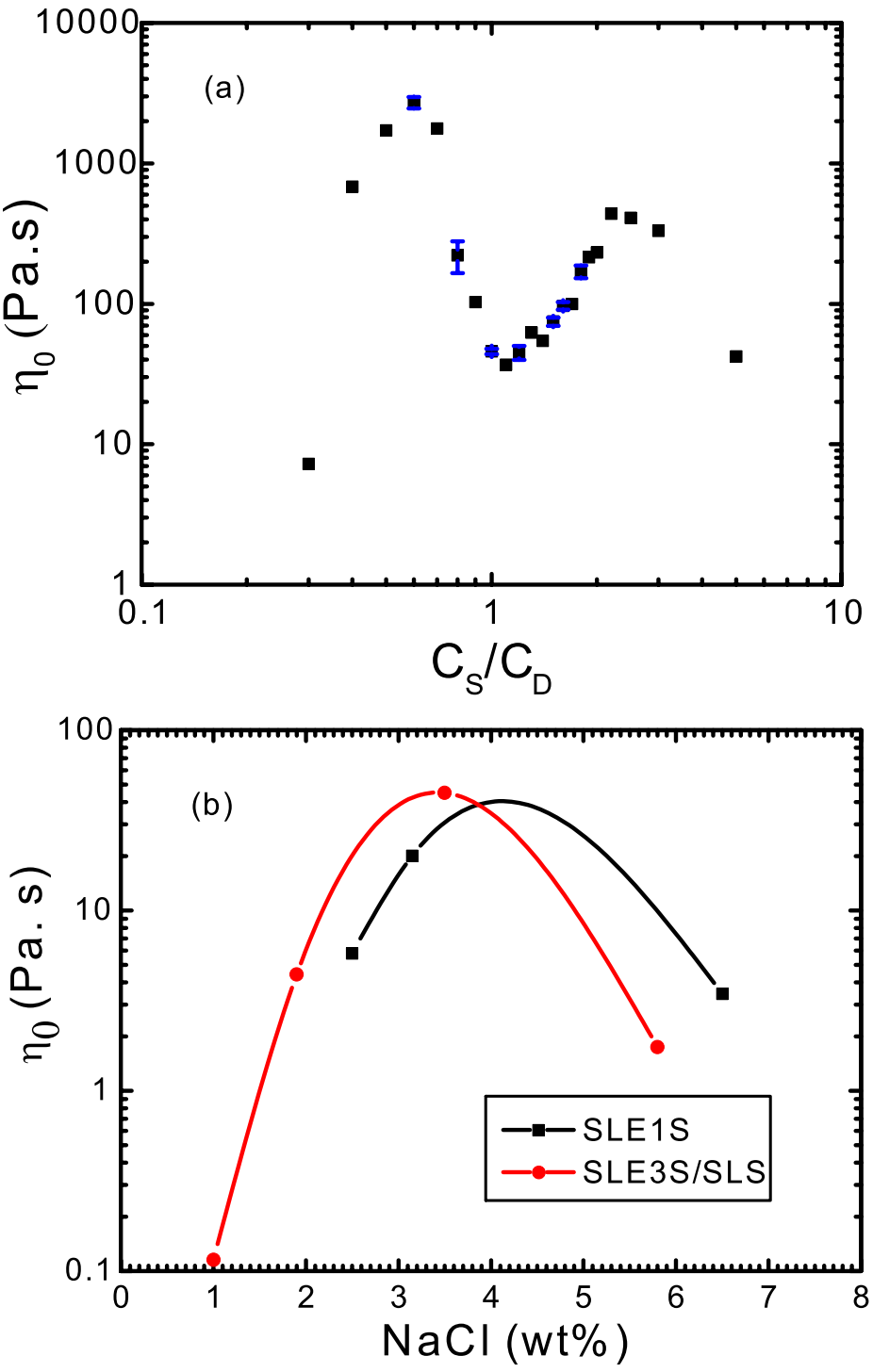

Figure 4.3: Dependence of zero shear viscosity on (a) NaSal to CTAB concentration ratio for CTAB/NaSal solutions at 25 °C and (b) weight percentage of NaCl in SLE1S/NaCl and SLE3S/SLS/NaCl solutions. The error bars in (a) represent the standard deviation from the mean of the zero-shear viscosities for 2, 2, 3, 2, 5, 3 and 2 samples each of solutions of $C_S/C_D = 0.6, 0.8, 1.0, 1.2, 1.5, 1.6$ and 1.8 WLMs respectively.

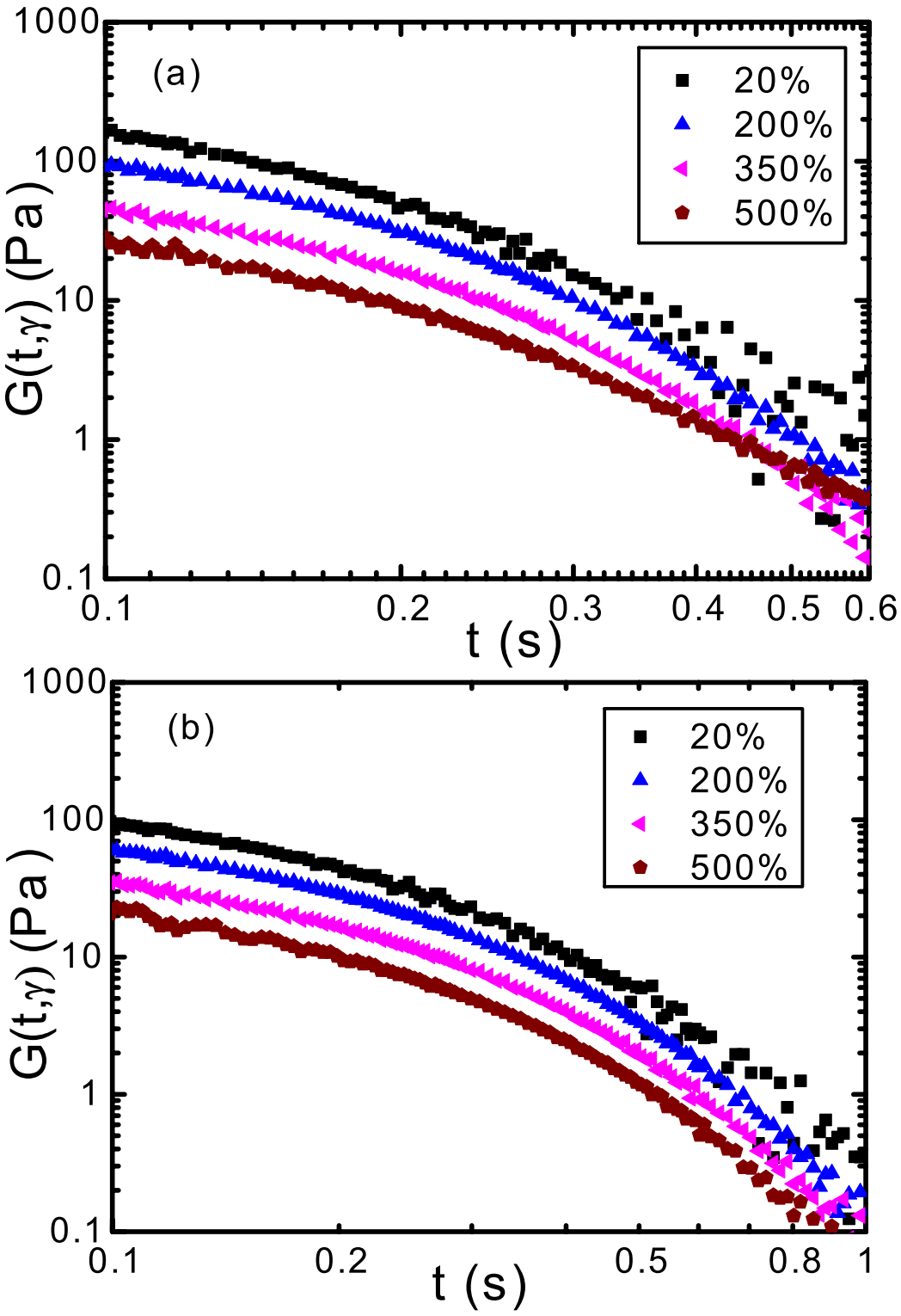

Figure 4.4: Stress relaxation curves at strains of 20, 200, 350 and 500% for (a) SLE3S/SLS with 3.5 wt% NaCl and (b) SLE1S with 3.15 wt% NaCl anionic wormlike micelle solutions at 25 °C.

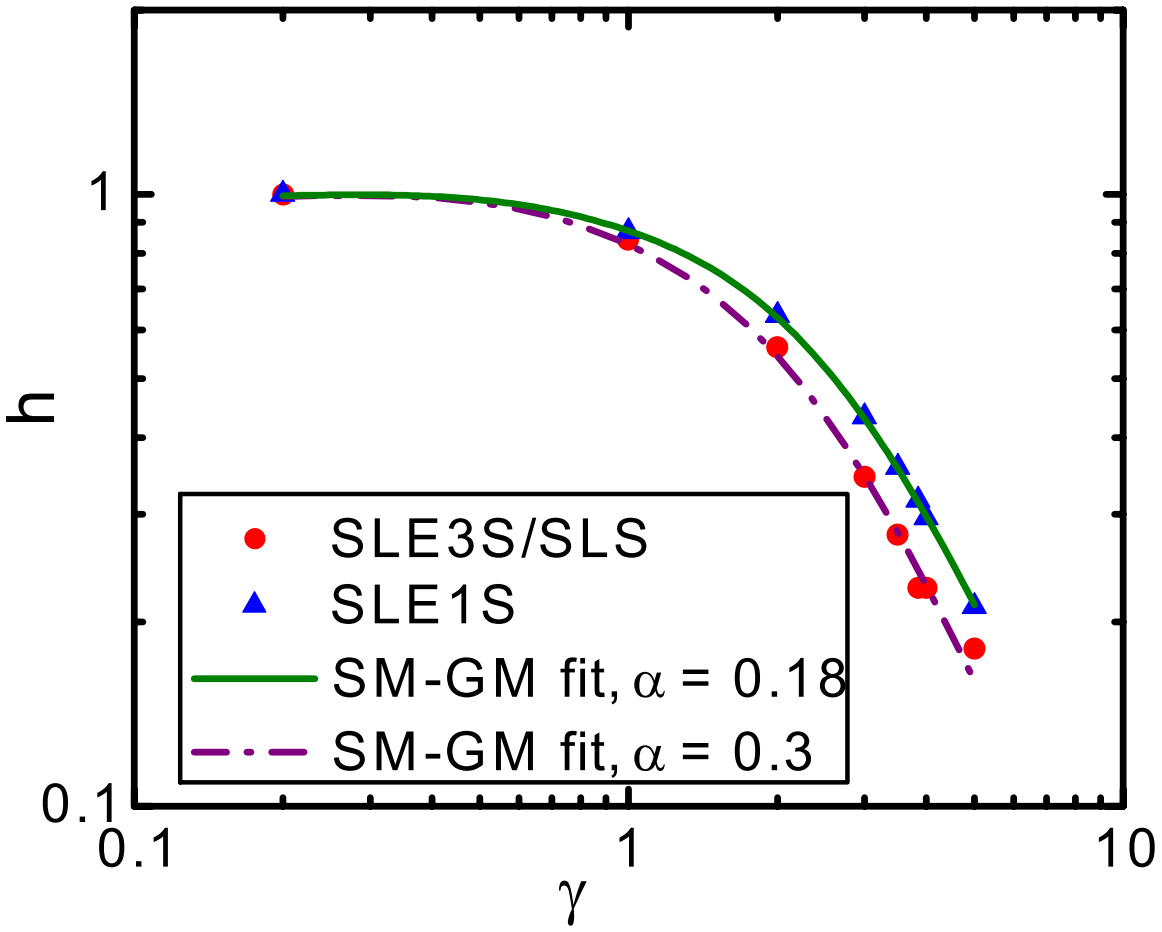

Figure 4.5: Damping function (h) as a function of strain (γ) for SLE3S/SLS with 3.5 wt% NaCl and SLE1S with 3.15 wt% NaCl at 25 °C. Fits to eq. 4.1 are shown.

anisotropy factors, α of 0.3 and 0.18 respectively. The relaxation curves for the CTAB/hydrotrope wormlike micelles on the other hand, are not time-strain separable and transition with time after the step strain from strain hardening to strain softening or back to the linear response. Similar trends were observed for other salt concentrations and temperatures.

Figure 4.6 shows stress relaxation curves exhibiting strain hardening for CTAB/NaSal. For $C_S/C_D = 1.2$ (Fig. 4.6a), the relaxation curve at 100 % strain superimposes on that of 20 % indicating that both strains are in the linear regime consistent with the strain sweep measurements (see Fig. D.1). A slight hardening response is observed at 200% strain while at 300 and 350 % strains, the relaxation moduli shows pronounced

strain hardening with moduli two and five times higher, respectively, than the linear response obtained at strains of 100 % and less. At a strain of 385 %, the initial pronounced hardening gradually wanes as the relaxation modulus decreases to the linear response. The relaxation curve at 400 % strain is roughly the same as the linear response at t = 0.1 s but then softens significantly with increasing time. Strain softening is also observed at 500 % strain; the relaxation modulus, $G(t, \gamma)$ is about 3 times lower in magnitude than the linear response. For some temperatures, salt concentrations and strains, we observe a transition of the relaxation modulus from strain hardening to strain softening similar to the findings of Brown, Burghardt, and Venerus [15]. As shown in Fig. 4.6b, the 0.1 M CTAB/NaSal solution at $C_S/C_D = 0.4$ exhibits only strain softening as the strain increases over the range 100-500 %. The pattern of decay of the nonlinear relaxation moduli with time is different however, from that seen for $C_S/C_D = 1.2$. The time dependence of the step strain response at 20 % strain can be modeled by a single exponential decay. In contrast, the response to 100 % strain shows two distinct relaxation periods. Figure 4.7 shows the response of the CTAB/SHNC wormlike micelles to step strain at 25 °C. The 60 mM CTAB / 30 mM SHNC solution exhibited strain hardening between 300 - 400% strains. However, the hardening transitioned to softening in about 1 s. The 75 mM CTAB/ 24 mM SHNC wormlike micelles experienced early "collapse" in the relaxation modulus before 0.1 s and was strain softening for all strains investigated. The nonlinear relaxation moduli displayed two distinct relaxation periods similar to Fig. 4.6b at $C_S/C_D = 0.4$. The 100 mM CTAB / 50 mM SHNC solution displayed progressive strain softening with increasing strain. This was in contrast to the behavior exhibited by the 60 mM CTAB / 30 mM SHNC wormlike micelles despite both solutions having the same hydrotrope-to-surfactant concentration ratio.

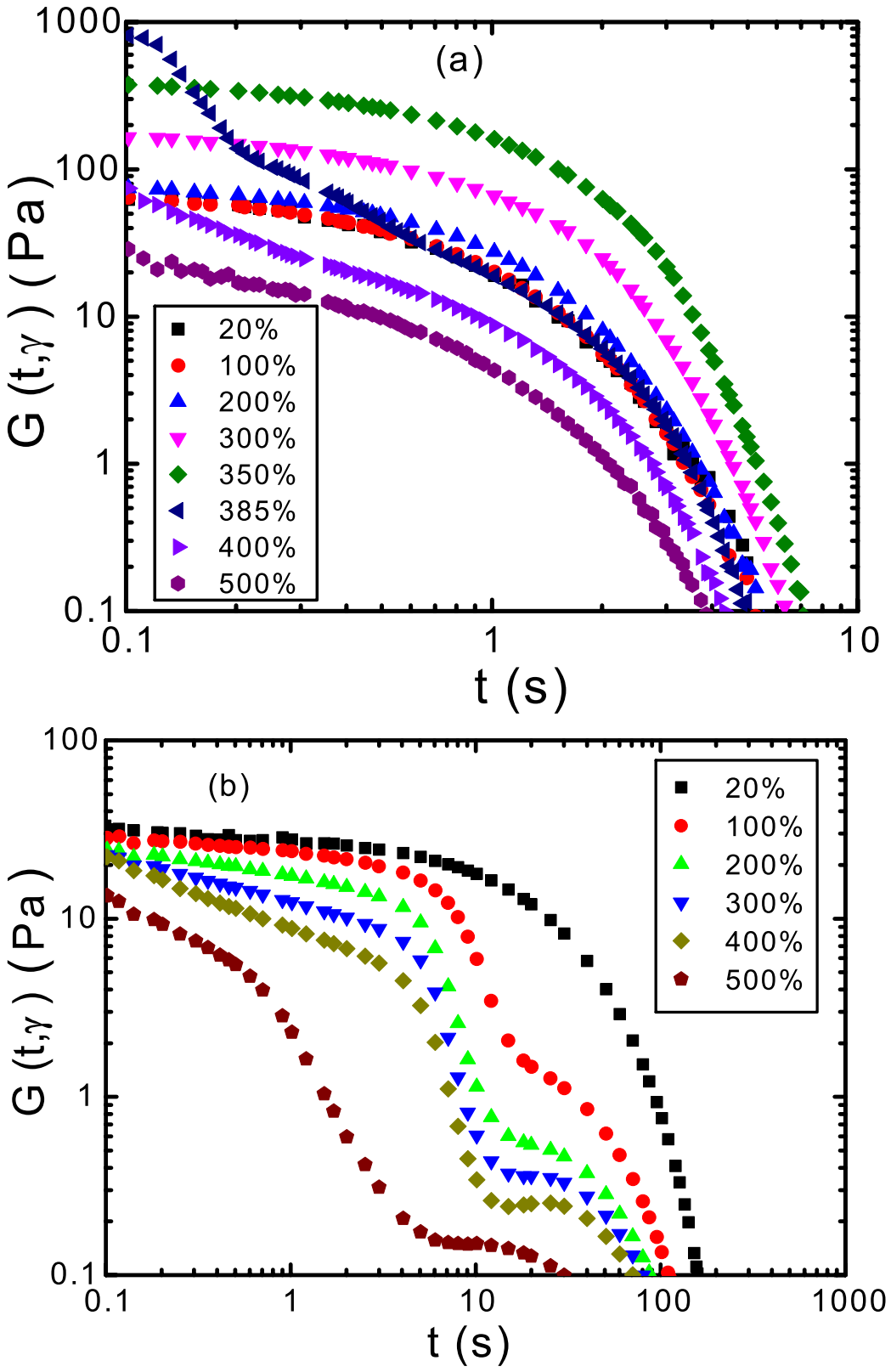

Figure 4.6: Nonlinear shear modulus at 25 °C for 0.1 M CTAB with NaSal at salt-to-surfactant concentration ratios (a) [NaSal]/[CTAB] = 1.2 and (b) [NaSal]/CTAB] = 0.4.

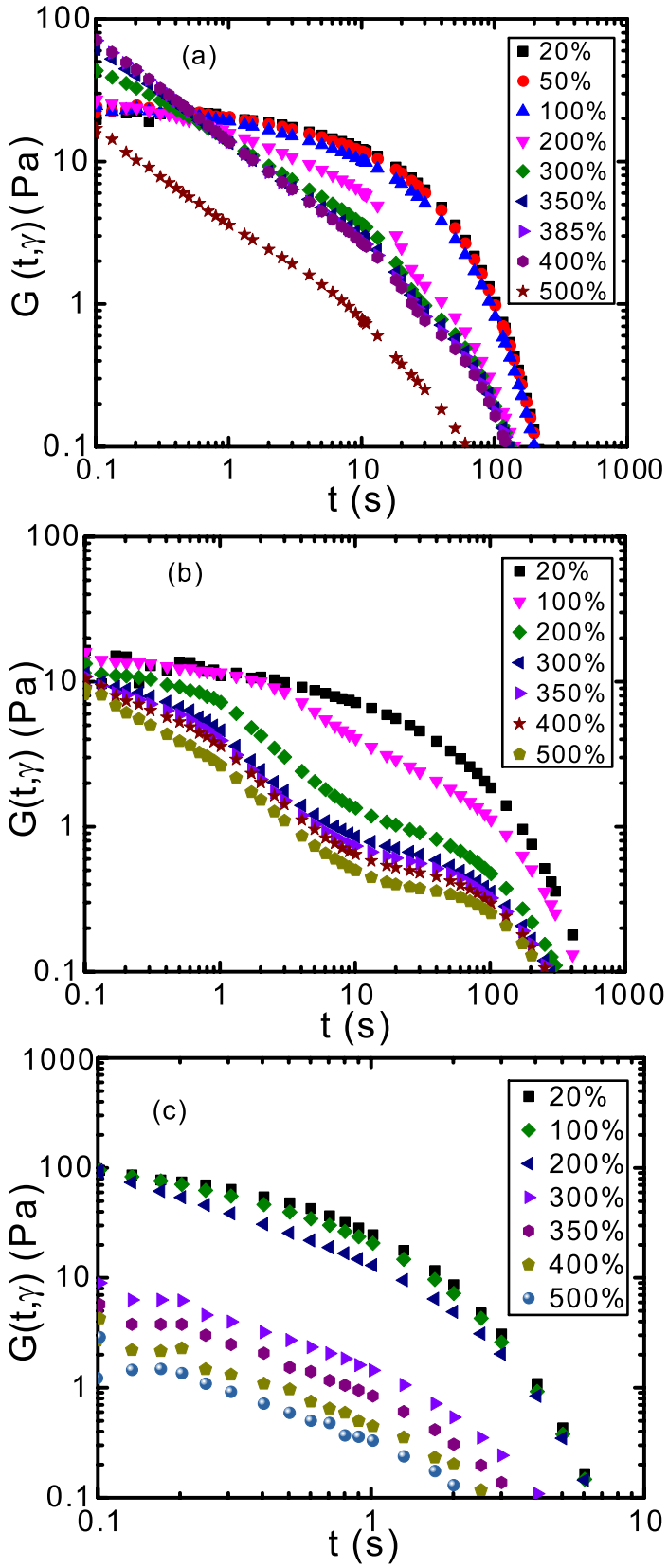

Figure 4.7: Nonlinear shear relaxation modulus after varying step strains at 25 °C for (a) 60 mM CTAB with 30 mM SHNC (b) 75 mM CTAB with 24 mM SHNC and (c) 100 mM CTAB with 50 mM SHNC wormlike micelle solutions.

4.3.2.1 Hydrotrope-to-Surfactant Concentration Dependence

Within the whole range of salt-to-surfactant concentration ratios of CTAB/NaSal micelle solutions studied here, namely 0.3 - 5.0, the relaxation curves shows strain hardening over the range $C_S/C_D = 0.5-3.0$. Thus, the relaxation behaves differently over the range $C_S/C_D = 0.3 - 0.5$ than for $C_S/C_D = 1.2$, as illustrated in Fig. 4.6. Within the hardening regime, $C_S/C_D = 0.5 - 3.0$, the change in hydrotrope concentration affects the magnitude of strain hardening and variation of the relaxation modulus with time after the step strain. For example, at a typical nonlinear strain of 350 % and fixed temperature of 20 °C, Fig. 4.8 shows that the initial strain hardening for $C_S/C_D = 0.5$ quickly collapses within 1 s to strain softening with two relaxation periods, while at $C_S/C_D = 1.0$, the hardening persists throughout the relaxation. A slight but persistent hardening is observed in $C_S/C_D = 1.5$ while the significant hardening at $C_S/C_D = 2.0$ lasts for about 10 s before strain softening.

To better quantify the magnitude of strain hardening, we define the "extent of hardening", δ in eq. 4.2 and plot it as a function of the salt-to-surfactant concentration ratio in Fig. 4.9. The time, $t = 0.1s$ used in the definition of this parameter was chosen to be short enough to capture the maximum modulus attained at the applied strain. The time is also about a decade longer than the time for the motor to apply the strain, thus avoiding errors due to motor-induced stress overshoots or ringing.

$$Extent\ of\ hardening,\ \delta = \frac{G(\gamma = 3.5, t = 0.1s)}{G(\gamma = linear, t = 0.1s)} \tag{4.2}$$

Figure 4.9 shows the dependence of the extent of hardening on salt-to-surfactant concentration ratio.

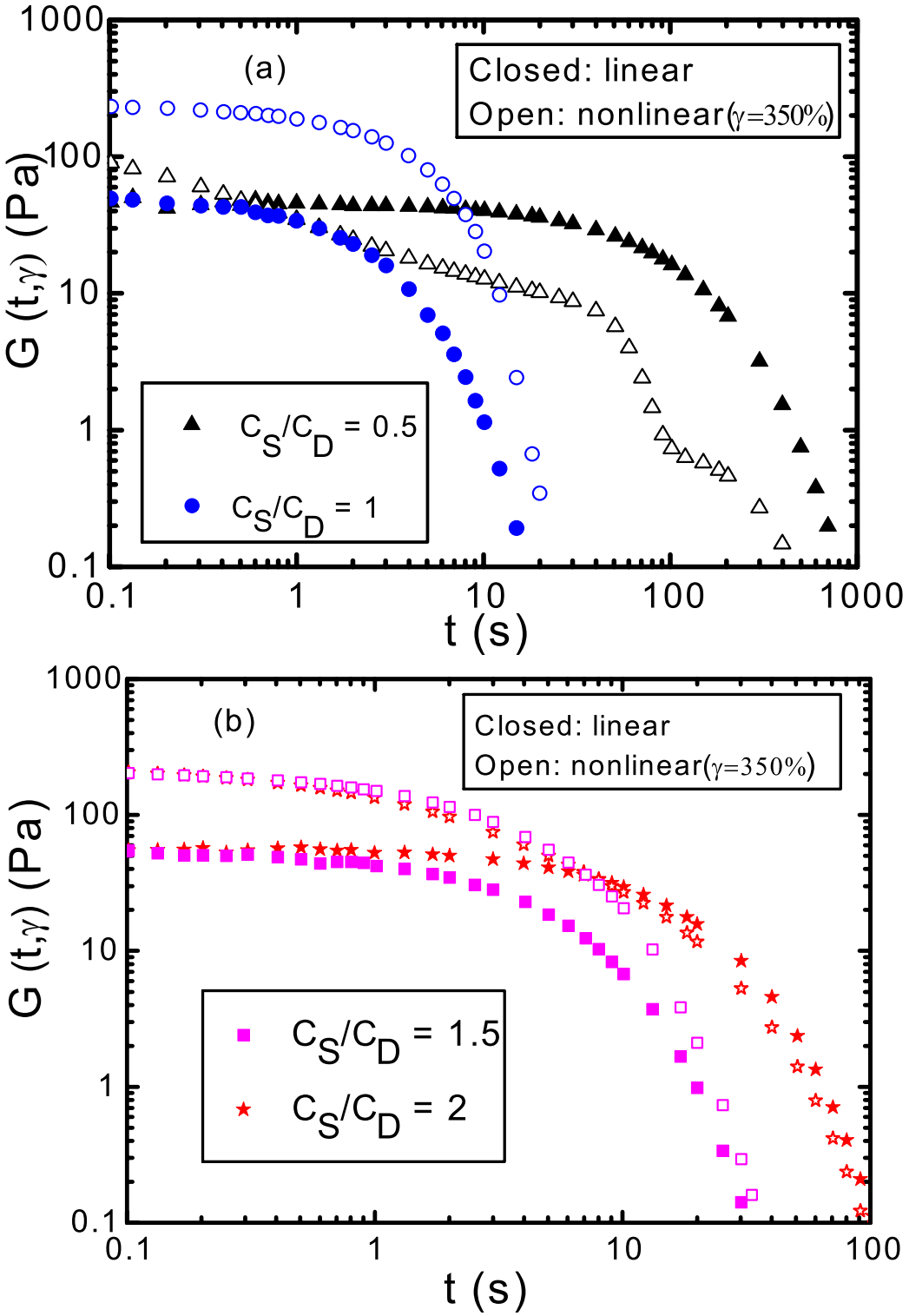

Figure 4.8: Stress relaxation after strains of 20 % (closed symbols) and 350 % (open symbols) for CTAB/NaSal solutions at (A) $C_S/C_D = 0.5$ and 1.0 and (B) $C_S/C_D = 1.5$ and 2.0. Measurements were taken at 20 °C.

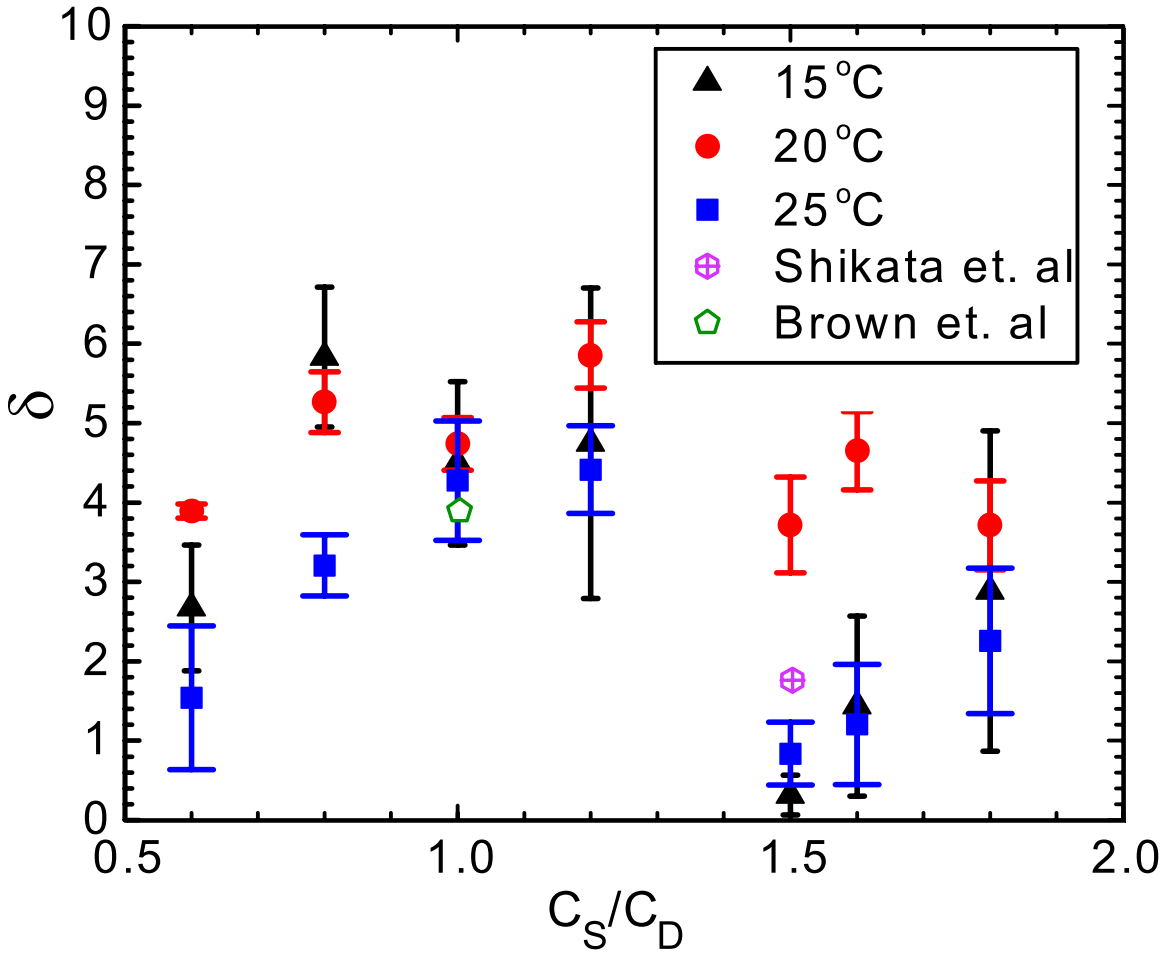

Figure 4.9: Strain hardening parameter as a function of salt-to-surfactant concentration ratio for CTAB/NaSal wormlike micelle solutions at three temperatures. Also shown are individual data points for identical solutions calculated from the data of Shikata et al.[14] (δ evaluated at $\gamma = 3.6$ and 1 s) and $T \approx 10 - 15\ ^0C$ and Brown et al.[15] at $\gamma = 3.5$ and an unspecified temperature. The error bars represent the standard error of the mean for repeated experiments on independently mixed solutions. The number of mixes represented in each error bar is given in the caption of Fig. 4.3a. The $C_S/C_D = 0.6$ 20 °C datapoint has an error bar which is very small thus inconspicuous.

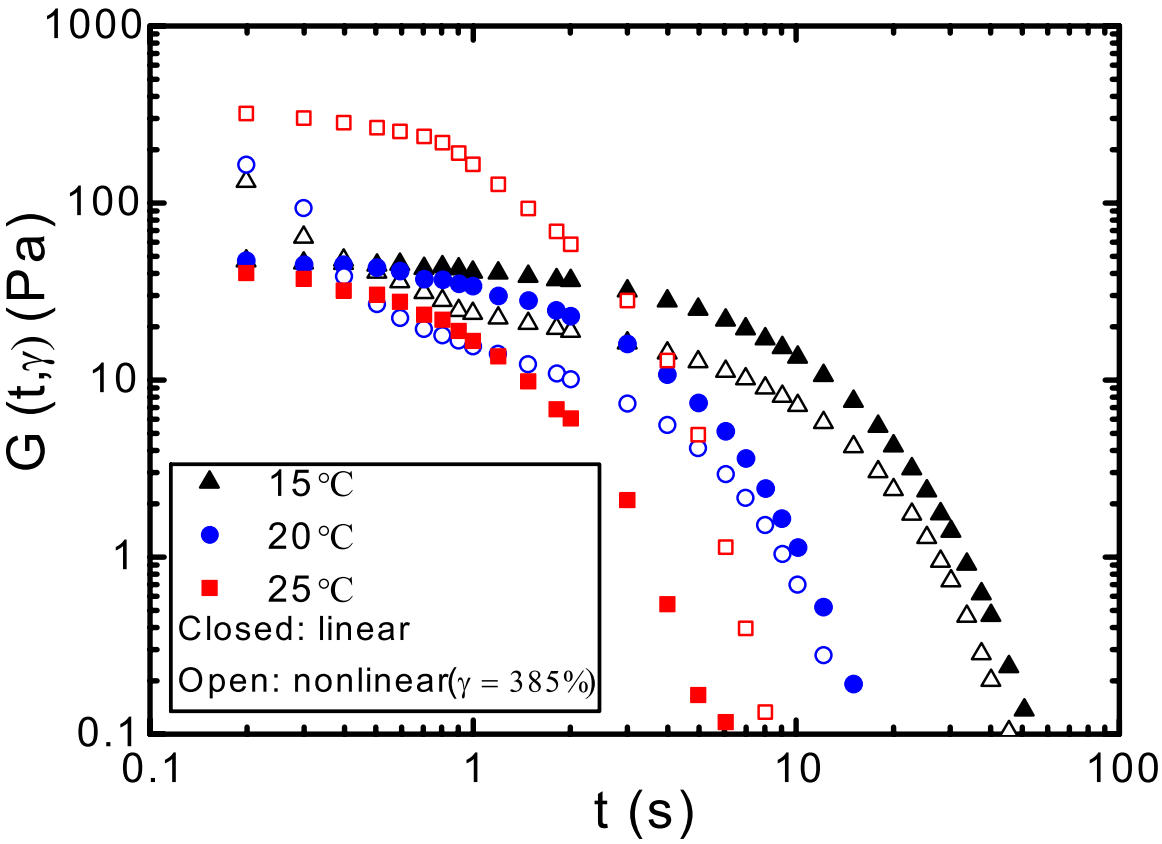

Figure 4.10: Stress relaxation after a step-strain of 385 % for CTAB/NaSal solution with salt-to-surfactant ratio of unity at 15, 20 and 25 °C.

4.3.2.2 Temperature Dependence

The relaxation of the wormlike micelles (at fixed salt concentration) varies with temperature upon nonlinear deformation. Generally, the relaxation time increased as the temperature decreased. Notably, the strain hardening at 385 % strain for the CTAB/NaSal at $C_S/C_D = 1.0$ and 25 °C is lost to a collapse of the relaxation modulus and transition to strain softening at about 0.4 s at 15 and 20 °C as shown in Fig. 4.10. This shows that temperature is an important parameter controlling strain hardening and that the temperature dependence of strain hardening is complex.

4.4 Discussion

Chain retraction and reptation have been described as the dominant mechanism of stress relaxation in some polymers [30]. These relaxation modes coupled with reversible scission have been used to explain the relaxation mechanism in wormlike micelles [9]. In this work, we observed strain hardening across a range of wormlike micelle solutions. The zero-shear viscosities varied non-monotonically with hydrotrope concentration as shown in Fig. 4.3a. The undulations observed in these properties suggest that changes in the equilibrium structure of these wormlike micelle solutions occur with increasing hydrotrope concentration. We therefore anticipate that additional relaxation processes might occur in the wormlike micelles upon nonlinear deformation. Our results significantly extend the earlier results of Shikata et al. [14] and of Brown et al. [15]. In particular, we comprehensively measured the effect of hydrotrope-to-surfactant concentration ratio and determined the temperature dependence of the transition from strain hardening to linear, and strain softening in CTAB/NaSal solutions. Despite having similar zero-shear viscosities, the wormlike micelle solution with added hydrotrope (CTAB/NaSal solution at $C_S/C_D = 1.2$) exhibited strain hardening while that with a simple salt (SLES/SLS with 3.5 wt% NaCl) did not show strain hardening behavior across the same range of applied strains. We also observed strain hardening in 60 mM CTAB / 30 mM SHNC wormlike micelles. This indicates that strain hardening is most likely to occur in wormlike micelles with hydrotropes.

The strain hardening observed could be due to alignment and packing of the erstwhile isotropic wormlike micelle network into bundles at high strain which would tend to fortify their strength and allow them to bear moderate nonlinear strains up to around 350%. Similar behavior has been observed in naturally occurring semiflexible polymer networks like filamentous actin (F-actin) in the presence of actin-binding protein (ABP) sucrin [31]. The F-actin/sucrin networks have comparable

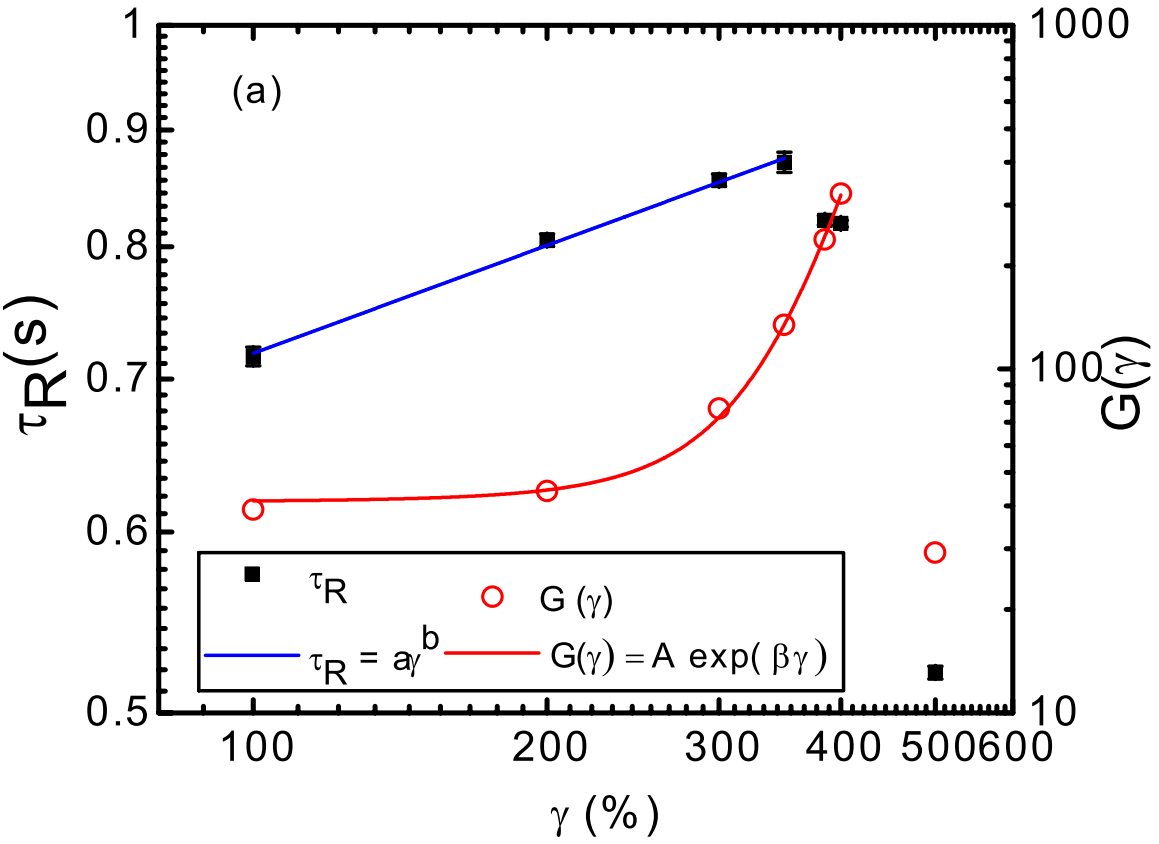

Figure 4.11: Relaxation time obtained from single decay exponential fits of the terminal region of nonlinear relaxation curves (closed squares) and relaxation modulus at $t = 0.1s$ (open circles) as functions of the applied strain for CTAB/NaSal solution at $C_S/C_D = 1.1$ at 25 °C. The relaxation time is fit by a power law with exponent b = 0.16 and the modulus was fit by an exponential function with growth constant $\beta = 0.02$, as indicated in the legend. The relaxation time decreases and does not fit the trend at strains of 385 - 500 % while the relaxation modulus collapse dramatically at 500 % strain.

sizes and flexibility[32] to giant micelles. The plateau modulus of F-actin/sucrin solutions increases with increasing strain much like the shear modulus at early times for CTAB/NaSal solution shown in Fig. 4.11. Gardel *et al.* showed that the sucrin simultaneously cross-links and bundles the actin filaments by connecting to them at regular intervals thus arranging the actin filaments in parallel conformations to one another. They exhibit over a decade increase in effective elasticity, thus strain hardening at constant nonlinear strain [31]. The strain hardening was reportedly lost at lower concentration of sucrin or F-actin similar to strain hardening lost in the case of CTAB/NaSal at low hydrotrope concentration.

The mechanism of strain hardening in semi-flexible polymer networks is not totally resolved. However, it has been attributed to tension generated in the network bundles due to nonlinear stretching of filaments, increase in mechanical cross-linking and bending rigidity of the bundles [31]. Cardiel *et al.* observed the formation of flow-induced structured phases containing entangled, branched and multi-connected bundles when solutions of CTAB/NaSal were subjected to high strains and strain rates by flowing them through micro-channels containing an array of micro-posts [12]. The existence of temporary sticky crosslinks acting as long-lived entanglements in the micelle network has in fact been suggested as an explanation of strain hardening in start-up shear flows of CTAB/NaSal solutions [16].

The nonlinear relaxation curves show a typical terminal relaxation time which was fit to a single exponential. At early times during the relaxation, some curves could not be fit by a single exponential. An exponential with two or three decay constants would need to be used to obtain a good fit depending on how quickly the modulus relaxed. This was common in the region of low hydrotrope concentration where the relaxation was prolonged with noticeable variation in decay rates of the modulus (see Fig. 4.6b). Under step stains, the micelles could form strain-induced structures transiently in short time through bundling of micelles or where shorter

micelles or free hydrotropes could form cross-links between micelles, which are not readily broken by moderate strains and persists for an extended period of time relative to an entanglement. These physical crosslinks would enhance the rigidity and overall elasticity of the wormlike micelle bundle and hence, the transient micellar network.

Following this argument, we postulate that the strain hardening occurs due to the dynamics of micelle bundles formed during flow. Sudden application of a large deformation on the micelle networks would lead to build-up of stresses in the wormlike micelle bundles especially at the interconnecting bridges (physical crosslinks) which have reduced degrees of freedom and therefore cannot instantaneously relax the stress. We anticipate relaxation modes of the wormlike micelle bundles that differ from those for individual unbundled micelles. There is a possibility of bending and twisting of the micelle bundles thereby causing internal sliding of bridges in the bundles. In addition to the established reversible scission and reptation, other relaxation processes present for bundles may include relaxation of stresses in the bridges, unbinding of the bridges and fracture of the bundles , as described by Broedersz and Mackintosh for bundles of actin filaments [32]. Some of the relaxation modes could potentially occur within similar timescales and compete to be the dominant mechanism of relaxation or occur in different timescales. The wormlike bundle model of Broedersz and Mackintosh takes into account competing deformation mechanisms by employing a parameter that describes the relative importance between the crosslink shearing and filament stretching [32]. The fracture of the wormlike micelle bundles could be responsible for the abrupt and pronounced reduction of the shear modulus. This could occur due to simultaneous rupture of many crosslinkers due to the accumulated tension surpassing their stiffness. The disintegration of the micelle bundles would free individual wormlike micelles to continue their relaxation.

Figure 4.8 shows three different regimes for the effect of hydrotrope-to-surfactant ratio on stress relaxation at a moderate nonlinear strain of 350 % and 20 °C. The

first regime ($C_S/C_D < 1$) is characterized by an initial strain hardening where the modulus is quickly relaxed in less than about 1 s to strain softening with a multi-stage relaxation of stress. The second regime ($1 \leqslant C_S/C_D \leqslant 1.6$) exhibits a consistent strain hardening. The third regime ($C_S/C_D > 1.6$) shows a prolonged strain hardening that reduces in about 10 s to strain softening with a single-stage relaxation. We hypothesize that the differences in the regimes may be explained by the stiffness of the transient structures formed and their relaxation times and mechanisms. A potential explanation for the strain hardening behavior of Regime I wormlike micelles is that micelle bundles of moderate stiffness are formed transiently leading to the initial hardening. Many of these bundles could then rupture as their strength is overcome by the strain applied. This rupture would lead to a sudden decrease in modulus and relaxation of the stress which dominates the first stage of relaxation. The latter stages of the relaxation would then be a combination of further unbundling and internal relaxation of the stresses in the micelle bundles and reversible scission and reptation of unbundled micelles, which we expect to dominate the final stage of the multi-stage relaxation. In Regime II, we propose that the transient strain-induced structures formed have greater stiffness than Regime I micelles and withstand the moderate strains of 350 % consistently through the relaxation. We anticipate that the internal bundle relaxations, unbundling, reversible scission and reptation occur in similar timescales and would compete for dominance of the stress relaxation process. The Regime III micelles on the other hand, we propose would form strain-induced structures of intermediate rigidity with a hybrid (of Regimes I and II) relaxation. The Regime III structures soften like those of Regime I at relatively longer times but the relaxation processes are much like that of Regime II. We remain uncertain what controls the rigidity and strength of these strain-induced structures.

The excess salt concentration defined by Shikata et al. [14] as the concentration of free hydrotropes not bound in the surfactant-hydrotrope complex was investigated

as a correlating variable for the strain hardening behavior. We found that the excess salt concentration - which was calculated as the difference in salt and surfactant concentration- did not better correlate the results. We noted previously in **??** that different relaxation behaviors were observed for CTAB/SHNC wormlike micelles at the same salt-to-surfactant ratio. Similarly, the results reported in Fig. 4.7b and Fig. 4.7c have nearly identical excess salt concentration of $-0.05\,mol/dm^3$ but also show remarkable difference in stress relaxation behaviors. Figure 4.7 illustrates that qualitatively similar relaxation processes of strain hardening, abrupt softening with multistage relaxation and softening with single relaxation are observed in CTAB/SHNC wormlike micelles akin to those of CTAB/NaSal. However, the kind of hydrotrope used could have different effect on the strain hardening and relaxation behavior for a particular salt-to-surfactant concentration ratio and this is a potential area of interest for future work.

As strain is initially increased, the terminal relaxation time is observed to increase progressively as shown in Fig. 4.11. Following a power law growth with $\tau_R \approx \gamma^{0.16}$. The initial shear modulus attained at the applied strain before significant relaxation of stress, which is the extent of strain hardening varies with strain by the relationship $G(\gamma) \approx exp(\beta\gamma)$ where $\beta = 0.02$ for $C_S/C_D = 1.1$. Hence, the micelle network stiffness increases exponentially with increasing nonlinear strain until a critical strain of about 400% at which the bundle strength is overcome leading to strain softening. This transition from strain hardening to softening can occur abruptly in time, as observed under some conditions in our experiments. The strain and time at which the 'collapse' of the hardening relaxation curve occurs varies with the salt-to-surfactant concentration ratio, C_S/C_D and temperature. This could be as a result of the changes in the morphology of the micelles formed as the concentration of hydrotrope is varied ultimately altering the dynamics of the micelles under shear flow. Changes in hydrotrope concentration have been reported to change micelle flexibility, stiffness and

size [33, 34, 2, 5].

We therefore propose that the hardening is the result of the stiffness and length of the micelles, size and the density of entanglements coupled with the availability of sufficient free (unbound) hydrotropes in solution that can easily act as crosslinkers to align and bundle the wormlike micelles into formidable transient network structures under flow. We observed that the transition from strain hardening to strain softening occurs between 300-400 % strain for most of the CTAB/NaSal solutions. Interestingly, at $C_S/C_D = 1$ and $\gamma = 385\%$, we observe in Fig. 4.10 a time dependent transition from hardening to softening, with the modulus crossing the linear response at 0.3 s, at 15 and 20 °C. However, at 25 °C, the solution remains strain hardening at all times at this higher temperature. However, we could not establish a simple relationship between the extent of strain hardening and either concentration or temperature.

It is noteworthy that we observed a striking correlation between the extent of hardening and the linear plateau modulus for a set of CTAB/NaSal wormlike micelles of different hydrotrope-to-surfactant concentration ratios. However, the correlation was largely lost when averaged over different independent mixes of wormlike micelle solutions at the same hydrotrope-to-surfactant concentration ratio. Figure 4.12 shows the averaged plateau modulus and extent of hardening as functions of the hydrotrope-to-surfactant concentration ratio for independently re-mixed samples of the wormlike micelle solutions. The error bars which represent the standard error of the means were significant. The large error bars in the plateau modulus in Fig. 4.12 could be as a result of the sensitivity to sample preparation, despite the care we have taken. Error bars of relatively similar magnitude of were also obtained for the zero-shear viscosity shown in Fig. 4.3 but they are less conspicuous, because they are plotted on a log scale, as is common in the field. This limit to reproducibility is not unique to our work. Calabrese et al. [35] also noted that it could be extremely difficult to replicate precisely some parameters from different sample preparations

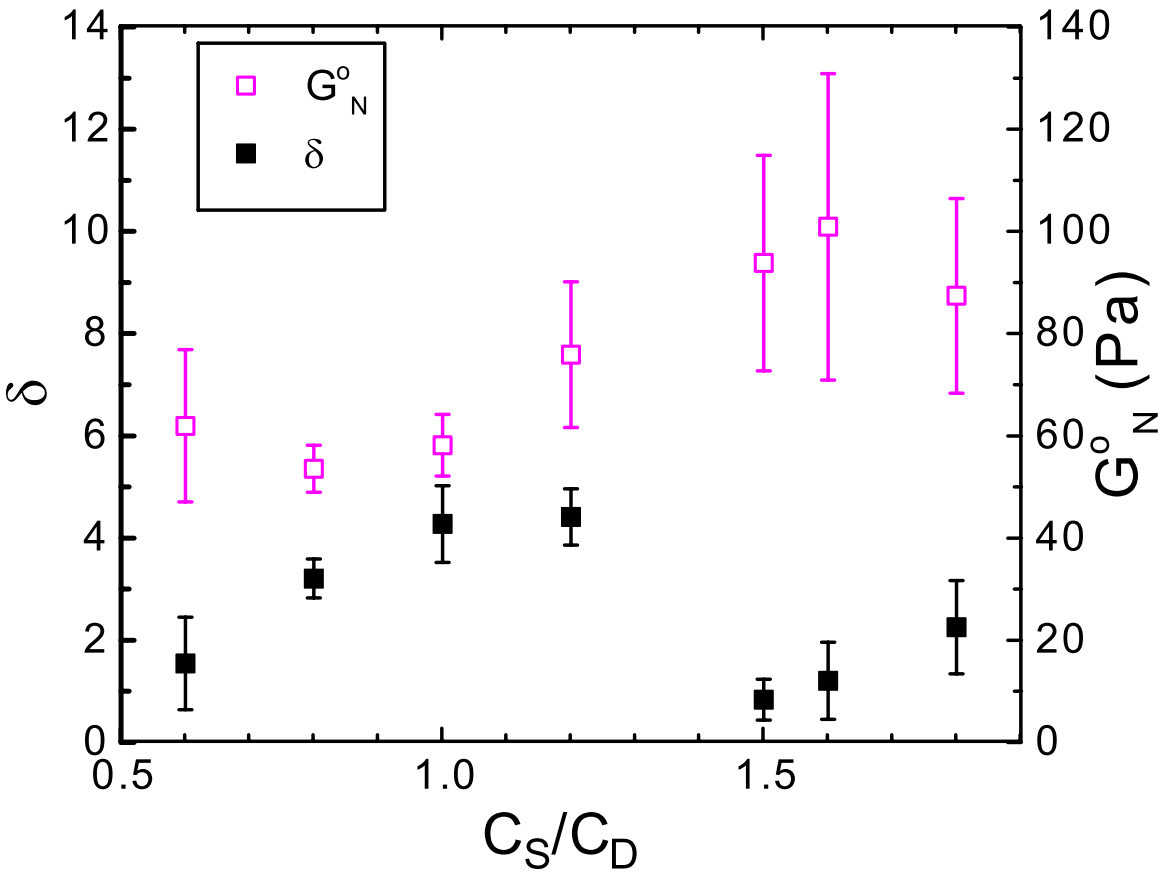

Figure 4.12: Plateau modulus, G_0 and extent of hardening, δ (defined in text) at 25 °C as functions of the ratio of concentration of NaSal to CTAB. The error bars represent the standard error of the mean of the plateau modulus and extent of hardening for different re-mixes. The number of samples represented in each error bar is given in the caption to Fig. 4.3a.

of wormlike micelles such as cross-over modulus and zero-shear viscosity in their study. The strain hardening in CTAB/NaSal wormlike micelles showed a general increase in the extent of hardening with increasing hydrotrope concentration up to about equimolar concentration of hydrotrope and surfactant, followed by a drop to a near-linear response at $C_S/C_D = 1.5$ and a meager increase afterwards. This trend was consistent between the remixed wormlike micelle solutions. To go beyond these observations regarding the sources of strain hardening and its collapse, the structure of the micelle solution under conditions of non-linear deformation will need to probed by techniques such as neutron or x-ray scattering.

4.5 Summary

We performed step-strain experiments on both anionic wormlike micellar solutions with a simple salt (NaCl) and cationic wormlike micelle solutions with added hydrotropic salt (NaSal and SHNC) and observed strain hardening only with the hydrotropic salts. The CTAB/NaSal wormlike micelles exhibited strain hardening over the range, $C_S/C_D = 0.5 - 3.0$. Limited studies of the CTAB/SHNC wormlike micelles showed strain hardening for 60 mM CTAB / 30 mM SHNC which transitioned to strain softening in time at 25 °C. We observed a temperature dependence of both strain hardening and of the transition in the stress relaxation curves from strain hardening to strain softening or linear response. The critical strain and time at which this transition occurs varies with concentration and temperature. The complex dependence of strain hardening on salt concentration, temperature, strain, and time that we observe remain to be explained. We postulate that the formation of strain-induced structures such as micelle bundles, with hydrotropes possibly bridging micelles together, are responsible for strain hardening, the anomalous transition to softening and the complex dependencies of strain hardening on the above variables in these wormlike micelles. Presumably structural probes that are complementary to rheology, such as time-resolved neutron scattering, will be required to provide a convincing explanation for these phenomena, which are likely related to shear thickening, shear-induced structures, and other phenomena in worm-like micellar solutions.

Bibliography

[1] D. P. Acharya and H. Kunieda, Advances in colloid and interface science **123-126**, 401 (2006).

[2] L. J. Magid, The Journal of Physical Chemistry B **102**, 4064 (1998).

[3] S. Ezrahi, E. Tuval, and a. Aserin, Advances in colloid and interface science **128-130**, 77 (2006).

[4] J. F. Berret, in *Molecular Gels: Materials with Self-Assembled Fibrillar Networks*, edited by R. Weiss and P. Terech (Springer Netherlands, 2006) pp. 667–720.

[5] R. Abdel-Rahem, Advances in colloid and interface science **141**, 24 (2008).

[6] M. E. Cates and S. M. Fielding, Advances in Physics **55**, 799 (2006), arXiv:0702047 [cond-mat] .

[7] M. F. Torres, J. M. González, M. R. Rojas, A. J. Müller, a. E. Sáez, D. Löf, and K. Schillén, Journal of colloid and interface science **307**, 221 (2007).

[8] M. E. Cates, Macromolecules **20**, 2289 (1987).

[9] M. E. Cates and S. J. Candau, Journal of Physics: Condensed Matter **2**, 6869 (1990).

[10] P. D. Olmsted, Rheologica Acta **47**, 283 (2008).

[11] J. K. G. Dhont and W. J. Briels, Rheologica Acta **47**, 257 (2008).

[12] J. J. Cardiel, A. C. Dohnalkova, N. Dubash, Y. Zhao, P. Cheung, and A. Q. Shen, Proceedings of the National Academy of Sciences of the United States of America **110**, E1653 (2013).

[13] J.-F. Berret, D. C. Roux, and G. Porte, Journal de Physique II **4**, 1261 (1994).

[14] T. Shikata, H. Hirata, E. Takatori, and K. Osaki, Journal of Non-Newtonian Fluid Mechanics **28**, 171 (1988).

[15] E. Brown, W. Burghardt, and D. Venerus, Langmuir **7463**, 3902 (1997).

[16] T. Inoue, Y. Inoue, and H. Watanabe, Langmuir : the ACS journal of surfaces and colloids **21**, 1201 (2005).

[17] M. Takeda, T. Kusano, T. Matsunaga, H. Endo, M. Shibayama, and T. Shikata, Langmuir **27**, 1731 (2011).

[18] R. Larson, *Constitutive equations for polymer melts and solutions* (Butterworth Publishers, 1988).

[19] K. Nakamura and T. Shikata, Nihon Reoroji Gakkaishi **36**, 167 (2008).

[20] K. Nakamura, S. Takase, and T. Shikata, Nihon Reoroji Gakkaishi **38**, 31 (2010).

[21] T. Shikata, H. Hirata, and T. Kotaka, Langmuir **3**, 1081 (1987).

[22] Y. Zhao, S. J. Haward, and A. Q. Shen, Journal of Rheology **59**, 1229 (2015).

[23] K. Penfield, A. Co, G. L. Leal, R. H. Colby, and A. J. Giacomin, AIP Conference Proceedings **1027**, 899 (2008).

[24] H. Rehage and H. Hoffmann, Molecular Physics **74**, 933 (1991).

[25] E. Kaler and F. Nettesheim, in *Giant Micelles*, Surfactant Science (CRC Press, 2007) pp. 223–247.

[26] X. Tang, W. Zou, P. H. Koenig, S. D. McConaughy, M. R. Weaver, D. M. Eike, M. J. Schmidt, and R. G. Larson, The Journal of Physical Chemistry B **121**, acs.jpcb.7b00257 (2017).

[27] Y. Kim, A. Adams, W. H. Hartt, R. G. Larson, and M. J. Solomon, Journal of Non-Newtonian Fluid Mechanics **232**, 77 (2016).

[28] W. Zou, X. Tang, M. Weaver, P. Koenig, and R. G. Larson, Journal of Rheology **59**, 903 (2015).

[29] T. Holz, P. Fischer, and H. Rehage, Journal of Non-Newtonian Fluid Mechanics **88**, 133 (1999).

[30] Y.-H. Lin, *Polymer Viscoelasticity*, 2nd ed. (World Scientific Publishing Co. Pte. Ltd., Singapore, 2010) p. 441.

[31] M. L. Gardel, J. H. Shin, F. C. MacKintosh, L. Mahadevan, P. Matsudaira, and D. A. Weitz, Science **304**, 1301 (2004).

[32] C. P. Broedersz and F. C. Mackintosh, Reviews of Modern Physics **86**, 995 (2014), arXiv:1404.4332 .

[33] C. A. Dreiss, Soft Matter **3**, 956 (2007).

[34] S. Amin, T. W. Kermis, R. M. van Zanten, S. J. Dees, J. H. van Zanten, R. Zanten, S. J. Dees, and J. Zanten, Langmuir **17**, 8055 (2001).

[35] M. a. Calabrese, S. a. Rogers, R. P. Murphy, and N. J. Wagner, Journal of Rheology **59**, 1299 (2015).

CHAPTER V

Conclusion and Future Work

5.1 Conclusion

In this thesis, we investigated the nonlinear rheological behavior of wormlike micelles over different concentration regimes using Brownian dynamics (BD) simulations, theoretical development of constitutive equations and step-strain experiments on a rheometer. These methods provided us better insights into the role of reversible scission and entanglements in the transient shear stress response in dilute and semi-dilute wormlike micelles, and strain hardening in wormlike micelles over a wide concentration range.

In Chapter II, we demonstrated that the implementation of reversible scission of micelles required a more detailed multi-bead-spring model with sufficient internal degrees of freedom that track the dynamics of the interacting chain segments. We showed the inadequacy of representing both species of interacting wormlike micelles as dumbbells, as in the Vasquez-Cook-McKinley (VCM) model by replicating the formulation of their problem in an analogous BD simulations. We observed an over-prediction of the transient stress of short micelle species by the VCM model in comparison to parallel BD predictions. We observe the source of this discrepancy to be the loss of configurational information of the relative short micelle segments in the long species when the long species are treated as dumbbells. Therefore, the micelle

reaction kinetic involving fusion of short dumbbells to longer dumbbells lack the required internal degrees of freedom needed to accurately describe reversible scission in wormlike micelles. We fix this by implementing long species micelles as multiple bead-spring chains that break in the middle to give shorter micelles each of equal length. We therefore track all internal chain segments and accurately describe the exchange of species during the scission and recombination events.

We then employed the differential equations for end-to-end vector dyads of Wiest, Wedgewood, and Bird [1] to develop a constitutive equation that tracks the internal configurations of the wormlike micelles during reversible scission. The constitutive equation can describe chains with Hookean springs exactly, as shown by comparison with Brownian dynamics simulations of the same two-species model, and could account approximately for non-linear chains for example, using finitely extensible nonlinear elastic (FENE) chains with appropriate closure approximations.

In Chapter III, we advance the wormlike micelle reversible scission simulation of Chapter II to include the effect of topological entanglements present at semi-dilute micelle concentrations. We formulated the novel model for simulating entangled wormlike micelles by incorporating reversible scission in an established slip-link model. We studied the effects of reversible scission vis-a-vis entanglements on the rheology of wormlike micelles. We find that entanglements increase steady stress and produced a stress overshoot in polymers with sufficient entanglements (about one entanglement per four beads). However, in entangled wormlike micelles, reversible scission on the order of Rouse time led to higher steady stress, for same conditions as in polymers, without the occurrence of the stress overshoot. Reversible scission in the fast-breaking regime, where breakage times are much more faster than reptation is needed for the stress relaxation effects to be significant. Increased scission rates led to a corresponding decrease in steady stress which produced a stress overshoot.

In Chapter IV, we performed step-strain experiments on both anionic wormlike

micellar solutions with a simple salt (NaCl) and cationic wormlike micelle solutions with added hydrotropic salt (NaSal and SHNC). We observed strain hardening only in wormlike micelles that contained hydrotropes. The CTAB/NaSal wormlike micelles exhibited strain hardening over the range, $C_S/C_D = 0.5 - 3.0$. We performed limited studies of the CTAB/SHNC wormlike micelles; they revealed a strain hardening transition to strain softening for 60 mM CTAB / 30 mM SHNC at 25 °C. We observed a temperature dependence of both strain hardening and of the transition in the stress relaxation curves from strain hardening to strain softening or linear response. The critical strain and time at which this transition occurs varied with concentration and temperature.

The complex dependence of strain hardening on salt concentration, temperature, strain, and time that we observe remain to be explained. We postulate that the formation of strain-induced structures such as micelle bundles, with hydrotropes possibly bridging micelles together, are responsible for strain hardening, the anomalous transition to softening and the complex dependencies of strain hardening on the above variables in these wormlike micelles. We note that employing complementary experiments that can probe the structure of micelles such as time-resolved neutron scattering, might be able to provide a convincing explanation for these phenomena, which are likely related to shear thickening, shear-induced structures, and other phenomena in worm-like micellar solutions.

5.2 Future Work

5.2.1 Advances on Modeling and Simulation of Worm-like Micelles

The constitutive equations developed in Chapter II could be used to explore calculations with FENE spring, and with multiple-species models. It should also be possible to include scission and fusion rates that depend on average stress and orien-

tation of the micelles. The study could also be extended to other equilibrium micelle kinetics such as end and bond interchange and structural features such as rings and micelle branches.

5.2.2 Dynamics and rheology of microstructure for strain hardening wormlike micelles

5.2.2.1 Background

In our previous studies reported herein, we observed strain hardening in cationic systems of CTAB/NaSal in water between a salt to surfactant concentration ratio, C_S/C_D of 0.5-2.0. The magnitude of strain hardening (Eq. (4.2)) however did not have a simple relationship with salt concentration. Our results defies the conclusion in literature of [2] that strain hardening occurred in cationic wormlike micelle systems with low concentration of free (unassociated) hydrotrope ions, C_S^*. We observed higher magnitudes of strain hardening at C_S^* values lower and higher than $C_S/C_D = 1.5$ corresponding to $C_S^* = 0.5$. We observed an anomalous transition in the stress relaxation curves from strain hardening to strain softening or linear response. The critical strain and time at which this transition occurred varied with concentration and temperature. This anomalous transition was observed to be temperature dependent, occurring at a strain of 3.85 and a low temperature of 15 ^0C but hardening at 25 ^0C for the same strain and salt and surfactant concentrations. This could be a promising tool for switching between a strain hardening and softening behavior and vice versa for the same wormlike micelle in potential applications. It is therefore necessary to understand the mechanism of this strange phenomenon.

5.2.2.2 Scientific Importance

We seek to understand the mechanism of strain hardening in wormlike micelles by performing in-situ neutron scattering with rheology (Rheo-SANS). Wormlike micelles

are formed by the reversible self-assembly of amphiphilic molecules. The wormlike micelles aggregate to form viscoelastic networks. Hence, they are applied in oil recovery, drug delivery, drag reduction etc. [3]. This is due to their interesting nonlinear rheological properties particularly shear banding, shear thickening and strain hardening. Of these properties, strain hardening is the least understood. We studied [4] the conditions necessary for strain hardening in surfactant wormlike micelles including CTAB with added hydrotrope, NaSal. We observed a complex dependence of the extent of hardening to the hydrotrope-to-surfactant concentration ratio and temperature. We also observed an anomalous transition from strain hardening to softening or linear response, similar to that reported by Brown et al. [5]. In addition, we observed the transition depended on temperature. This transition has potential applications where strain hardening and softening behaviors were needed and temperature could be used as a switch between them. Unlike the Rheo-SALS (Rheology with Small Angle Light Scattering) which can track the dynamics of the micellar contour length, Rheo-SANS is particularly suited for tracking the dynamics of macromolecular chains and aggregates at a globular and individual (few Kuhn lengths) scale in-situ as the shear is been applied to them. Takeda et al. [6] used Rheo-SANS to observe transitions in the morphology of CTAB/NapTS micelles from short to long wormlike micelles then to long micelles with entanglements corresponding to Newtonian to shear thickening then shear thinning behavior. We observed a correlation of the extent of hardening and the linear plateau modulus, an equilibrium and linear property of the wormlike micelles, which relates to the number density of entanglements. We therefore hypothesize that strain-hardening phenomenon is connected to the existence and dynamics of the entanglements, perhaps the interconnection of entangled micelles to form wormlike micelle bundles. However, the factual explanation of the mechanism of strain hardening is still elusive.

5.2.2.3 Preliminary Work

The conditions under which wormlike micelle solutions of CTAB and NaSal exhibit strain hardening have been examined by performing step strain measurements on a rheometer. We observed complex relationships between the extent of strain hardening - defined as the ratio of nonlinear to linear relaxation modulus at short times (0.1 s) - and both concentration and temperature. The ALV CGS-3 dynamics light scattering instrument with a compact goniometer system and a laser of wavelength 632.8 nm could be used to obtain equilibrium properties of the wormlike micelles. Using this, relaxation times, mesh size and size distributions of the wormlike micelles in equilibrium are obtained by varying the scattering angle gradually between 0 and 90 °. These equilibrium properties can be obtained from the translation diffusion coefficient as the slope of a plot of relaxation rate and scattering vector, q2 [7, 8]. The wormlike micelle size is determined by solving iteratively the Yamakawa-Fujii equation which models the wormlike micelles as a worm-like cylinder [9]. Using an Anton-Paar MCR 702 rheometer with a SALS option, and circular Couette and parallel plate geometries, the contour length dynamics of the wormlike micelles during nonlinear step strains (where strain hardening occurs) can be probed.

5.2.2.4 Choice of Instrument

To carry out the in-situ neutron scattering and rheological studies of the wormlike micelles, the use of the general SANS (GP-SANS CG-2) instrument at HFIR because of the high intensity neutron flux is required. Secondly, the two-meter (2 m) sample environment is spacious enough to allow for an MCR 301 rheometer to sit along the beam line. The services of the Biophysical characterization laboratory could be requested to prepare deuterated NaSal hydrotropes from perdeuterated salicylic acid. The NaSal hydrotropes tend to aggregate around entanglements. The contrast observed would be used as a means of observing the structural changes in

the entanglement and their dynamics.

5.2.2.5 Experiment Plan

The samples are four different hydrotrope-to-surfactant concentration ratios (0.6, 1.0, 1.5 and 1.8) of the CTAB/NaSal wormlike micelles. For each of the concentration ratios, prepare a batch with the surfactant and hydrotrope dissolved in D_2O with 99.9% purity. The second batch of sample would be prepared with CTAB and perdeuterated NaSal in water. The perdeuterated salicylic acid would be reacted with sodium hydroxide to get the perdeuterated sodium salt of the acid, NaSal. The samples would be allowed to equilibrate for 2 days. Rheology measurements with in-situ neutron scattering in the velocity gradient-vorticity plane could be run using Titanium based Couette shear cells for all samples. Experiments at equilibrium (no flow) would be used as a control in comparison to the scattering data with flow. Each of the runs should take an hour to complete. For each of the samples, perform a linear step strain measurement at 10 % strain and nonlinear strains for (350, 385 and 500 % strains). Each of these would take an hour to complete. Then run a set of step strain experiments for the sodium lauryl ether (1) sulfate (SLE1S)/ NaCl wormlike micelle solution that was observed [4] not to exhibit strain hardening as a control for the experiments. These experiments would be run at 25 °C. Step strain experiments at hydrotrope-to-surfactant concentration ratio of 1, strains of 10 and 385 % at 20 °C would be performed to investigate the hardening-softening transition. The q-range for the experiments are 0.005 - 0.3 $^{-1}$. It should require about 4 days to run these experiments on the CG-2 GP-SANS instrument at HFIR, Oak Ridge National Laboratory. The rheological data generated should be collected on the Anton-Paar RheoCompass software. The neutron scattering intensities would be detected on a square meter detector and the data collected on the Mantidplot software and used in generating 2-D SANS patterns. The 2-D scattering pattern should then be ana-

lyzed using SASview (http://www.sasview.org/). The data would be reduced to a 1-D scattering intensity vs q plot [10] and fit to theoretical models that model the structures as wormlike cylinders [11] and take account of micelle flexibility [12, 13].

5.2.2.6 Spatial and Temporal Resolution of Microstructure and Stress

The orientation of the wormlike micelles can be tracked from the SANS measurements using the alignment factor, Eq. (5.1) which is an order parameter that quantifies the flow-induced alignment of the micelles. Alignment factor values range between 0 and 1. A value of zero represents isotropic configuration of the wormlike micelles while a value of 1 represent full alignment in the direction of flow. A nematic fluid has a typical alignment factor of about 0.7 [14].

$$\left|A_f\right| \ (q^*) = \frac{\int_0^{2\pi} I(q^*, \phi) \cos 2(\phi - \phi_0)] d\phi}{\int_0^{2\pi} I(q^*) d\phi} \tag{5.1}$$

where q is the scattering angle, ϕ is the azimuthal angle with respect to the direction of flow, ϕ_0 is the segmental orientation given by the minimum in $I(q^*, \phi)$ which is the annular average scattering intensity consequently averaged over q range corresponding to the segmental length of the wormlike micelles [15]. The principle axis of scattering, ϕ_0 defines the microstructure[14]. The stress relaxation curve is to be estimated in time using the stress-SANS rule as given by Eq. (5.2).

$$\sigma_{12}^p = G_0 (C A_f)^{(1/2)} \sin(2\phi_0) \tag{5.2}$$

Similar method of obtaining derived parameters explained in equilibrium section above would be employed for step strain experiments. Helgeson [16] reported writing a computer program to fit their data with the Schurtenberger model [12, 17, 18].

5.2.2.7 Safety Considerations

The chemical formula of cetyl trimethylammonium bromide is [(C16H33)N(CH3)3]Br and that of sodium salicylate is C7D5NaO3 (salicylic acid C7D6O3). The chemical formula of sodium lauryl ether (1) sulfate (SLE1S) is $CH_3(CH_2)_{11}(OCH_2CH_2)_1OSO_3Na$. All samples to be tested on the GP-SANS are in solution state. The samples are in powdered form before preparation.

Bibliography

[1] J. M. Wiest, L. E. Wedgewood, and R. B. Bird, The Journal of Chemical Physics **90**, 587 (1989).

[2] T. Shikata, H. Hirata, E. Takatori, and K. Osaki, Journal of Non-Newtonian Fluid Mechanics **28**, 171 (1988).

[3] C. A. Dreiss, Soft Matter **3**, 956 (2007).

[4] A. A. Adams, M. J. Solomon, R. G. Larson, and X. Xia, Journal of Rheology **61**, 967 (2017).

[5] E. Brown, W. Burghardt, and D. Venerus, Langmuir **7463**, 3902 (1997).

[6] M. Takeda, T. Kusano, T. Matsunaga, H. Endo, M. Shibayama, and T. Shikata, Langmuir **27**, 1731 (2011).

[7] P. a. Hassan, S. R. Raghavan, and E. W. Kaler, Langmuir **18**, 2543 (2002).

[8] T. G. Movchan, I. V. Soboleva, E. V. Plotnikova, a. K. Shchekin, and a. I. Rusanov, Colloid Journal **74**, 239 (2012).

[9] W. Brown, *Dynamic light scattering: the method and some applications*, Monographs on the physics and chemistry of materials (Clarendon Press, 1993).

[10] A. P. R. Eberle and L. Porcar, Current Opinion in Colloid and Interface Science **17**, 33 (2012).

[11] V. Lutz-Bueno, J. Kohlbrecher, and P. Fischer, Rheologica Acta **52**, 297 (2013).

[12] J. Skov, P. Schurtenberger, and J. S. Pedersen, Macromolecules **9297**, 7602 (1996).

[13] C. Sommer, L. Cannavacciuolo, S. U. Egelhaaf, J. S. Pedersen, and P. Schurtenberger, Progress in Colloid and Polymer Science **115**, 347 (2000).

[14] a. K. Gurnon, C. R. Lopez-Barron, A. P. R. Eberle, L. Porcar, and N. J. Wagner, Soft Matter **10**, 2889 (2014).

[15] C. R. López-Barrón, a. K. Gurnon, A. P. R. Eberle, L. Porcar, and N. J. Wagner, Physical Review E - Statistical, Nonlinear, and Soft Matter Physics **89**, 042301 (2014).

[16] M. E. . Helgeson, *STRUCTURE , RHEOLOGY , AND THERMODYNAMICS OF WORMLIKE MICELLE-NANOPARTICLE MIXTURES by Matthew E . Helgeson A dissertation submitted to the Faculty of the University of Delaware in partial fulfillment of the requirements for the degree of Doctor of Philos*, Doctoral, University of Delaware (2009).

[17] J. S. Pedersen, L. Cannavacciuolo, and P. Schurtenberger, in *Giant Micelles*, Surfactant Science (CRC Press, 2007) pp. 179–222.

[18] M. Bergström, J. S. Pedersen, P. Schurtenberger, and S. Egelhaaf, The Journal of Physical Chemistry B **103**, 9888 (1999).

APPENDICES

APPENDIX A

Two-species Brownian dynamics (BD) Simulations of Wormlike Micelles using Springs with a Non-linear Force-Extension Relationship

A.1 Introduction

In order to predict many of the nonlinear rheological phenomena discussed in Section 1.3.2, nonlinear force-extension relationships, also referred to as "spring laws" are used to represent the entropic springs in multi-bead-spring Brownian dynamics simulations. The nonlinear spring laws ensures that the dynamics of the springs are closer to reality by permitting the springs to extend to a maximum extension (see Fig. A.1). This is unlike the Hookean springs whose extension (or chain stretch) vary linearly with applied force thereby allowing them to stretch infinitely. Hookean springs are suitable for linear rheology studies and low shear rate flows. Nonlinear spring laws are more suited to capture nonlinear flows where shear rates are high and deformation is huge.

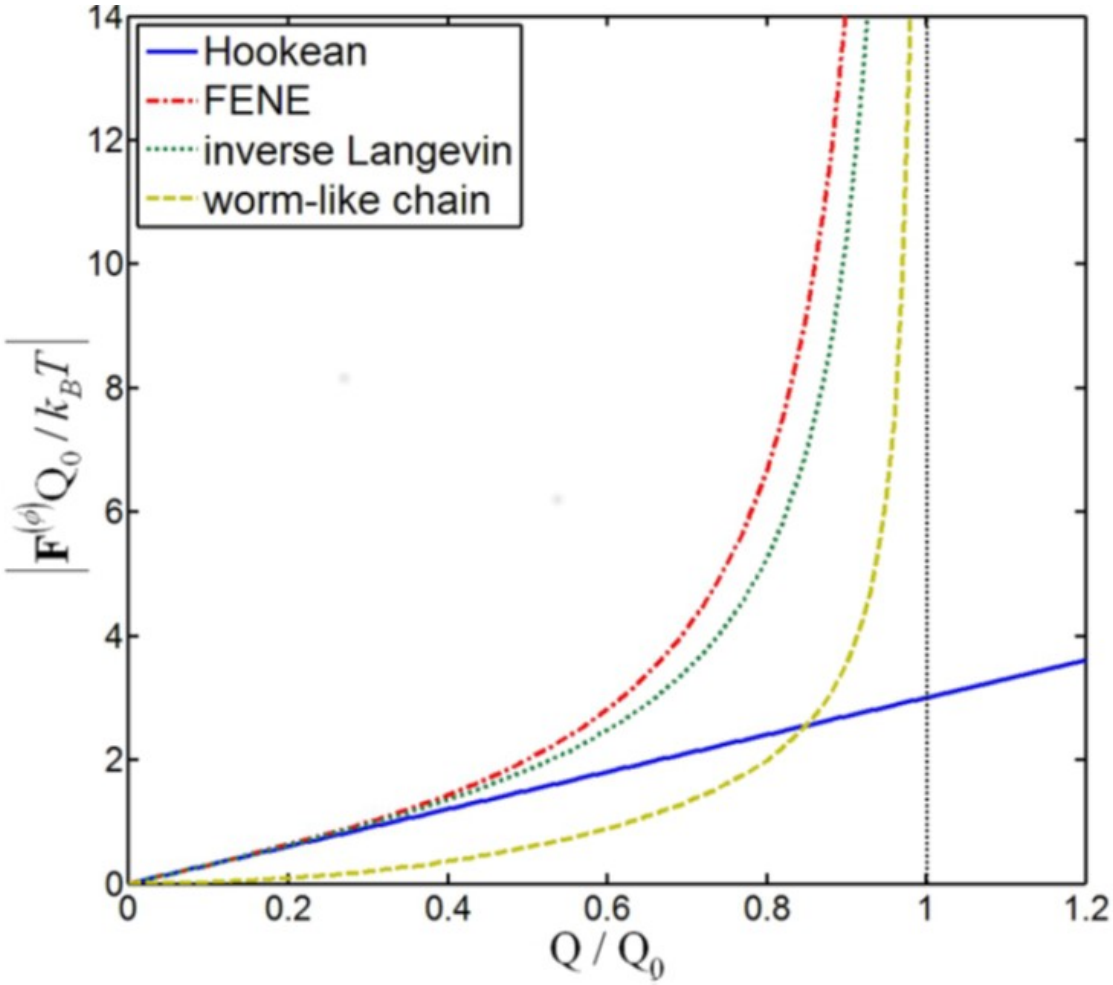

Figure A.1: Force-extension relationship for different springs employed in Brownian dynamics (BD) simulations. Figure reproduced from [4].

A.2 Simulation setup

The wormlike micelle chains are represented as a series of beads connected by entropic springs. The beads are subjected to constant bombardment by solvent molecules which we depict as stochastic forces are they diffuse in the medium. The resulting Langevin equation of motion Eq. (A.1a) [1, 2] for each inertia-less bead (i.e. overdamped dynamics) of every bead-spring chain is solved using Somasi's predictor-collector algorithm [3].

$$\frac{d\mathbf{r}}{dt} = \frac{1}{\zeta}\mathbf{F}_i^{flow} + \frac{1}{\zeta}[\mathbf{F}_{i+1}^S - \mathbf{F}_i^S] + \frac{1}{\zeta}\mathbf{F}_i^R \tag{A.1a}$$

$$\mathbf{F}_i^{flow} = \zeta(\kappa(r_i) \cdot r_i + \mathbf{v}_i') \tag{A.1b}$$

$$\mathbf{F}_I^S = \frac{k_B T(\alpha\hat{r} - \beta\hat{r}^3)}{b_K(1 - \hat{r}^2)} \tag{A.1c}$$

$$\mathbf{F}_I^R = \sqrt{\frac{6k_B T\zeta}{\Delta t}}\mathbf{n}_i \tag{A.1d}$$

where $\mathbf{r}_i$ is the position vector of the ith bead in a bead, ζ is the drag coefficient, κ is the transpose of the velocity gradient tensor, $\mathbf{v}_i'$ accounts for the variation in the local flow field around r_i due to intra-molecular hydrodynamic interaction with surrounding beads [4], $\mathbf{F}_I^R$ is the Brownian force, $\mathbf{F}_i^{flow}$ is the drag force due to flow, and $\mathbf{F}_i^S$ and $\mathbf{F}_{i+1}^S$ represents forces due to i and $i+1$th springs. In the absence of hydrodynamic interaction, as is the case in our simulation results presented here, $\mathbf{v}_i' = 0$. The Cohen-Pade approximation of the inverse Langevin function [5], Eq. (A.1c) is used to represent the spring-force law. α and β have values of 3 and 1 respectively due to their independence with coarse-graining [2]. The equations were made dimensionless by scaling length with the Kuhn length (b_K), force with $k_B T/b_k$ and time with $\zeta b_K^2/k_B T$ [2].

Two-specie reversible scission of wormlike micelles

We simulate the micelle reversible scission kinetics as described in Section 2.2. Additionally, we include shear-induced scission into kinetics following the VCM model [6]. The shear-induced scission is implemented using Larson's Partially Extended Convected (PEC) model given by the second term on Eq. (A.2a) [7, 6].

$$c_A = c_{Aeq} + \frac{1}{3}\xi\mu\left(\underset{=}{\dot{\gamma}} : \frac{\mathbf{R_{gA}}}{n_A}\right) \tag{A.2a}$$

$$c_B = c_{Beq} \tag{A.2b}$$

where ξ is the shear-induced breakage rate, $\mathbf{R_{gA}}$ is the ensemble average radius of gyration tensor for the long species micelles defined as Eq. (A.3) and $\mu = \lambda_A/\lambda_{eff} = 1+c_{Aeq}$. λ_A and λ_{eff} are the relaxation times for the long species and the cooperative (effective) network relaxation time [6].

$$\mathbf{R_{gA}} = \left\langle \frac{1}{2N_A^2} \left(\sum_i^{N_A} \sum_j^{N_A} (\mathbf{R}_{ij})^2 \right) \right\rangle \tag{A.3}$$

The simulation was run using a time-step of 10^{-3} dimensionless time. The number of Kuhn segments per spring, $N_{k,s} = 6$, shear-induced scission rate, $\xi = 0.3$, and, the number of springs in long species chains, $N_A = 6$. The equilibrium number of long chains at equilibrium, $\mathcal{N}_{A0} = 100$ while the ratio of short to long chains at equilibrium, $N_{B0} = 1$. The simulation was run and averaged for an ensemble of 100. The stress was calculated as Eq. (A.4)

$$\boldsymbol{\sigma}_A = n_A \sum_{k=1}^{N_A-1} \left\langle \mathbf{F}_k^S \mathbf{Q}_k \right\rangle_A \tag{A.4a}$$

$$\boldsymbol{\sigma}_B = n_B \sum_{k=1}^{N_B-1} \left\langle \mathbf{F}_k^S \mathbf{Q}_k \right\rangle_B \tag{A.4b}$$

A.3 Results

In Figure A.2a, we observe that the number densities of long and short chains fluctuate about 1. This indicates that at a Weissenberg number of unity and $\xi = 0.3$, the flow does not induce much scission of the long micelles. We observe a moderate stress overshoot of the transient stress in Fig. A.2b. However, at $Wi = 10$, we observe a higher number density of short species (see Fig. A.3a) despite the ratio of short to long chains at equilibrium, $N_{B0} = 1$. This is because of the higher scission rates from the contribution of the flow to the scission of long species micelles. At this very high shear rate, we observe a pronounced overshoot of the transient stress curve in

Fig. A.3b.

The blue stress curve in Figure A.4 can be described as gentle rise from zero to a steady shear stress value of about 40 in about 0.3 dimensionless time for a breakage time of 0.02. As the breakage rate increased 200 fold, the red curve in Fig. A.4 shows a substantial reduction in stress values obtained. This agrees with the theory that breaking and recombination of wormlike micelle chains is a mechanism for relieving stress. It suggests that the more breaking and recombination events occurring a systems, the lower the stress that would be felt in the system. Figure A.5 shows plots of the dimensionless steady shear stress, $\sigma_{12s.s} = \sum_{\alpha=A,B} \sigma_{12\alpha s.s}/G_\alpha$ and viscosity values $\sigma_{12s.s}/\dot{\gamma}$. with dimensionless shear rate. The viscosity curve depicts a shear thinning behavior because the viscosity reduced with increasing shear rate. The steady shear stress rose steadily to a plateau with a tendency of an upturn at higher dimensionless shear rates. These results are in line with known rheological responses. The stress plateau has been attributed to shear banding and mechanical instabilities. See further details in Section 1.3.2.3.

Bibliography

[1] R. G. Larson, Journal of Rheology **49**, 1 (2005).

[2] I. S. Dalal, N. Hoda, and R. G. Larson, Journal of Rheology **56**, 305 (2012).

[3] M. Somasi, B. Khomami, N. J. Woo, J. S. Hur, and E. S. Shaqfeh, Journal of Non-Newtonian Fluid Mechanics **108**, 227 (2002).

[4] C. Cruz, F. Chinesta, and G. Régnier, Archives of Computational Methods in Engineering **19**, 227 (2012).

[5] a. Cohen, Rheologica Acta **30**, 270 (1991).

[6] P. a. Vasquez, L. P. Cook, G. H. Mckinley, and L. Pamela Cook, Journal of Non-Newtonian Fluid Mechanics **144**, 122 (2007).

[7] R. G. Larson, Journal of Rheology **28**, 545 (1984).

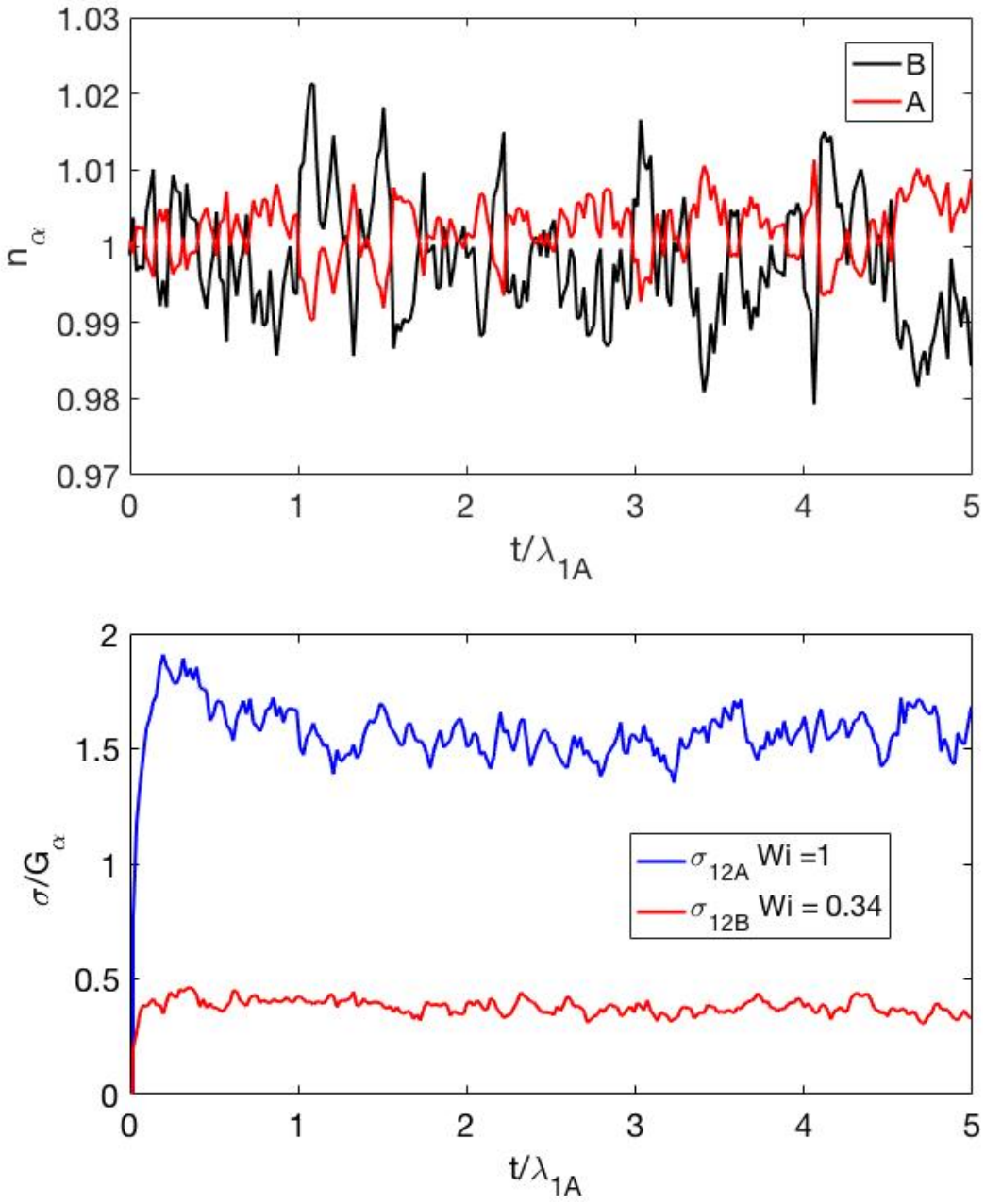

Figure A.2: Normalized number density (top) and dimensionless stress (bottom) against dimensionless time at Weissenberg number, $Wi = 1$.

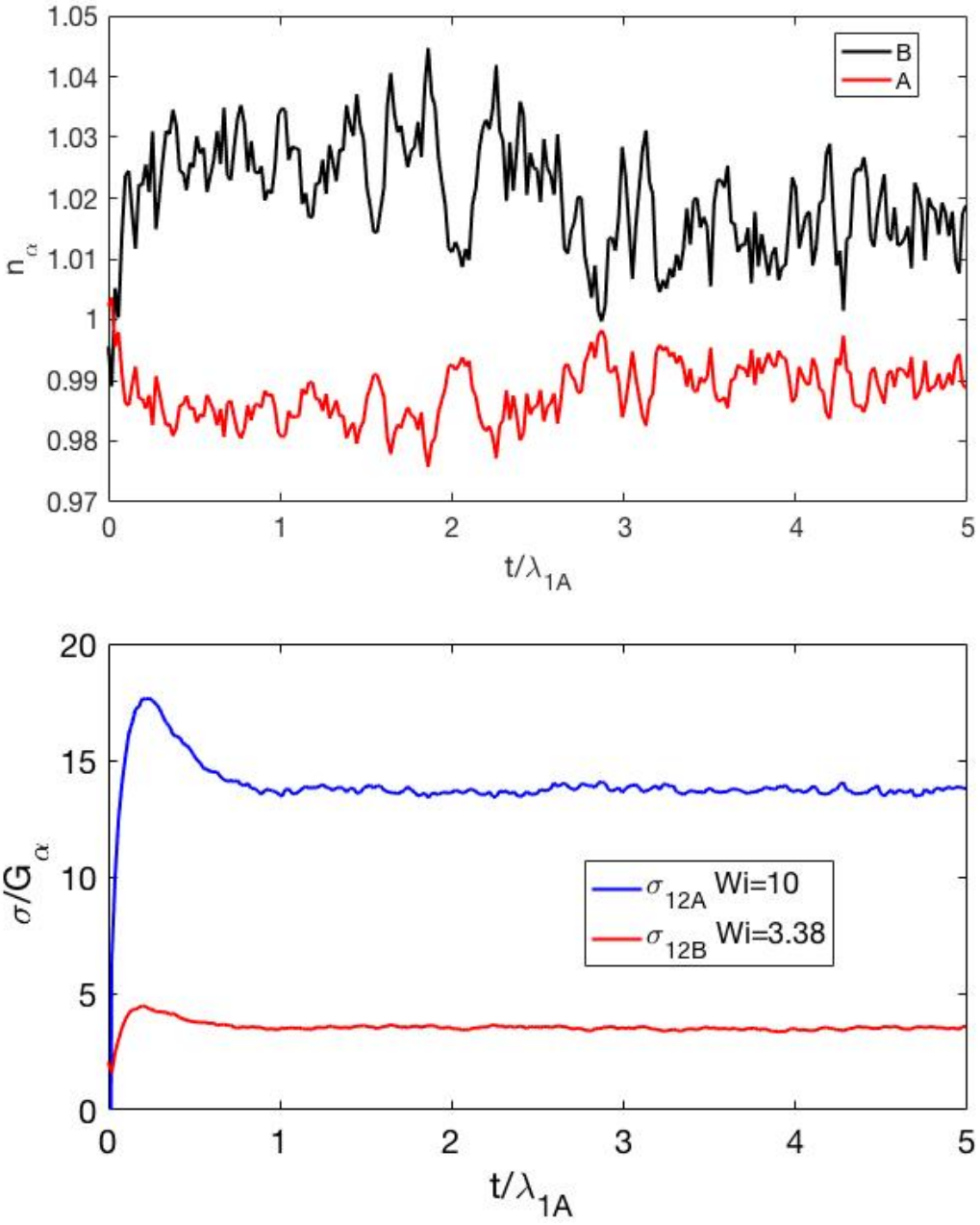

Figure A.3: Normalized number density (top) and dimensionless stress (bottom) against dimensionless time at Weissenberg number, $Wi = 10$.

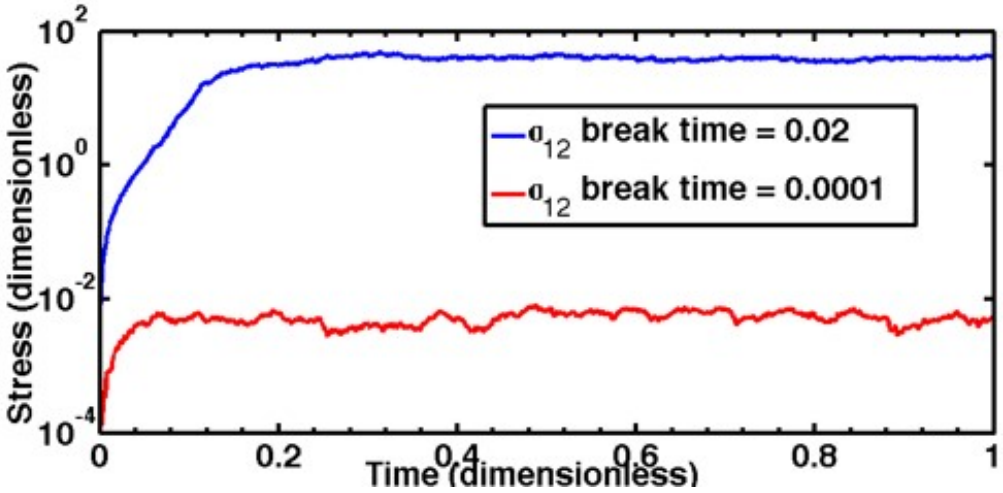

Figure A.4: Normalized number density (top) and dimensionless stress (bottom) against dimensionless time at Weissenberg number, $Wi = 100$. $N_{k,s} = 10$ and $c_{Aeq} = 3.5$ in this simulation. The overshoot is not visible beacuse it is plotted on a semi-log scale to accommodate both graphs.

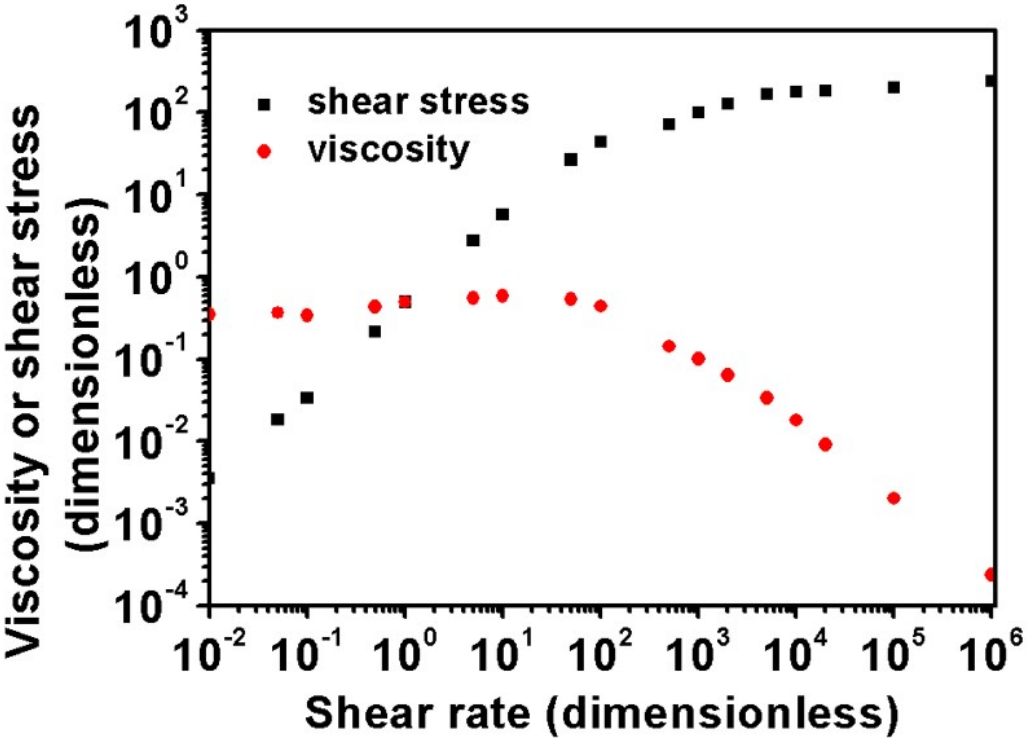

Figure A.5: Dimensionless steady shear stress (black squares) and viscosity (red circles) against dimensionless shear rates. Same parameters are used in this simulation as Fig. A.4

APPENDIX B

Development of Constitutive Equation for Two-species Reversible Scission and Deformation of Rigid Micelles

B.1 Constitutive Equations Development

The formulation of this constitutive equation assumes that two short species dumbbells fuse into a longer dumbbell twice the size of the short dumbbells similar to the VCM model. We also assume that after the fusion of two short dumbbells, the average isotropic stress of the long species is unaffected and only the deviatoric stresses are perturbed by the addition of short species dumbbells. Let $\mathbf{S}$ be the tensor for the short chains containing the deviatoric stress contribution of the short chains. We define $\mathbf{S}$ as

$$\mathbf{S} = \left\langle \vec{Q}\vec{Q} \right\rangle_s / Q_{s0}^2 - 1/3\underline{\underline{\delta}} \tag{B.1}$$

where $\left\langle \vec{Q}\vec{Q} \right\rangle_s$ is the ensemble average of the end-to-end vector of short chains, $\langle .. \rangle$ represents ensemble average. Q_{s0}^2 is the end-to-end length of short chains at equilibrium and $1/3\underline{\underline{\delta}}$ is the isotropic stress contribution. Similarly, for long chains,

$$\mathbf{L} = \left\langle \vec{Q}\vec{Q} \right\rangle_l / Q_{l0}^2 - 1/3\underline{\underline{\delta}} \tag{B.2}$$

where $\left\langle \vec{Q}\vec{Q} \right\rangle_l$ is the ensemble average of the end-to-end vector of long chains, Q_{l0}^2 is the end-to-end length of long chains at equilibrium.

When two short dumbbells fuse into a longer dumbbell, the isotropic parts combine as

$$\vec{n}_s \rightarrow 2\vec{n}_s \tag{B.3}$$

$$\sqrt{tr\mathbf{S}}\vec{n}_s \rightarrow 2\sqrt{tr\mathbf{S}}\vec{n}_s \tag{B.4}$$

where $\sqrt{tr\mathbf{S}}$ is the length of the short dumbbell. After fusing, the new tensor is the product

$$2\sqrt{tr\mathbf{S}}\vec{n}_s \cdot 2\sqrt{tr\mathbf{S}}\vec{n}_s = 4tr\mathbf{S}\vec{n}_s\vec{n}_s \tag{B.5}$$

By multiplying the mean square end-to-end vector of the short chains at equilibrium, the new (fused) tensor in dimensional terms is $4tr\mathbf{S}Q_{s0}^2\vec{n}_s\vec{n}_s$. Since, $\mathbf{S} = tr\mathbf{S}\vec{n}_s\vec{n}_s$, then

$$4tr\mathbf{S}\vec{n}_s\vec{n}_s = 4\mathbf{S}Q_{s0}^2 \tag{B.6}$$

Substituting Eq. (B.1) in Eq. (B.6) gives

$$4\left(\left\langle \vec{Q}\vec{Q} \right\rangle_s - 1/3Q_{s0}^2\underline{\underline{\delta}}\right) = 4\left\langle \vec{Q}\vec{Q} \right\rangle_s^a \tag{B.7}$$

where $\left\langle \vec{Q}\vec{Q} \right\rangle_s^a$ represents the anisotropic part of the fused stress tensor. Following our initial assumption, we obtain the total stress of the resultant fused dumbbell from two short dumbbells by adding the anisotropic contribution to the isotropic stress of the long dumbbells. Therefore, stress contribution to long species micelles from fusion of short species micelles is

$$Stress \quad gained = 4\left\langle \vec{Q}\vec{Q} \right\rangle_s^a + 1/3Q_{l0}^2\underline{\underline{\delta}} \tag{B.8}$$

Similarly, a long dumbbell can break to give two short chains. Thus,

$$\sqrt{tr\mathbf{L}}\vec{n}_l \rightarrow 1/2\sqrt{tr\mathbf{L}}\vec{n}_l \tag{B.9}$$

where $\sqrt{tr\mathbf{L}}$ is the length of the long dumbbell. The new tensor is therefore

$$1/2\sqrt{tr\mathbf{L}}\vec{n}_l \cdot 1/2\sqrt{tr\mathbf{L}}\vec{n}_l = 1/4tr\mathbf{L}\vec{n}_l\vec{n}_l \tag{B.10}$$

Given $\mathbf{L} = tr\mathbf{L}\vec{n}_l\vec{n}_l$,

$$1/4tr\mathbf{L}\vec{n}_l\vec{n}_l = 1/4\mathbf{L}Q_{l0}^2 \tag{B.11}$$

Substituting Eq. (B.2) in Eq. (B.11) gives

$$1/4\left(\left\langle\vec{Q}\vec{Q}\right\rangle_l - 1/3Q_{l0}^2\underline{\underline{\delta}}\right) = 1/4\left\langle\vec{Q}\vec{Q}\right\rangle_l^a \tag{B.12}$$

where $\left\langle\vec{Q}\vec{Q}\right\rangle_s^a$ represents the anisotropic part of the fused stress tensor. Similarly, we add the anisotropic contribution of the broken long dumbbell to the isotropic stress of the short dumbbells. Therefore, stress contribution to short species micelles from scission of short species micelles is

$$Stress \quad gained = 1/4\left\langle\vec{Q}\vec{Q}\right\rangle_l^a + 1/3Q_{s0}^2\underline{\underline{\delta}} \tag{B.13}$$

From Section 2.2, we obtained Eq. (2.4) as

$$\frac{dn_A}{dt} = \frac{c_B}{2}n_B^2 - c_A n_A \tag{B.14a}$$

$$\frac{dn_B}{dt} = -c_B n_B^2 + 2c_A n_A \tag{B.14b}$$

where c_A and c_B are the rates for breaking and rejoining of long and short chains respectively. The above equations are identical to the corresponding equations of

the VCM model. Therefore, the constitutive equation is obtained by multiplying the rates in Eq. (B.14) by the respective stress contributions Eqs. (B.8) and (B.13) and adding to the Upper-Convected Maxwell equation for dumbbells.

$$n_A \overset{\nabla}{\boldsymbol{\sigma}}_A + \frac{n_A}{\lambda_A}\left(\boldsymbol{\sigma}_A - G_A\boldsymbol{\delta}\right) = \left(\frac{1}{2}c_B n_B^2\left[4H_B\left\langle\vec{Q}\vec{Q}\right\rangle_B^a + \frac{1}{3}H_A Q_{A0}^2\boldsymbol{\delta}\right]\right) - c_A n_A H_A\left\langle\vec{Q}\vec{Q}\right\rangle_A \tag{B.15a}$$

$$n_B \overset{\nabla}{\boldsymbol{\sigma}}_A B + \frac{n_B}{\lambda_B}\left(\boldsymbol{\sigma}_B - G_B\boldsymbol{\delta}\right) = \left(2c_A n_A\left[\frac{1}{4}H_A\left\langle\vec{Q}\vec{Q}\right\rangle_A^a + \frac{1}{3}H_B Q_{B0}^2\boldsymbol{\delta}\right]\right) - c_B n_B H_B\left\langle\vec{Q}\vec{Q}\right\rangle_B \tag{B.15b}$$

where subscripts s and l have been substituted with B and A respectively for consistency with previous equations. $H_\alpha = 2k_BT\beta_s\alpha^2$ is the Hookean spring constant and $\beta_s\alpha^2 = 3/(2N_{k,s\alpha}b_k^2)$ is the elasticity of the spring in species α.

B.2 Result

Figure B.1 shows that both BD simulations and the model give matching predictions in the absence of reversible scission. This is because the equations becomes uncoupled Maxwell equations, see Section 2.4 for details. In Fig. B.2, we observe over-prediction of the stress response for long chains by the Rigid Micelles ("VCM-R1") model and an under-prediction of that of the short micelles. This discrepancy is likely as a result of the underlying assumption of the model which states that the stress tensor quadruples when two chains fuse. That is, the radius of gyration and the gyration tensor always increases in fusion events. Thus, the model cannot capture fusion events that result in "back-folding", see Fig. 2.4. The model however, may be suitable for predicting the dynamics of very rigid "rod-like" micelles in which case the fusion can only be by end-to-end interaction such that the radius of gyration increases.

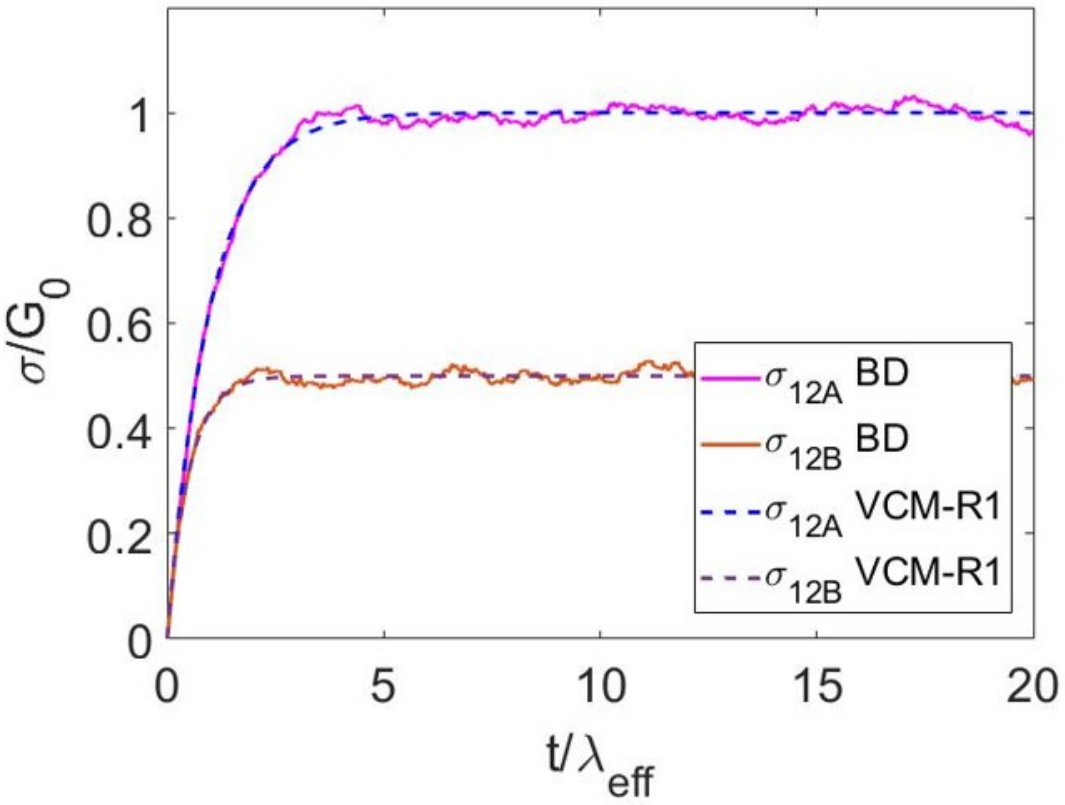

Figure B.1: Comparison of stress contributions from long (subscript A) and short (subscript B) chains for Brownian Dynamics (BD) simulation and for Rigid Micelles (marked VCM-R1) model without reversible scission at Weissenberg number of unity.

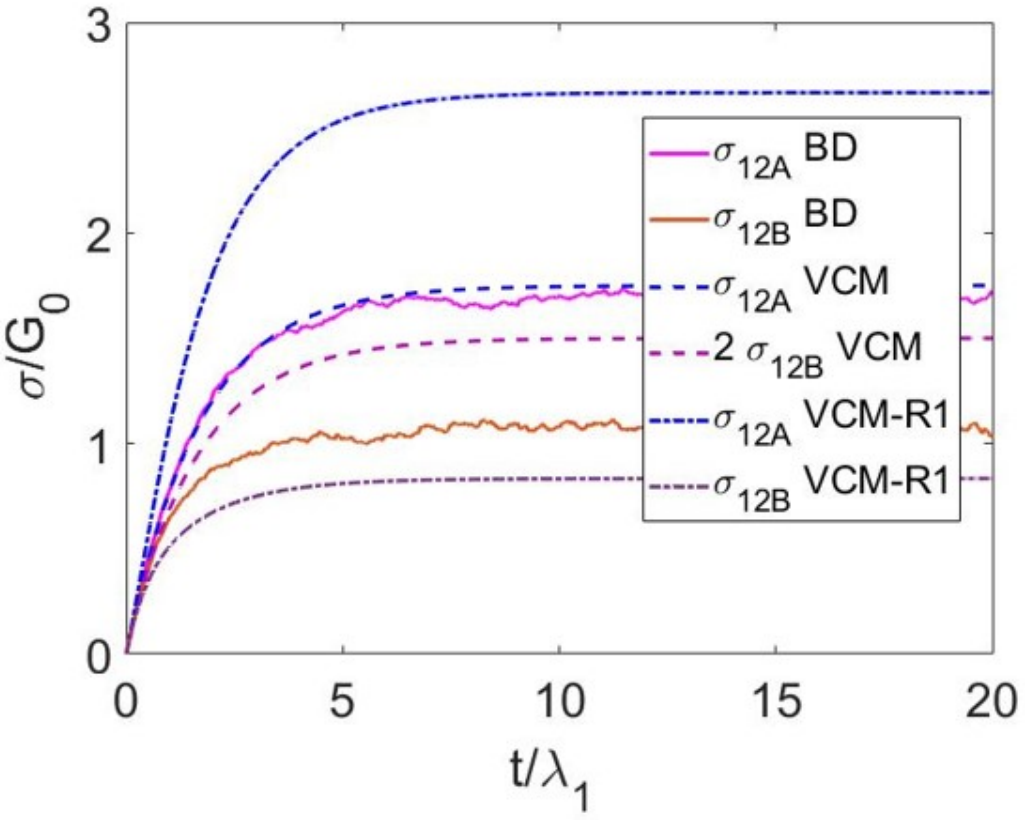

Figure B.2: Similar to Fig. B.1 but with VCM model predictions (marked VCM) and with scission rate, $c_{Aeq}\lambda_{1A} = 1$.

Bibliography

APPENDIX C

Modified Rouse Linear Entangled Polymers (Rolie-Poly) Model

C.1 Rouse Linear Entangled Polymers (Rolie-Poly) Model

The Rolie-Poly model is an advancement of the reptation theory and tube model. The Rolie-Poly equation is a single-mode approximation of a more complex GLAMM (Graham Likhtman McLeish Milner) [1] model. It was developed by Likhtman and coworkers in order to provide a simpler, less tedious and computationally compatible equation that would mitigate the difficulty and expense of coupling the GLAMM in other CFD applications, yet providing the underlying physics to get qualitatively similar rheological predictions [2]. The Rolie-Poly model is given as Eq. (C.1) [2].

$$\overset{\nabla}{\underset{=}{\sigma}} + \frac{1}{\tau_d}\left(\underset{=}{\sigma} - \underset{=}{I}\right) + \frac{2}{\tau_R}\left(1-\lambda^{-1}\right)\left[\underset{=}{\sigma} + \beta(\lambda^2)^{\delta}\left(\underset{=}{\sigma} - \underset{=}{I}\right)\right] = \underset{=}{0} \tag{C.1}$$

where $\overset{\nabla}{\underset{=}{X}} = \dot{\underset{=}{X}} - \underset{=}{\nabla v}^T \cdot \underset{=}{X} - \underset{=}{X} \cdot \underset{=}{\nabla v}$. The constitutive equation is modeled towards the description of fast flows in entangled polymers. Therefore, it incorporates faster relaxation mechanisms like contour length fluctuations (CLF), convective constraint release (CCR), and chain stretch, which are on shorter time scales compared to reptation [2, 3]. Convective constraint release (CCR) is the removal of the topological

constraints (entanglements) imposed by surrounding chains on the primitive chain by convection of the shearing flow [4, 5]. CCR occurs at a rate porportational to the inverse of the shear rate and is the dominant mechanism of stress relaxation in nonlinear flows or large step strain experiments [2, 5].

C.2 Modified Rouse Linear Entangled Polymers (Rolie-Poly) Model

The Rolie-Poly model successfully predicts transient overshoots in startup shear with unique undershoots at shear rates in concordance with Osaki's [6] experiments. Likhtman et al. [2] predicted shear damping function in good agreement with the original Doi-Edwards theory [2]. It has also been modified by Cromer et al. [7] and Adams et al. [3] to study concentration fluctuations and inhomogeneities leading to shear banding.

To investigate effect of concentration, we introduce finite extensibility to the stretch characterized by the maximum extensibility parameter, λ_{max}. The relation between maximum stretch and concentration given by $\lambda_{max} = \lambda_{max0}\underset{\_}{\phi}^{c}$ where λ_{max0} is the maximum chain stretch at equilibrium. We therefore obtain a modified Rolie-Poly model, with a nonlinear spring constant, k_s, which is of the FENE-P type i.i. Finitely Extending Nonlinear Elastic with Peterlin approximation [7, 8].

$$\overset{\nabla}{\underset{=}{Q}} + \frac{1}{\tau_d}\left(\underset{=}{Q} - \underset{=}{I}\right) + \frac{2}{\tau_R}k_s\left(1-\lambda^{-1}\right)\left[\underset{=}{Q} + \beta(\lambda^2)^{\delta}\left(\underset{=}{Q} - \underset{=}{I}\right)\right] = \underset{=}{0} \tag{C.2}$$

$$\underset{=p}{\sigma} = G(\phi)\left(k_s\underset{=}{Q} - \underset{=}{I}\right) \tag{C.3}$$

$$k_s = \left(\lambda_{max}^2 - 1\right) / \left(\lambda_{max}^2 - \lambda^2\right) \tag{C.4}$$

We refer to Eqs. (C.2) to (C.4) as the modified Rolie-Poly equation. τ_d and τ_R are

the disentanglement and Rouse times respectively. $\lambda = l/l_0 = \sqrt{tr\underline{\underline{Q}}/3}$ is the stretch parameter and $\lambda_{max} = l_m/l_0$ is the maximum stretch of the tube. l and l_m are the instantaneous and maximum tube length containing an entanglement segment respectively and l_0 is the equilibrium tube length. $\underline{\underline{Q}}$ is the orientation tensor [9, 10] and $\overset{\nabla}{\underline{\underline{Q}}}$ is as defined previously in Section C.1. G(ϕ) is the plateau modulus [7]. β is an adjustable parameter from 0 to 1 that proportional to the rate at which entanglement constraints are released by the convection of flow (CCR) [2, 11]. An alternative nonlinear spring constant [2] could be used in the modified Rolie-Poly model:

$$k_s = \left(\lambda_{max}^2\right) / \left(\lambda_{max}^2 - \lambda^2\right) \tag{C.5}$$

Modification of the Rolie-Poly equation by Adams et al. [12] to include diffusion and solvent stress has been used to predict transient banding in entangled polymers. This has been noted by Berret [13], Cates [14] and Ravindranath [15]. However, the predictions of Adams et al. did not match experiments quantitatively, they required large entanglement number, Z=265 while experiments observed banding between 15 and 50 [3]. The entanglement number is defined as the ratio of the disengagement to Rouse time, [3, 16]

$$Z = \frac{1}{3}\frac{\tau_d}{\tau_R} \tag{C.6}$$

where τ_d and τ_R have definitions as in Eq. (C.2) above.

C.3 Modelling of the modified Rolie-Poly model

The modified Rolie-Poly model was non-dimensionalized as follows: $t^* = t/\tau_R$, $\underline{\underline{\sigma}}_p^* = \underline{\underline{\sigma}}_p/G$, $\dot{\gamma}^* = \dot{\gamma}\tau_R$ and $\tau_d^* = \tau_d/\tau_R$. Optimal values of CCR parameter, $\beta = 1$ and $\delta = -0.5$ were set to fit transient and steady-state predictions of GLAMM in concordance with Likhtman [2]. The ratio of reptation to Rouse time, $\tau_d^* = 100$ which corresponds to entanglement number $Z = 33.3$. Initial values used were: $\lambda =$

1, $t^* = 0$, $Q_{11} = 1$, $Q_{12} = 0$, $Q_{22} = 1$ and $Q_{33} = 1$. Other elements of $\underline{\underline{Q}}$ not mentioned above were set to zero.

The step strain could be modelled as an instantaneous jump in strain from zero to a finite strain using a step function. However, this method does not simulate the experimental conditions. In experiments, the rheometer cannot perform a step ramp to the desired strain due to instrument and geometry inertia. Also, during the rapid ramp-up of shear, the chains are stretched rapidly but at the same time some of the stress developed is relaxed almost instantaneously by the fast modes of relaxation such as retraction. However, the use of a step function as a 'switch' and/or 'shutting off' of the fast-mode relaxations during this period would cause some of the physics to be lost and the make the model less realistic. We therefore model using a high shear rate of 250 to reach the desired strain in a very short time (about 0.02 dimensionless time to reach a strain of 2.5). Note: $\dot{\gamma} = d\gamma/dt$. The lag of 0.01 dimensionless time to get to a strain of 2.5 during the 'step' proves of some fast mode relaxation. Time step of 10^{-6} was used in modeling. The equations were solved using Euler integration in FORTRAN. Once the strain, γ reached the desired value, the shear rate, $\dot{\gamma}$ was turned to zero thereby keeping the strain constant at that value. The stress is then outputted from the equations. Stress relaxation modulus is then computed. This code was run for different maximum extensibilities ($\lambda_{max} = 5$, 10 and 20) and strains of 1, 2.5 and 4.

In the modelling of startup flow, same equations and initial values were used. The code was repeated for maximum extensibilities, λ_{max} of 5 and 10 for different shear rates ranging between 0.0001 and 200. The model was re-run for Z=50. Unlike in the step strain runs, strain is not controlled and is allowed to build-up. The evolution of stress and stress relaxation modulus are outputted from the model.

C.4 Results and Analysis

Figure C.1a shows the variation of shear stress with shear rate. As the shear rate is increased, the stress increases up to a critical shear rate where the shear stress becomes invariant with changes in shear rate. This leads to the formation of a stress plateau which spans about three decades between $10^{-2} \leq Wi \leq 10^{0}$. This indicates that within the stress plateau, different shear rates can co-exist at the same stress. Under this condition, the entangled polymer solution separates into distinct bands of bands of fluids each moving at different shear rates. We cannot ascertain how many of such distinct bands could form with this model. However, we know that at least two bands would form in a bid to maintain a mean shear rate along the flow curve. A high shear band with a magnitude proximate to that of the upper critical shear rate and another low shear band about the would exist with a value about the lower critical shear rate. In our model, we observe the lower and upper critical shear rates to be Weissenberg numbers ($Wi = \dot{\gamma}\tau_R$) of 0.04 and 0.4 respectively. The stress plateau is an indicator of occurrence of shear banding. Although, the modified Rolie-Poly model does not include reversible scission, it accurately predicts the stress plateau is as observed in experiments of Lopez-Barron [17, Fig 2(a)] and Miller [18, Fig 7]. The modified Rolie-Poly model presented in this work is in essence a monotonic constitutive equation capable of qualitatively predicting shear banding in entangled polymers and wormlike micelles.

The modified Rolie-Poly model predicts shear thinning from the plot of viscosity as a function of shear rate (see Fig. C.1b) in line with experiments of Miller [18, Fig 4]. The observed reduction of viscosity is due to the alignment of the micelles in the direction of flow thereby reducing their resistance to flow (viscosity). The zero-shear viscosity defined as the steady viscosity as very low shear rate of the wormlike micelles depends on the ratio of the reptation time to the Rouse time. In essence, the number of entanglements, Z. This informs us that the resistance offered by the

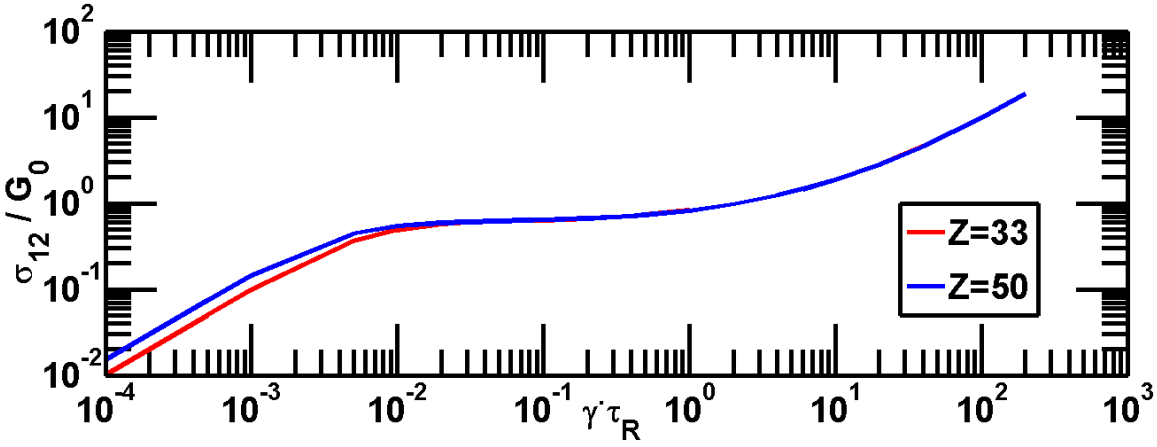

(a)

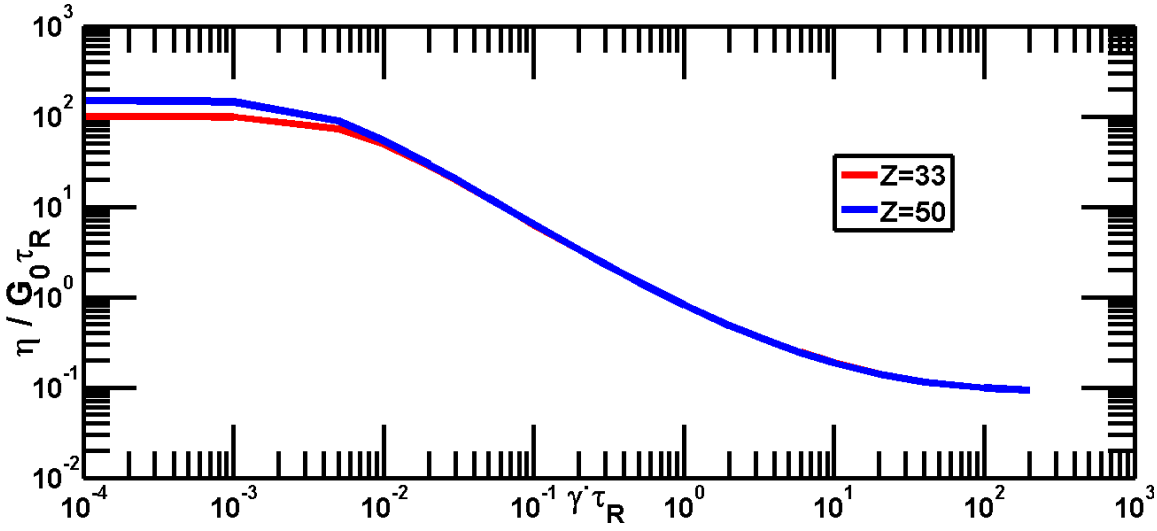

(b)

Figure C.1: (A) Shear banding of wormlike micelles predicted by stress plateau (B) Shear thinning of wormlike micelles as shear rate increases.

entanglement network is a significant contributor to viscosity in the linear regime. Similar dependence is seen in Miller's experiments in which he varied the concentrations of the wormlike micelles in the experimental runs. This reinforces the existence of inter-relationships between entanglement, concentration and viscoelasticity.

The startup shear curve (FigureC.2b) at moderate shear rates $\dot{\gamma} = 1$ and $\dot{\gamma} = 10$ agrees qualitatively with the experiments of Lopez-Barron [17, see Fig 2(b)] predicting mild stress overshoots at moderate shear rates. The gentle slope at the onset of the overshoot indicates the build-up of stress due to straining of the entanglements. It also predicted the sharp peak of stress overshoots observed by Lopez-Baron [17, see Fig. 6(a)] at high shear rates. The peak is formed as a result of excessive instantaneous strain applied on the entanglement network leading to a stress overshoot. This is then quickly relaxed by the retraction of the wormlike micelles towards their equilibrium length. Lopez-Barron and coworkers identified the region after the overshoot as a metastable state with some inhomogeneities that heralds the formation of shear bands before reaching a plateau. However, the modified Rolie-Poly model failed to predict this metastable state which is characterized by long transients. Instead, it proceeds to steady state after the overshoot. This inadequacy suggests the need for further improvement of the model.

The relaxation mechanism after step strain observed from the modified Rolie-Poly (figure C.3a) indicated strain hardening at high strains of $\gamma = 4$ (green line) at early times of about 0.01 - 0.1 dimensionless time. This is due to the increase in stress relaxation modulus relative to the linear response represented by the (blue line) at $\gamma = 1$. The relaxation was not mono-exponential in time. This indicates the presence of more than one mode of relaxation: the fast modes e.g. retraction and the slow modes e.g. reptation. This is in line with the measurements of Brown et al. [19] (see fig. 2b of reference) and Fig. 4.6 in Section 4.3.2. Additionally, strain hardening is observed during start-up shear (Figure C.2a) at a shear rate of 40 (equivalent to strain

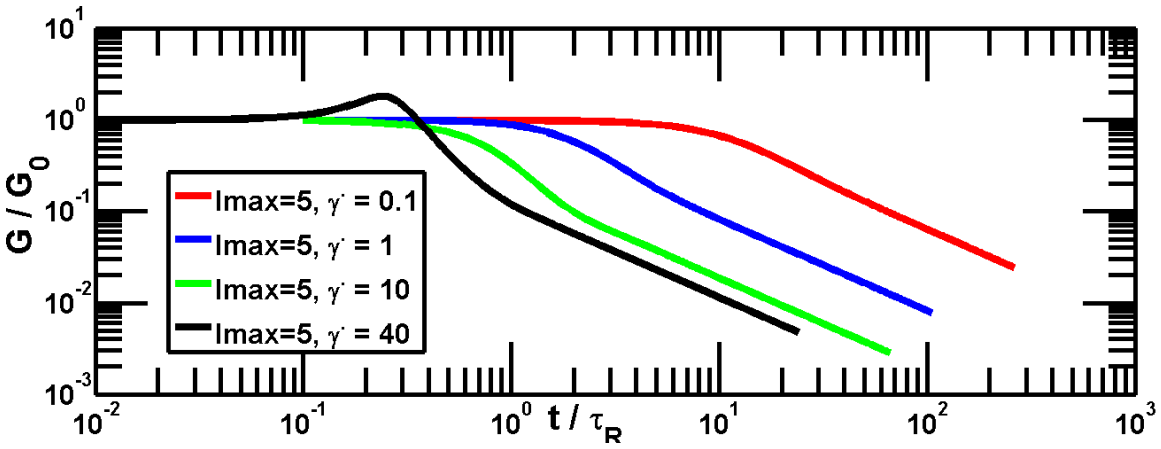

(a)

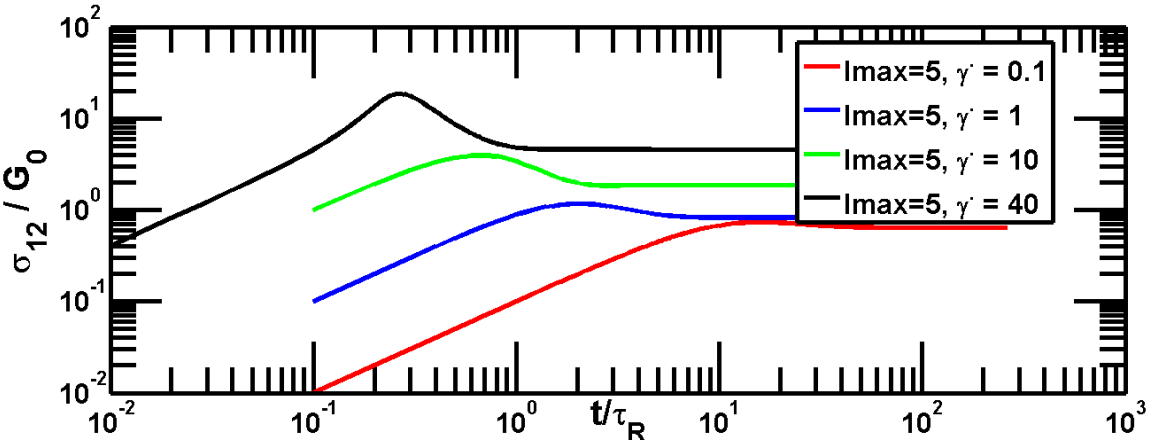

(b)

Figure C.2: Modulus exhibits (A) hardening and (B) pronounced stress overshoot in start-up flow at high shear rate of 40.

of 4 at 0.1 dimensionless time). The mild strain hardening in is followed by strain softening attributed to the quick retraction of the chain segments into their tubes towards the equilibrium length. The relaxation then progresses slowly by reptation at about 2 dimensionless time. The model predicted no dependence on the finite extensibility on the relaxation mechanism (not shown). This is attributed to the high rate of convective constraint release which reduces the effect of chain stretch drastically thereby causing the effect of finite extensibility of the chain during stretch (i.e. deformation) insignificant in the relaxation mechanism of stress.

The model also predicts the Lodge-Meissner relationship holds for the entangled polymer solutions (see figure C.3b). The Lodge-Meissner rule states that the ratio of the first normal stress difference to the shear rate following a step strain is constant that equals the applied strain [19]. Modified Rolie-Poly however violates this relationship at long times and large strains. A plausible culprit is the shear banding of stress into layers of high and low shear rates. This causes an increase in the ratio of first normal stress difference to shear stress compared to the strain at the low band regions. Similar views are held by Brown et al.[19]. The result agrees with the predictions of the modified Rolie-Poly model and the step strain experiments of Larson et al. [20] and Brown et al. [19].

C.5 Summary

Nonlinear rheological phenomena such as stress plateau, shear thinning, strain hardening and softening and the Lodge-Meissner relationship have been predicted by the modified Rolie-Poly model. The modified Rolie-Poly presented herein is an example of a monotonic constitutive equation that predicts shear banding. A mild strain hardening following a step strain was observed followed by a multi-process relaxation. Stress overshoot in the transient for shear startup flow was adequately predicted by the model. However, it failed at predicting the long metastable tran-

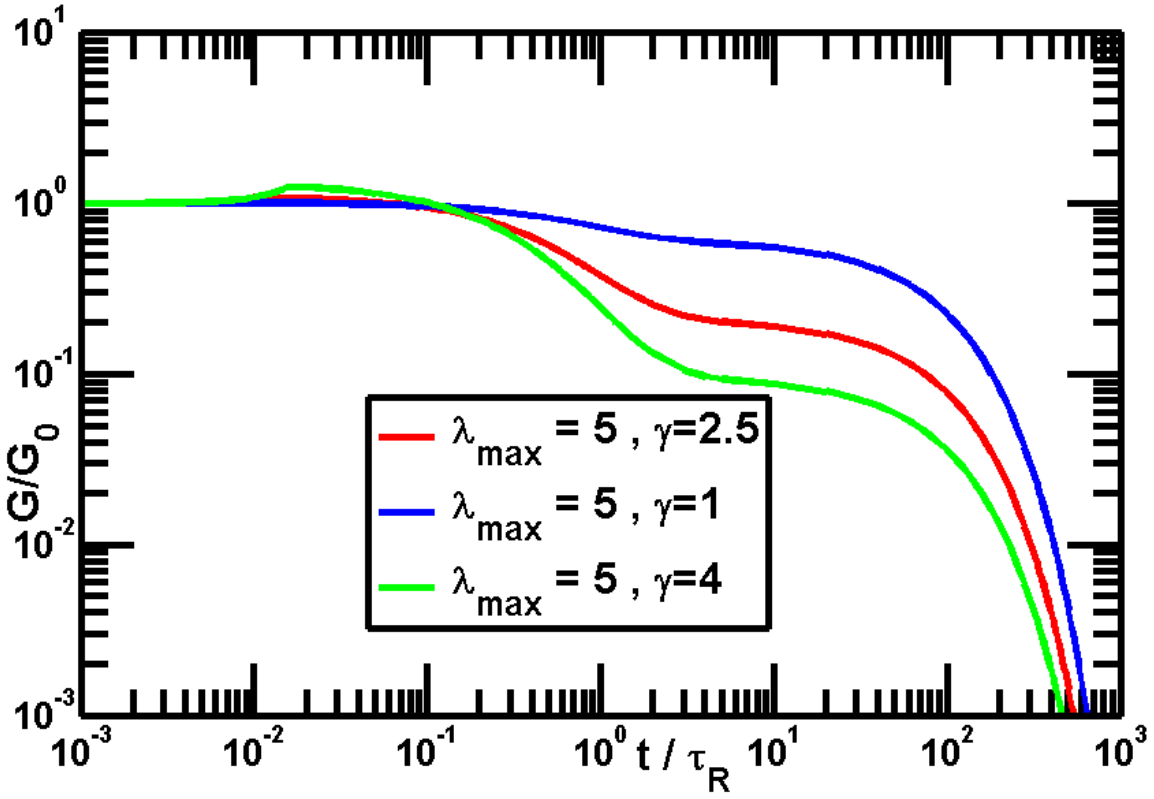

(a) Stress relaxation moduli at different strains

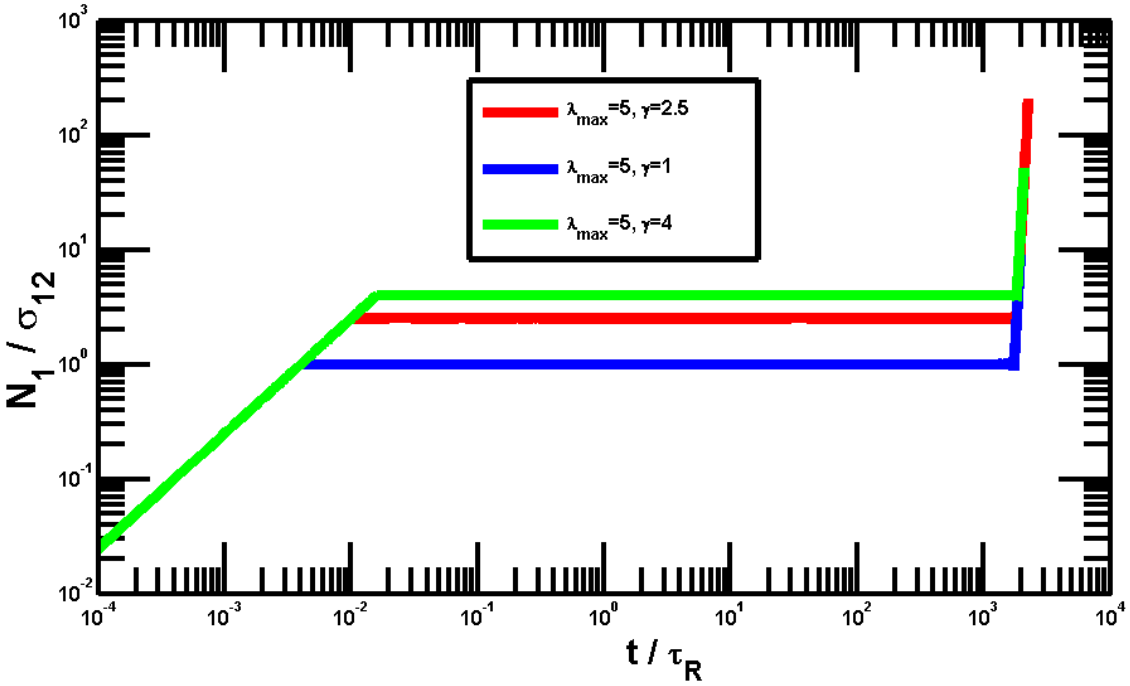

(b) Lodge-Meissner relation

Figure C.3: Modified Rolie-Poly prediction of the Lodge-Meissner relation for different rates.

sient observed in the post-overshoot relaxation at high shear rates in some entangled wormlike micelles. The model predicted the Lodge-Meissner relationship but failed at high strains and long times quintessential of highly entangled systems. The modified Rolie-Poly predicted that the magnitude of the finite extensibility of the micelle chains did not influence the relaxation mechanism. Rather, it showed that the mechanism was strain dependent. Strain hardening was observed for large deformations followed by significant strain softening due to quick relaxation of stress by retraction of the chain segments. This was in agreement with experiments in literature [19].

The modified Rolie-Poly model has shown promise in predicting nonlinear phenomena in entangled systems. We look forward to further modification of the model to enhance its predictions in areas where it is lacking. The first stop being to use the alternative nonlinear spring constant [Eq. (C.5)], and observing the predictions. Depending on the outcome of results from the alternative spring constant, we would consider coupling diffusion and solvent stress into the model. Alongside the computational work, effort would be made to advance experiments. Preliminary results have been obtained for step strain experiments (not included in interest of space). We plan on finalizing the experiments in a couple of weeks then move on to optical measurements and determination of causes of shear banding to augment our understanding of this weird but interesting phenomenon and verify our theoretical predictions.

C.6 Outlook

The effect of the CCR in the Rolie-Poly and GLAMM models is to relax the chain stretch [2]. We hypothesize that having chains with the ability to stretch to infinity limits the ability of the CCR (even at maximum rate) to relax the chain stretch. Hence, the need of very large values of Z to observe shear banding phenomena at $\beta < 1$ as in Adams' [3] model. We aim at modifying the diffusive Rolie-Poly (DPR) model of Adams in the future to include finite extensibility with a view of

obtaining quantitative agreement of the DPR with experiments. If they agree, we would attempt to obtain the value of CCR parameter, β at which transient and steady state banding occur. This could lead to an independent way of obtaining β. With a clearer understanding of the effect of the constitutive relations of these parameters, by setting $\beta = 1$, we can attempt to obtain a strictly monotonic constitutive equation that would predict shear banding phenomenon. The possibility of predicting shear banding with a strictly monotonic constitutive equation has been debated between opponents and adherents of the tube model [21, 22, 23, 7]. One can observe the dependence of β in the modified Rolie-Poly equation (Eq. (C.2)) is analogous to the CCR rate c_v in the GLAMM model [1] and β in Marrucci's model [4]. In summary, the Rolie-Poly model has shown promise in predicting many nonlinear phenomena observed in experiments.

Bibliography

[1] R. S. R. Graham, A. A. E. Likhtman, T. C. B. McLeish, and S. T. Milner, Journal of Rheology **47**, 1171 (2003).

[2] A. E. Likhtman and R. S. Graham, Journal of Non-Newtonian Fluid Mechanics **114**, 1 (2003).

[3] J. M. Adams, S. M. Fielding, and P. D. Olmsted, Journal of Rheology **55**, 1007 (2011).

[4] G. Marrucci, Journal of Non-Newtonian Fluid Mechanics **62**, 279 (1996).

[5] J. M. Dealy and R. G. Larson, *Structure and rheology of molten polymers: from structure to flow behavior and back again* (Hanser Publishers, Cincinnati, 2006) p. 516 p.

[6] K. Osaki, T. Inoue, and T. Isomura, , 1917 (2000).

[7] M. Cromer, M. C. Villet, G. H. Fredrickson, and L. G. Leal, Physics of Fluids **25**, 051703 (2013).

[8] R. Keunings, Journal of non-newtonian fluid mechanics **68**, 85 (1997).

[9] M. Doi and S. F. Edwards, Journal of the Chemical Society, Faraday Transactions 2 **74**, 1818 (1978).

[10] M. Doi and S. F. Edwards, *The theory of polymer dynamics* (Oxford University Press, Oxford, 1986) p. 391.

[11] P. D. Olmsted, Rheologica Acta **47**, 283 (2008).

[12] J. M. Adams, S. M. Fielding, and P. D. Olmsted, Journal of Rheology **55**, 1007 (2011).

[13] J. F. Berret, in *Molecular Gels: Materials with Self-Assembled Fibrillar Networks*, edited by R. Weiss and P. Terech (Springer Netherlands, 2006) pp. 667–720.

[14] M. E. Cates and S. M. Fielding, Advances in Physics **55**, 799 (2006), arXiv:0702047 [cond-mat] .

[15] S. S. Ravindranath, *How do entangled polymer liquids flow?*, Ph.d, University of Akron (2010).

[16] R. G. Larson, T. Sridhar, L. G. Leal, G. H. McKinley, a. E. Likhtman, and T. C. B. McLeish, Journal of Rheology **47**, 809 (2003).

[17] C. R. López-Barrón, a. K. Gurnon, A. P. R. Eberle, L. Porcar, and N. J. Wagner, Physical Review E - Statistical, Nonlinear, and Soft Matter Physics **89**, 042301 (2014).

[18] E. Miller and J. P. Rothstein, Journal of Non-Newtonian Fluid Mechanics **143**, 22 (2007).

[19] E. Brown, W. Burghardt, and D. Venerus, Langmuir **7463**, 3902 (1997).

[20] R. G. Larson, S. A. Khan, V. R. Raju, and M. Hill, Stress The International Journal on the Biology of Stress **32**, 145 (1988).

[21] J. M. Adams and P. D. Olmsted, Physical Review Letters **102**, 067801 (2009).

[22] J. M. Adams and P. D. Olmsted, Physical Review Letters **103**, 219802 (2009).

[23] S.-Q. Wang, Physical Review Letters **103**, 219801 (2009).

APPENDIX D

Supplementary Rheological Data for CTAB/NaSal Surfactant Solutions

D.1 Strain Sweep

A sample strain sweep data is shown in Fig. D.1. The storage (G') and loss (G") moduli become strain dependent at strains above 100 %. They strain soften till about 300 % strain before strain hardening as evident from the increase in G' and G". The G' curve drastically reduced after strains above 400 %. The trend of the G' curve is reminiscent of the linear to strain softening then strain hardening followed by a collapse to strain softening of the stress relaxation curves as strain increased (Fig. 4.6a).

D.1.1 Stress Relaxation for 0.1 M CTAB 0.11 M NaSal wormlike micelles

The stress relaxation curves for CTAB/NaSal $C_S/C_D = 1.1$ wormlike micelles are presented in Fig. D.2.

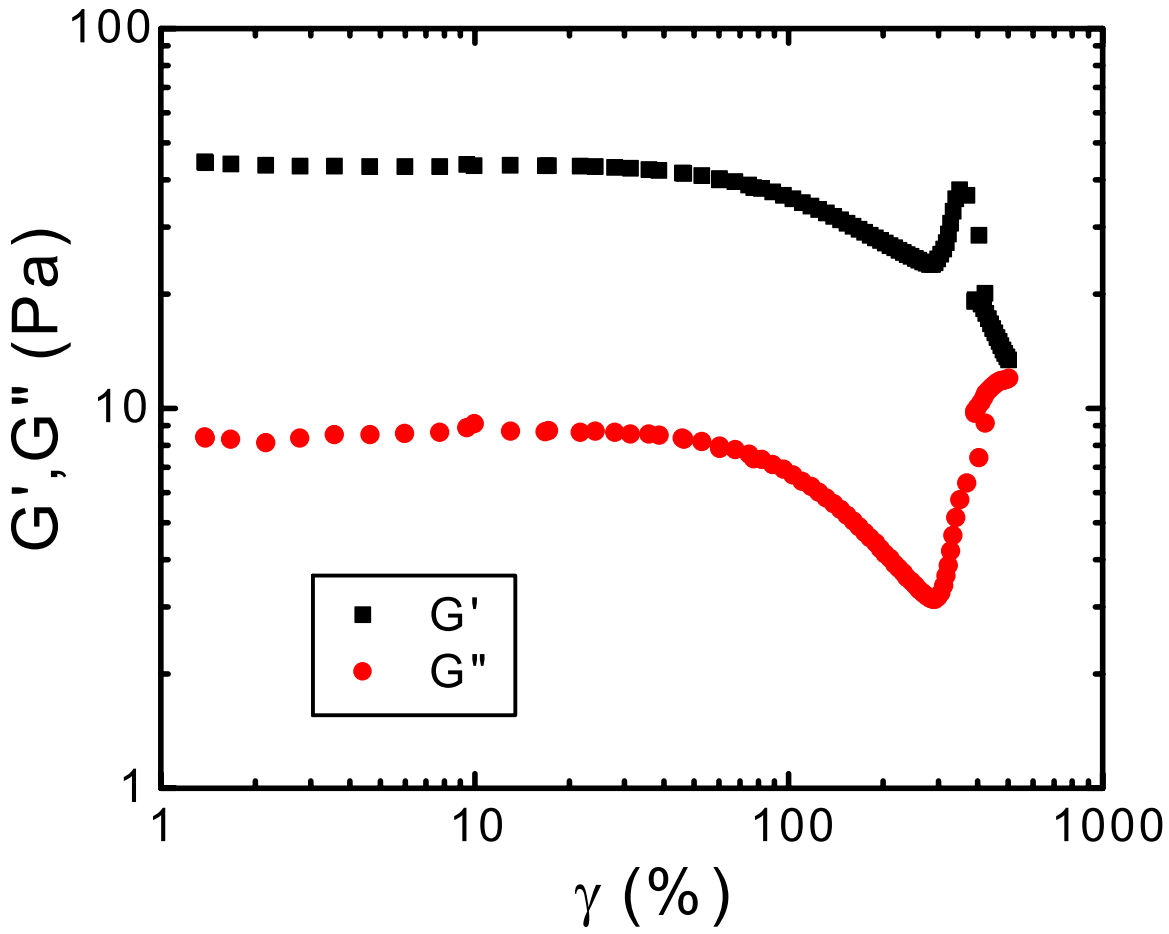

Figure D.1: Strain dependence of storage and loss moduli at a frequency of 6.28 rad/s for 0.1 mol/L CTAB and 0.12 M NaSal at 25 °C.

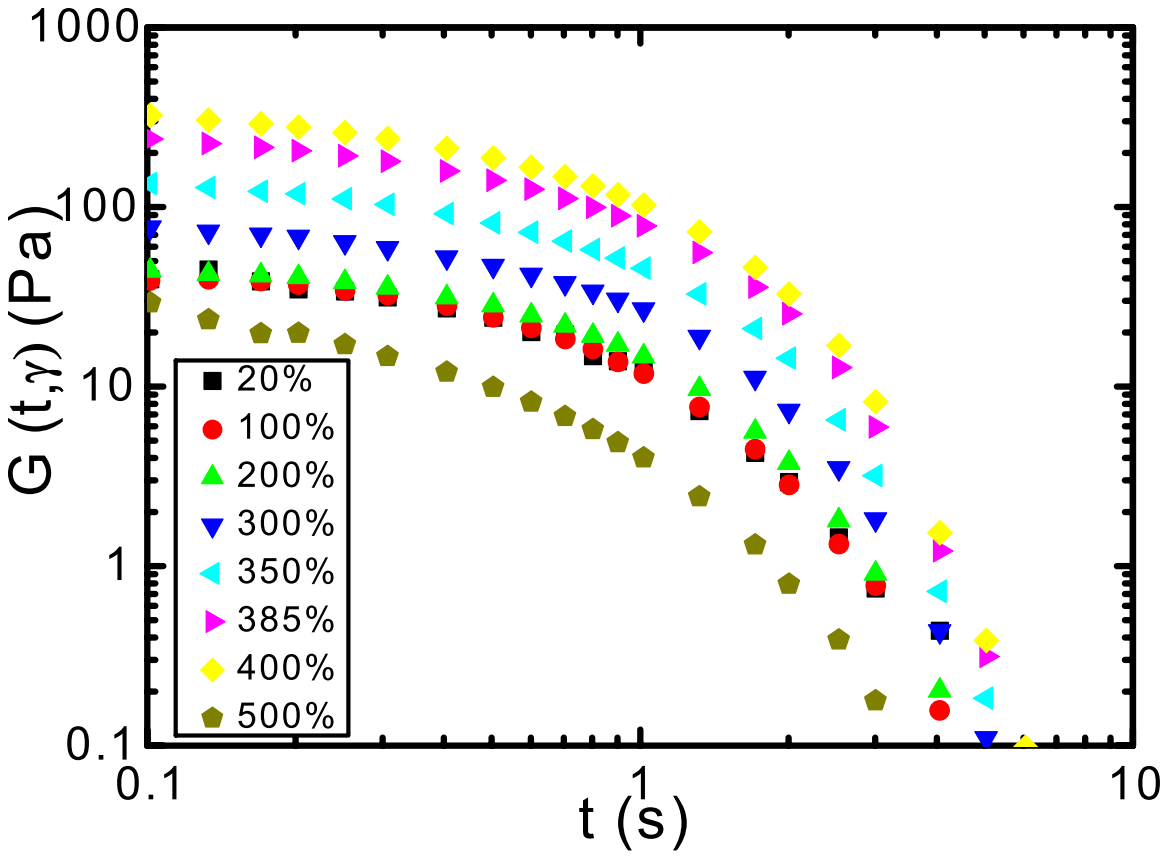

Figure D.2: Stress relaxation curves with varying strains for 0.1 M CTAB and 0.11 M NaSal at 25 °C.

D.2 Equilibration time for 0.1 M 0.16 M NaSal wormlike micelles at 25 °C.

We performed repeated step strain measurements on the wormlike micelles with delay times of 120 s after each run to determine if any hysteresis occurred after the equilibration time used for the experiments at 25 °C. The result is presented in Fig. D.3 and we observe that the equilibration time of 120 s was sufficient for the wormlike micelles to reorient themselves to their equilibrium structure without the strain history affecting the subsequent stress relaxation experiments. The delay time required to achieve the equilibrium structure increases with decreasing temperature. The delay time required for the wormlike micelles was checked for the wormlike micelles at a certain temperature by performing similar experiments. The minimum delay time used for any experiment was 120 s and as a convenient rule of thumb at least 1.2 times the required value obtained from such experiment was used in cases where it was above 120 s. [1]

Bibliography

[1] A. A. Adams, M. J. Solomon, R. G. Larson, and X. Xia, Journal of Rheology **61**, 967 (2017).

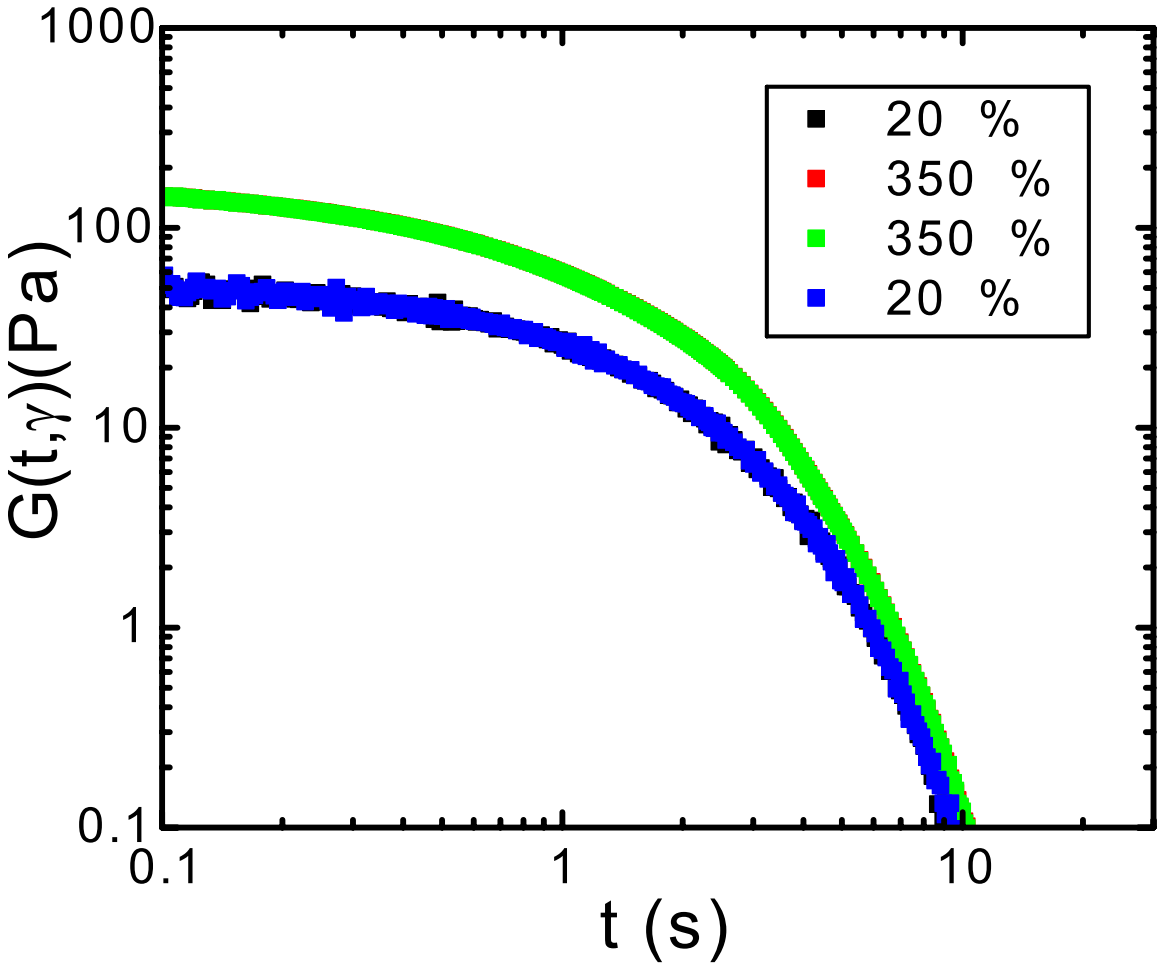

Figure D.3: Stress relaxation curves with varying strains for a sample of 0.1 M CTAB and 0.16 M NaSal at 25 °C. The experiments were performed consecutively at strains of 20, 350, 350 and 20 % with wait times of 120 s between each experiment.